A HYBRID PARTICLE/CONTINUUM APPROACH FOR NONEQUILIBRIUM HYPERSONIC FLOWS

by

Wen-Lan Wang

A dissertation submitted in partial fulfillment
of the requirements for the degree of
Doctor of Philosophy
(Aerospace Engineering)
in The University of Michigan
2004

Doctoral Committee:

Professor Iain D. Boyd, Chairperson
Assistant Professor Andrew J. Christlieb
Professor Philip L. Roe
Professor Bram van Leer

Dedicated to my family for years of encouragement and support,
and to my friends.

ACKNOWLEDGEMENTS

First and foremost, I would like to express my sincere thanks to my advisor, Professor Iain D. Boyd, for his guidance throughout this research, for his insight into many questions, and for his gracious support and constant encouragement. The lessons I have learned from him will stay with me for the rest of my professional career.

I appreciate Professor Andrew Christlieb for his many suggestions to this research. I also wish to thank the other members of my doctoral committee, Professor Philip Roe and Professor Bram van Leer, for their comments and participation.

I gratefully acknowledge Professor Graham Candler of University of Minnesota for providing the CFD code and Ioannis Nompelis for providing some CFD solutions in this dissertation and answering many tedious questions. I would also like to express thanks for the assistance from the University of Minnesota Department of Aerospace and Mechanics Computational Facilities.

A special thanks goes to Dr. Quanhua Sun for his help and collaboration throughout this research. I am also grateful to every member in the research group, including Dr. Michael Kaidar, Justin Koo, Matt McNenly, Jerry Emhoff, and Michael Martin, for many research or non-research related discussions.

I would like to acknowledge the enjoyable time I had in the OpenFront group in the Engineering Research Center for Reconfigurable Machining Systems (ERC/RMS) at the University of Michigan. I thank the project director Dr. Zbigniew Pasek and

former leader Dr. Uri Benchetrit for their support. I am also grateful to the team members: exchange student Markus Einarsson from Sweden, Chris Tusciuk, Gabe Tewari, Chris Holtz, Forbes Husted, Stephen Marker, Dr. Byung-Kwon Min, and exchange student Michael Kremer from Germany. Working with them for three years is a very happy and memorable experience of my life.

To my friends, I appreciate their company in many extracurricular and social activities. I would especially like to thank Kevin Ma, Ying-Chao Hung and his wife Ming-Hui Hsieh, Wan-Thai Hsu and his wife Queenie, Vincent Yu, Wei-Cheng Tian and his wife Jennifer, Ei-Wen Lo and his wife Kelly, Ray Fu and his wife Melissa, Chung-Yen Chao and his wife Fang-Yi Chiang, Tun-Cheng Chien and his wife Chen-Chen Tu, and many others. I cherish their friendship and have tons of pleasure memories to share with them.

I am greatly indebted to my parents for their unending support and encouragement throughout my lengthy doctoral program. Their love and patience have been the only hope during my downtime.

Finally, I would like to acknowledge the financial support I have received from the Air Force Office of Scientific Research under grant F49620-01-1-0003. Without financial support, this study would have not been possible.

TABLE OF CONTENTS

LIST OF FIGURES

Figure

LIST OF TABLES

Table

LIST OF APPENDICES

Appendix

CHAPTER I

INTRODUCTION

1.1 Motivation

The interactions of the bow shock of a hypersonic vehicle and the shock waves from a wing or control surface are of great interest in the design of reusable launch vehicles (RLV), space planes, and hypersonic cruise vehicles, because of the potentially high localized temperature and the associated extremely high aerothermal loads in the interaction region. The interactions are also often seen on the compression ramp forming the integrated airframe inlet to an air-breathing engine. The shock waves impinging on the vehicle control surface may cause boundary layer separation and, as a result, may reduce the control surface effectiveness.

For many years, experimental and numerical efforts have been undertaken on understanding the shock/shock and shock/boundary layer interactions in hypersonic flows. Because of the tremendous technical complexities, such as the uniformity of a hypersonic flow in a wind tunnel and measuring techniques, and costs, flight and experimental measurements under realistic conditions are limited and sometimes difficult to understand. On the other hand, because of the increasing availability of computing resources, numerical means play a pivotal role in the design of the next generation hypersonic vehicles.

Future hypersonic vehicles will likely have leading edges made from a material similar to the Ultra-High Temperature Ceramics (UHTC's) being developed at the NASA Ames Research Center. There materials are reusable for temperatures up to 3,100 K and do not ablate [69]. The use of UHTC's makes it possible to design a new generation of vehicles with very sharp leading edges and smooth surfaces, resulting in a much smaller, lighter, and more efficient vehicle. For instance, the leading edge made from UHTC's could have a radius as small as 0.23 cm, compared to 81.5 cm for the nose made from the reinforced carbon-carbon material used on the Space Shuttle. Therefore, passively cooled leading edges of the order of 1 mm in radius are feasible.

The fact that future hypersonic vehicles will have very small leading edge radii does not solve the problems of localized high heat transfer from shock interactions. Instead, it puts these interactions into the regime where a continuum simulation approach is not necessarily valid. In Figure 1.1, the velocity and Knudsen number of a typical entry trajectory of an RLV are plotted as a function of the flight altitude [11]. The Knudsen number is evaluated based on a leading edge radius of 0.23 cm as the characteristic length. The Knudsen number is about 0.0074 at an altitude of 40 km and it is about 0.03 at an altitude of 50 km. It is clear that the flow near the leading edge is likely to be non-continuum at 40 km and will certainly be rarefied at 50 km. Therefore, the flow around a hypersonic vehicle during its atmospheric re-entry always spans a very wide range of flow regimes, depending upon the flight altitude and the characteristic length scale.

The large variation in flow properties leads to some regions where the flow is accurately described as a continuum and can be modeled by the Navier-Stokes (NS) equations and solved numerically by Computational Fluid Dynamics (CFD) meth-

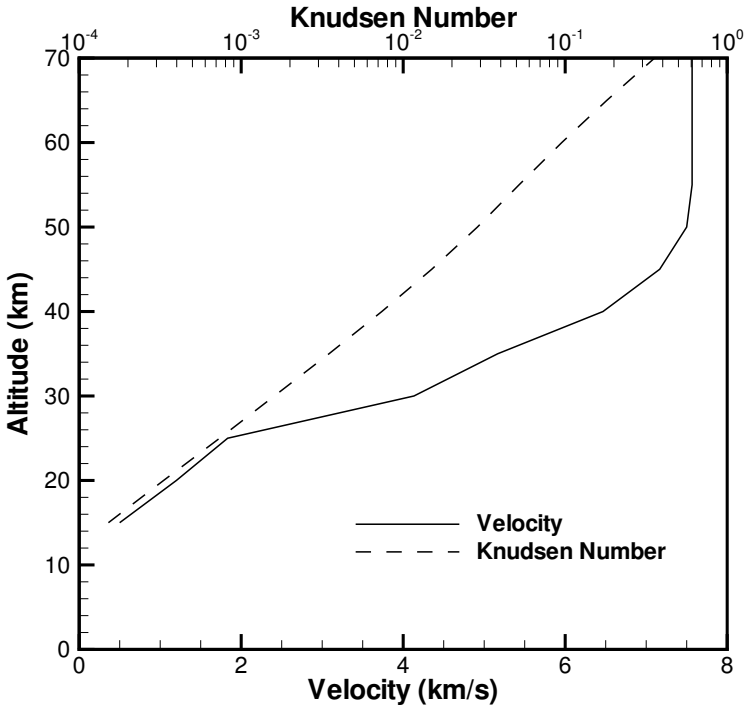

Figure 1.1: Velocity and Knudsen number of the entry trajectory of a RLV with 0.23 cm as the characteristic length.

ods. However, the wide variation in flow properties also leads to some regions where the flow is rarefied and the NS equations break down because of physical limitations. A particle simulation technique such as direct simulation Monte Carlo [16] (DSMC) is commonly employed for such conditions.

DSMC emulates the nonlinear Boltzmann equation with simulated particles by moving them around based on their microscopic velocities and simulating the intermolecular collisions with frequencies and scattering velocity distributions determined from the kinetic theory of a dilute gas. Theoretically, the DSMC method can also be applied to continuum flows, but it demands huge amounts of computational capacity because of the requirement of a sufficiently large number of simulated particles in regions where the flow is dense.

Therefore, on one end of the numerical spectrum is CFD, which solves a set

of partial differential equations, is numerically efficient for continuum flows, but is considered physically inappropriate for rarefied or strongly nonequilibrium flows. On the other end of the numerical spectrum is DSMC, which emulates the Boltzmann equation with simulated particles, is physically accurate for both continuum and rarefied flows, but is too computationally intensive for dense flows.

For flow configurations involving a mixture of continuum and rarefied regimes, such as the hypersonic flows of interest in this thesis, it is an attractive idea to unify the two methods in a way such that the rarefied and continuum domains are handled by DSMC and CFD, respectively. This is not an easy task, however, because the two numerical methods are different to a large extent in terms of physical representation and programming algorithm. To make them work together, many issues must be dealt with carefully.

A major issue regarding the development of a hybrid DSMC/CFD method is to determine, in a flow, which regions are rarefied and which are continuum. In other words, a criterion is required for the placement of the interfaces between the rarefied and continuum domains.

Another issue in developing the hybrid method arises from the information exchange at the interfaces. At each interface, macroscopic flow properties must be provided to the CFD method to evaluate the net fluxes and to the DSMC method to initialize the particles entering from the continuum domain into the particle domain. For strongly nonequilibrium, hypersonic flows, the information exchange must take place for each time step.

1.2 An Overview of Previous Hybrid Approaches

The idea of a hybrid particle/continuum approach is not new and several attempts have been considered previously. The simplest hybrid approach involves splitting the whole domain into two and performing two decoupled simulations. The study by Hash and Hassan [45] was for a hypersonic flow over a 70° blunted cone with a sting and the scheme proposed by George and Boyd [37] was for supersonic expanding flows. The CFD solution in a decoupled hybrid approach is used to provide boundary conditions for DSMC. A decoupled hybrid approach is good only for flows in which the interface between the continuum and particle domains is determined once and for all.

Using interpolation of fluxes or physical variables for each time step, Wadsworth and Erwin first performed a one-dimensional shock problem [84] and a two-dimensional slit flow [85]. Employing the Marshak condition as the coupling mechanism for resolving fluxes at the interface, Hash and Hassan assessed a hybrid approach in Couette flows [44] and revisited the hypersonic flow over a 70° blunted cone problem [46]. The Marshak condition employs a conservation of fluxes at the domain interfaces and the net flux is the summation of the half-flux crossing from the DSMC side plus the half-flux crossing from the Navier-Stokes side. The strategy of coupling a particle method and the Navier-Stokes equations by friction or half fluxes was respectively proposed by Bourgat *et al.* [18] and Le Tallec and Mallinger [81] to simulate hypersonic flows over an object. To overcome the statistical scatter in the particle method, a second order smoothing technique was used [46], but it sometimes produced nonphysical results. All other approaches in this paragraph employed the technique that one global update of the macroscopic properties requires several DSMC sampling steps.

Therefore, these hybrid approaches are inappropriate for strongly nonequilibrium flows in which the detailed nonequilibrium information in the particle domain must be shared with the coupled continuum method for each time step.

A more sophisticated hybrid technique using the kinetic flux-vector splitting (KFVS) scheme [28] was developed by Lou [56] and Duttweiler [31] at Stanford. Interestingly, when their technique was applied to a Mach 10 flow over a 2-D rectangle, the Navier-Stokes equations were solved near the surface where the gradients are large and the NS equations are expected to be invalid. Recently, a hybrid scheme for flows with thermal and chemical nonequilibrium was established by Michaelis [59] but most of the work was focused on one dimensional configurations.

The scheme proposed by Rovedo *et al.* [70, 71] incorporated the DSMC method with the adaptive discrete velocity (ADV) Euler solver, and would therefore not be appropriate for nonequilibrium flows. The scheme introduced by Garcia [36] embedded a particle method with the adaptive mesh and algorithm refinement (AMAR) method. This scheme has been shown to work well for simple flows, such as a 1-D Mach 2 impulsively started piston problem, a 1-D Mach 2 Rayleigh problem, and a Mach 1 flow over a sphere, but has not been fully tested for hypersonic flows. The approach studied by Hadjiconstantinou [41] coupled molecular dynamics with finite/element methods and would not be appropriate for rarefied gas flows because the molecular dynamics technique has proved to be valuable only for the simulations of dense gases and liquids [4].

Postprocessing with a filter to reduce the statistical scatter in the DSMC solution is an interesting direction for the development of a hybrid approach. Oh and Oran [63] showed that the Flux-Corrected-Transport (FCT) method has the ability to filter out the high-frequency fluctuations very naturally. Information was

extracted from DSMC to NS by the interpolation algorithm using a bilinear shape function. Later, another filter using the FCT method was proposed by Kaplan and Oran [52]. Their filter employed a high-order, nonlinear monotone convection algorithm to remove high-frequency statistical fluctuations. While the idea of filtering is promising, it is unknown at the present time how to use it for information exchange at the domain interface.

A hybrid approach in which the continuum and particle regions are combined by an overlapped Schwarz alternating method with Dirichlet-Dirichlet type boundary conditions was proposed by Aktas and Aluru [1] for multiscale analysis of microfluidic filters. This approach required multiple sampling steps in the particle domain for one global update of the macroscopic properties, and would be inappropriate for strongly nonequilibrium flows for the same reason mentioned previously.

More recently, Sun [77] developed a hybrid approach that employs the Information Preservation (IP) technique [33] coupled with a NS solver. While the approach was shown to be accurate and efficient, it was primarily applied to 2-D, low speed microscale gas flows. The IP technique in Sun's hybrid approach is inapplicable for supersonic compressed flows due to the inappropriate numerical scheme implemented for solving the continuity equation. In addition, the IP technique is inaccurate for strongly nonequilibrium flows because of the assumption made for the energy fluxes crossing computational cells.

Therefore, to date, a robust, multi-dimensional hybrid approach that is capable of handling nonequilibrium, hypersonic compressed flows has not yet been accomplished. The ideal hybrid code must be efficient, parallelized, and implemented in a single program.

1.3 Current Status of Computations of Laminar Hypersonic Interacting Flows

To improve the understanding of shock/shock and shock/boundary layer interactions in hypersonic flows, a number of experiments have been performed in the Large Energy National Shock (LENS) facility at the Calspan - University at Buffalo Research Center (CUBRC) to provide a benchmark database at well calibrated hypersonic test conditions. The experiments were conducted to examine complex interaction regions developed over simple model configurations in fully laminar flows. The experimental results were not made available to the public until after a blind code validation exercise organized by Dr. Michael Holden at the 2001 AIAA Aerospace Sciences Meeting in Reno [51, 43].

During the exercise, two model configurations - a double cone and a hollow cylinder/flare - emerged as simple configurations over which complex interacting flows are developed which can provide a stringent test of the numerical schemes that are employed in the Navier-Stokes and DSMC computations. A schematic of the two configurations is shown in Figure 1.2. The configurations are assumed to be perfectly aligned with the pure nitrogen freestreams so the flows are axisymmetric. Solutions were invited by a limited number of experts in the field of hypersonic computations: Graham Candler [25] (CFD, University of Minnesota), Peter Gnoffo [38] (CFD, NASA Langley Research Center), James Moss [60] (DSMC, NASA Langley Research Center), John Tannehill [53] (CFD, Iowa State University), Iain Boyd [23] (DSMC, University of Michigan), and Chris Roy and Michael Gallis [72] (CFD and DSMC, Sandia National Laboratories).

Despite its simple shape, the double cone creates complicated flow structures. In general, the first cone produces an attached oblique shock wave and the second,

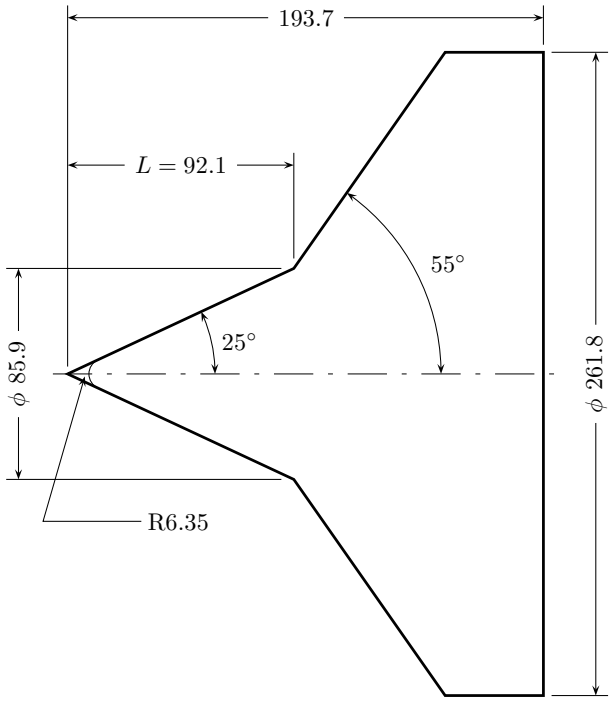

(a) 25°-55° sharp and blunted double-cone.

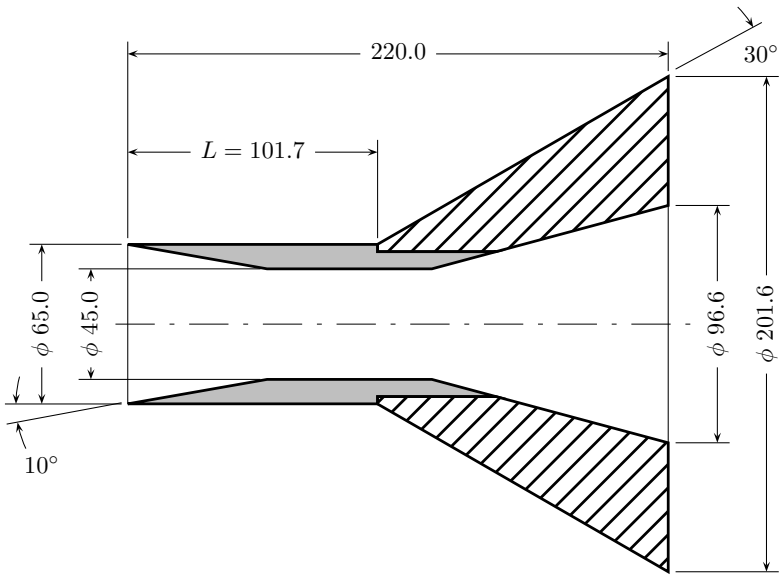

(b) Hollow cylinder/flare.

Figure 1.2: Schematic of the CUBRC wind-tunnel models (measurements in mm).

larger angle cone produces a detached bow shock. These two shock waves interact to form a transmitted shock that strikes the second cone surface near the cone-cone conjunction. The adverse pressure gradient due to the cone juncture configuration and the transmitted shock generates a large region of separated flow that in turn produces its own separation shock. This shock interacts with the attached oblique shock from the first cone, altering the interaction with the detached shock from the second cone. The size of the separation zone is then affected by this interaction.

A weak oblique shock starts from the sharp leading edge of the hollow cylinder and coalesces with the shock generated by the separation somewhere along the cylinder. Two shocks together interact with the detached bow shock due to the flare to form a strengthened shock wave. This interaction, taking place near the surface of the body, elevates the pressure and increases the adverse pressure gradient due to the flare juncture, which causes the boundary layer on the cylinder to separate. This in turn, produces the separation shock.

The code validation exercise resulted in several key conclusions. One of them was that DSMC always under-predicted the size of the separation zone in the double cone for the hypersonic flows considered. For example, the surface heat transfer coefficients for Run 35 obtained by different methods are compared in Figure 1.3. The under-prediction is not believed to be a flaw of the DSMC method. The likely explanation for the poor DSMC results is that the freestreams were too dense and none of the participants who performed DSMC simulations had employed a sufficiently large amount of simulated particles and required fine grids. Later investigations verified that DSMC can well predict the size of the separation zone if the density in the freestream is reduced by a factor of 3 [73, 42]. Therefore, for the DSMC solution of Run 35 to be properly resolved it is necessary to ensure that the computational cells

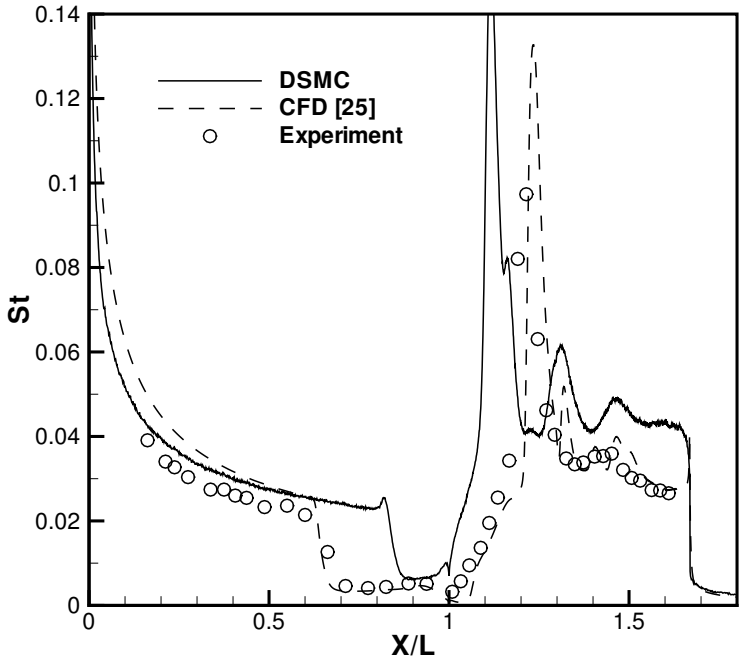

Figure 1.3: Comparison of surface heat transfer coefficients for Run 35 on the 25°-55° sharp double-cone.

are sufficiently small and remain populated with a reasonable number of particles. For practical purposes, only the region of about the first 5 cm of the first cone is considered in this thesis. Such a simple geometry provides a basic assessment for the development of the hybrid approach.

Another conclusion in the code validation exercise was that some NS solutions, for example by Candler [25] and Gnoffo [38], over-predicted to a large extent the size of the separation zone in the hollow cylinder/flare configuration in a certain of freestream conditions (Run 11) while the DSMC solutions were in good agreement with the measured data. A comparison of surface heat transfer coefficients for different methods is made in Figure 1.4. This shows that the solutions predicted by CFD under rarefied conditions may be inaccurate. The main reason of the over-prediction of the size of the separation zone is very likely due to the numerical schemes and grids employed in the CFD simulations because one CFD simulation performed by

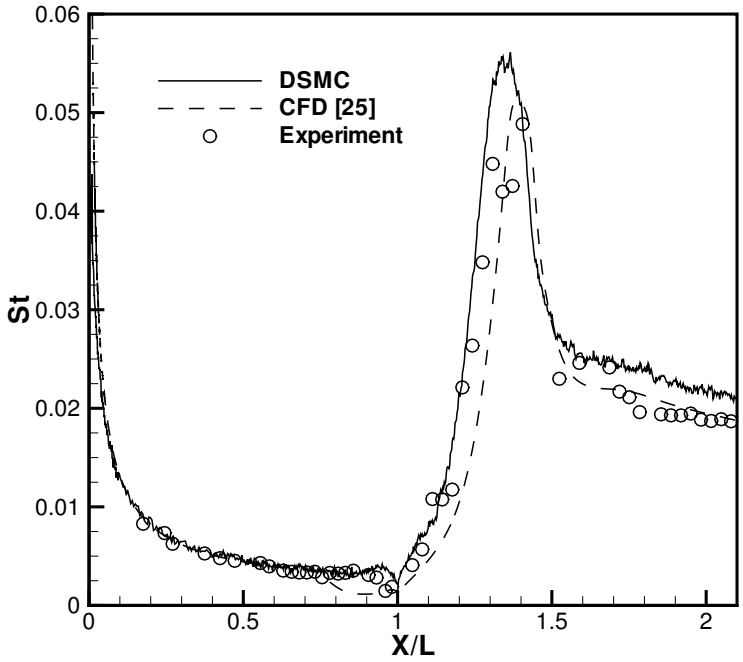

Figure 1.4: Comparison of surface heat transfer coefficients for Run 11 on the hollow cylinder/flare.

Kato and Tannehill [53] did predict the size correctly. This raises a challenge to the DSMC/CFD hybrid approach. If the whole computational domain is initialized with a CFD solution with considerable discrepancies from the "correct" solution, can the hybrid approach eventually predict the correct solution? If the answer is yes, then how much effort will it take?

1.4 Objectives and Thesis Overview

There are three primary objectives in the thesis.

1. Predict the conditions under which the continuum approach may be expected to fail in hypersonic viscous flows. Determine a criterion for placing the interface between the rarefied and continuum domains.

2. Develop a hybrid DSMC/CFD approach for simulating nonequilibrium, hypersonic flows. The hybrid approach must be able to perform information

exchange between the particle and continuum domains for each time step. The hybrid approach also must be able to adjust the domain interface based on its solution. The hybrid approach must be physically accurate and numerically efficient.

3. Assess the hybrid approach. The accuracy of the hybrid results will be investigated by comparisons with the results obtained by other numerical methods and experimental data if available. The efficiency of the hybrid approach will be assessed by comparing the times consumed by the hybrid approach and the DSMC method.

In Chapter II, the mathematical and numerical formulations of the continuum and particle approaches will be briefly described. The Navier-Stokes equations in the continuum method are solved by a finite-volume method whereas the direct simulation Monte Carlo method is employed for the particle method. The Information Preservation method will also be discussed.

In Chapter III, verifications of the accuracy and consistency of the continuum and particle methods employed in the hybrid approach are conducted. In this chapter, a number of accuracy issues are carefully investigated for numerical simulations over a blunted cone tip and a hollow cylinder/flare.

In Chapter IV, a continuum breakdown criterion is developed. Investigations are performed through detailed comparisons of the numerical results obtained with continuum and particle methods. This chapter addresses the first objective.

In Chapter V, the details of the hybrid approach combining the CFD and DSMC methods is described. The emphases include how to handle particles moving in to or out from the DSMC domain, how to evaluate fluxes for CFD on the domain

interface, and how to parallelize the hybrid approach. This chapter addresses the second objective.

In Chapter VI, hypersonic flows over a blunted cone and a hollow cylinder/flare are considered to assess the accuracy and efficiency of the hybrid approach. Flow fields are carefully compared with the results obtained with the pure DSMC simulations to estimate the accuracy. Computational times consumed by the hybrid approach are compared to the times required by the pure DSMC simulations to estimate the efficiency. These studies therefore address the third objective.

In Chapter VII, a summary is presented and conclusions are drawn. This chapter ends with some recommendations for future work.

CHAPTER II

NUMERICAL METHODS

The mathematical and numerical formulations of the continuum and particle approaches will be briefly described in this chapter. A finite-volume method is employed to solve the Navier-Stokes equations for the continuum method whereas the direct simulation Monte Carlo method is employed for the particle approach. A recently developed technique, Information Preservation, is also utilized to reduce the statistical scatter in the direct simulation Monte Carlo method. The perfect gas assumption is made for all methods.

2.1 Velocity Distribution Function and the Boltzmann Equation

The ideal way of understanding a flow behavior is to deterministically track every microscopic detail, such as position and velocity, of each molecule in the flow. However, this is a task almost next to impossible even using the most powerful supercomputer nowadays because the number of molecules is enormously large in general and as a result the amount of information needed to be stored and processed is vast. One cubic centimeter of air at standard tempeature and pressure, for instance, contains approximately 2.687×10^{19} molecules. In addition, a description of this kind is not practical because it is macroscopic flow properties, such as density, bulk velocity,

temperature, stresses, and heat flow, that are of most interest. An alternative is to use a statistical means in terms of a particle velocity distribution function, F.

The time evolution in phase space of the particle velocity distribution function $F(\mathbf{x}, \mathbf{c}, t)$ of a dilute gas is governed by the nonlinear Boltzmann equation and can be expressed in terms of time $t \in \mathbb{R}^+$, the spatial coordinates $\mathbf{x} \in \Omega \subset \mathbb{R}^3$, and the molecular velocity $\mathbf{c} \in \mathbb{R}^3$. If external forces are absent, the Boltzmann equation reads

$$\frac{\partial}{\partial t}F + \mathbf{c} \cdot \nabla F = \frac{\delta}{\delta t}F, \tag{2.1}$$

subject to the initial condition

$$F(\mathbf{x}, \mathbf{c}, t = 0) = F_0(\mathbf{x}, \mathbf{c}),$$

complemented with the boundary conditions [27] for $\mathbf{c} \cdot \mathbf{e} \geq 0$ and $\mathbf{x} \in \partial\Omega$

$$F(\mathbf{x}, \mathbf{c}, t)|\mathbf{c} \cdot \mathbf{e}| = \int_{\mathbf{c}^* \cdot \mathbf{e} < 0} B(\mathbf{c}^* \to \mathbf{c}; \mathbf{x}, t) F(\mathbf{x}, \mathbf{c}^*, t)|\mathbf{c}^* \cdot \mathbf{e}| \, d\mathbf{c}^*,$$

where $\mathbf{e}$ is the inward unit normal and the non-negative function $B(\mathbf{c}^* \to \mathbf{c})$ denotes the scattering probability from the direction $\mathbf{c}^*$ to the direction $\mathbf{c}$. If permanent adsorption is excluded, the total probability for scattering particles must be unity

$$\int_{\mathbf{c} \cdot \mathbf{e} \geq 0} B(\mathbf{c}^* \to \mathbf{c}; \mathbf{x}, t) \, d\mathbf{c} = 1.$$

The right-hand side of Equation(2.1), $\delta F/\delta t$, is the collision operator and represents the time rate of change of the distribution function due to binary intermolecular collisions.

Assuming that the distribution function is normalized to the particle number density, n, if $Q(\mathbf{c})$ is a function of $\mathbf{c}$ but not of position and time, the moment of the distribution function F with respect to Q over the velocity space is defined as

$$n\overline{Q} \equiv \int_{\mathbb{R}^3} QF \, d\mathbf{c}. \tag{2.2}$$

Consider a perfect gas with molecular mass m and number of internal degrees of freedom ζ. Macroscopic states of the gas such as density and bulk velocity are moments of F

$$\rho = \int_{\mathbb{R}^3} mF \, d\mathbf{c}, \tag{2.3}$$

$$\mathbf{V} = \frac{1}{\rho} \int_{\mathbb{R}^3} m\mathbf{c}F \, d\mathbf{c}. \tag{2.4}$$

It is convenient to define a *thermal* or *peculiar* velocity, $\mathbf{c}'$, measured with respect to the macroscopic velocity of the gas

$$\mathbf{c}' \equiv \mathbf{c} - \mathbf{V}$$

and satisfying $\overline{\mathbf{c}'} = 0$ with the help of Equations (2.2) and (2.4). Similar to Equations (2.3) and (2.4), the translational energy per unit volume can be written

$$\begin{aligned} \tfrac{1}{2}\rho\overline{c^2} &= \int_{\mathbb{R}^3} \tfrac{1}{2}mc^2F \, d\mathbf{c} \\ &= \tfrac{1}{2}\rho(V^2 + \overline{c'^2}) \\ &= \tfrac{1}{2}\rho(V^2 + 3\,RT) \end{aligned} \tag{2.5}$$

with the translational temperature defined as

$$T \equiv \frac{1}{3\rho R} \int_{\mathbb{R}^3} mc'^2F \, d\mathbf{c} \tag{2.6}$$

where R is the specific gas constant.

Although the Boltzmann equation (2.1) describes the time evolution of the velocity distribution function in a single equation, it still remains a great challenge to be solved because of its nonlinearity and complexity. Analytical solutions to the Boltzmann equation are limited to very simple flows [27]. Most researchers focus their efforts on numerical approaches.

One approach is the direct numerical solution of the Boltzmann equation, directly solving the only dependent variable, the velocity distribution function, by using a finite difference or finite element method. There are two major difficulties about this approach. First, the velocity space domain is of infinite extent. Finite bounds must therefore be predetermined such that only a negligible fraction of molecules lie outside them. This is not a large concern for low-speed flows. However, this becomes a severe issue in the case of hypersonic or high-temperature flows in which a small fraction of molecules with very high velocities relative to the bulk of the gas can have a significant effect on the macroscopic flow properties. The second difficulty of this approach is the number of data points needed to correctly represent the distribution function. It is estimated that a total number of 10^{14} points in phase space are required for solving an unsteady three-dimensional flow in a grid with 100 intervals in each direction [16]. This requirement prevents the direct numerical method from being used for most engineering applications.

Recent development of the direct numerical solution of the Boltzmann equation is mainly due to the work by Ohwada *et al.* [64, 65]. They employed a finite difference method to handle the convection terms on the left hand side of Equation (2.1) and the numerical kernel method developed by Sone [76] to deal with the right hand side collision operator. However, application of their approach has been limited to one dimensional flow problems.

Two other approaches are presented in the rest of this chapter and they are continuum and particle methods. These methods are efficient from the engineering point of view but have their own limitations.

2.2 Continuum Method

2.2.1 Conservation Equations

Similar to the moment of the distribution function defined in Equation (2.2), Maxwell's equation of change can be derived by multiplying the Boltzmann equation (2.1) by $Q(\mathbf{c})$ and integrating over velocity space

$$\frac{\partial}{\partial t}(n\overline{Q}) + \nabla \cdot (n\overline{\mathbf{c}Q}) = \Delta[Q] \tag{2.7}$$

where

$$\Delta[Q] \equiv \int_{\mathbb{R}^3} Q \frac{\delta}{\delta t} F \, d\mathbf{c}.$$

If, however, $Q(\mathbf{c})$ is taken to be the collisional invariants $m, m\mathbf{c}$, and $m(c^2 + \zeta RT)/2$ (the principle of energy equipartition applied), $\Delta[Q]$ vanishes because the change in Q for both molecules must be zero in each collision. This leads to the conservation equations of gases

$$\frac{\partial}{\partial t}\rho + \nabla \cdot (\rho\overline{\mathbf{c}}) = 0, \tag{2.8}$$

$$\frac{\partial}{\partial t}\rho\mathbf{V} + \nabla \cdot (\rho\overline{\mathbf{c}\mathbf{c}}) = 0, \tag{2.9}$$

$$\frac{\partial}{\partial t}\rho E + \nabla \cdot (\tfrac{1}{2}\rho\overline{\mathbf{c}(c^2 + \zeta RT)}) = 0, \tag{2.10}$$

where $E = \frac{1}{2}\overline{c^2 + \zeta RT} = V^2/2 + c_v T$ is the specific total energy. Here, $c_v \equiv (\zeta+3)R/2$ is the specific heat at constant volume. If the distribution function in the flow is only slightly perturbed from the Maxwellian equilibrium distribution locally, it can be approximated by the Chapman-Enskog expansion and truncated from the second order term. The conservation equations above then reduce to the Navier-Stokes equations [40, 83]. In two dimensions, the NS equations in a vector form read

$$\frac{\partial}{\partial t}\mathbf{U} + \frac{\partial}{\partial x}\mathbf{F} + \frac{\partial}{\partial y}\mathbf{G} = 0 \tag{2.11}$$

where

$$\mathbf{U} = \begin{bmatrix} \rho \\ \rho u \\ \rho v \\ \rho E \end{bmatrix},$$

and

$$\mathbf{F} = \begin{bmatrix} \rho u \\ \rho u^2 - \tau_{xx} \\ \rho uv - \tau_{xy} \\ (\rho E - \tau_{xx})u - \tau_{xy}v + q_x \end{bmatrix}, \qquad \mathbf{G} = \begin{bmatrix} \rho v \\ \rho uv - \tau_{yx} \\ \rho v^2 - \tau_{yy} \\ (\rho E - \tau_{yy})v - \tau_{yx}u + q_y \end{bmatrix}$$

where u and v are the components of velocity in the x and y directions. With the *scalar pressure* defined as $p \equiv \frac{1}{3}\rho\overline{c'^2}$, the viscous-stress and heat-flux terms are expressed as

$$\tau_{xx} = -p + 2\mu[\partial u/\partial x - \tfrac{1}{3}\nabla \cdot \mathbf{V}], \tag{2.12a}$$

$$\tau_{yy} = -p + 2\mu[\partial v/\partial y - \tfrac{1}{3}\nabla \cdot \mathbf{V}], \tag{2.12b}$$

$$\tau_{xy} = \tau_{yx} = \mu(\partial u/\partial y + \partial v/\partial x), \tag{2.12c}$$

$$q_x = -\kappa \partial T/\partial x, \tag{2.12d}$$

$$q_y = -\kappa \partial T/\partial y. \tag{2.12e}$$

The perfect gas equation of state, $p = \rho RT$, is assumed. The viscosity μ is modeled with the power law

$$\mu = \mu_r (T/T_r)^{\omega} \tag{2.13}$$

and the thermal conductivity κ is determined from the Prandtl number

$$\mathrm{Pr} = c_p \mu/\kappa$$

where μ_r and T_r are reference quantities, ω is a constant characterizing the molecular interaction and c_p is the specific heat at constant pressure. To be consistent with the viscosity simulated in the particle approach, the reference viscosity takes the form

$$\mu_r = \frac{15\sqrt{\pi m k T_r}}{2\sigma_r(5-2\omega)(7-2\omega)} \tag{2.14}$$

where k is the Boltzmann constant and σ_r is the reference cross section and will be addressed in Section 2.3.2.

2.2.2 Navier-Stokes Solver – CFD

During the past few decades, Computational Fluid Dynamics (CFD) has been well developed to numerically solve the Navier-Stokes (NS) equations. Although a general method working for all kinds of flows is not yet possible, some techniques have achieved great success for certain categories of flows [6, 47, 48]. Among those techniques, a finite-volume method is considered to be the best candidate of solving the NS equations for supersonic flows. The finite-volume form of the NS equations in two dimensions can be written as

$$\frac{d\mathbf{U}}{dt} = -\frac{1}{A}\sum_{\text{edges}}(\mathbf{F}\Delta y - \mathbf{G}\Delta x) \tag{2.15a}$$

where A is the area of the cell and Δx and Δy are the changes of x and y along an edge. For axisymmetric flows, the NS equations must include a source term and can be written as

$$\frac{d\mathbf{U}}{dt} = -\frac{1}{Ay_c}\sum_{\text{edges}}\bar{y}(\mathbf{F}\Delta y - \mathbf{G}\Delta x) + \mathbf{S} \tag{2.15b}$$

with $\mathbf{S}$ defined as

$$\mathbf{S} = \begin{bmatrix} 0 \\ 0 \\ p_c/y_c - 2\mu(v_c/y_c - \frac{1}{3}\nabla \cdot \mathbf{V}_c)/y_c \\ 0 \end{bmatrix}.$$

Here, $\bar{y}$ is the midpoint of the edge and the subscript c represents the centroid of the cell.

If the flux function on a cell edge is defined as $\mathbf{\Phi} \equiv (\mathbf{F}\Delta y - \mathbf{G}\Delta x)/\Delta s$, where $\Delta s = \sqrt{(\Delta x)^2 + (\Delta y)^2}$ is the edge length, equations (2.15) for a general two-dimensional flow are approximated as

$$\mathbf{U}^{t+\Delta t} - \mathbf{U}^t = -\frac{\Delta t}{A y_c} \sum_{\text{edges}} \bar{y}\mathbf{\Phi}\Delta s + \mathbf{S}. \tag{2.16}$$

In the thesis, the flux function is evaluated with an explicit, modified Steger-Warming flux vector splitting scheme [57], accurate to second order in space. To evaluate the fluxes on the interface between cells (i,j) and (i+1,j), a total number of eight cells surrounding it are involved, as shown in Figure 2.1. The strategy of the parallelization of the hybrid approach is largely influenced by the stencil for the flux evaluation and will be discussed in Section 5.4. An implicit Gauss-Seidel line-relaxation technique for the time integration that speeds up the numerical convergence is also employed in some calculations in the next chapter.

2.2.3 Slip Boundary Conditions

In a transitional flow, it is observed that the gas very close to a solid stationary wall is not considered to be at rest, therefore a velocity "jump" between the flow and the wall exists. A similar phenomenon is also observed for temperature. These

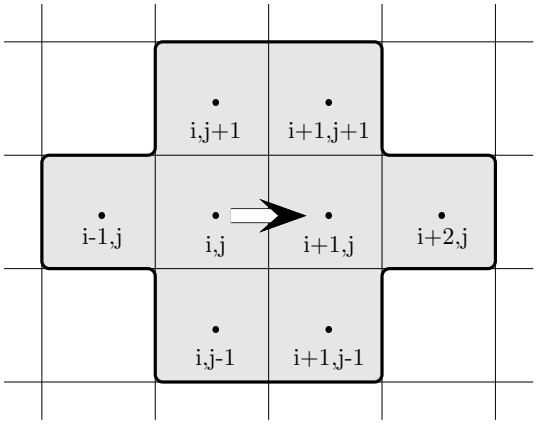

Figure 2.1: The stencil for the finite-volume scheme.

jumps are modeled with the Maxwell-Smoluchowski slip boundary conditions [74]

$$\vec{u}_s = \frac{2-\alpha_v}{\alpha_v}\lambda_v \frac{\partial \vec{u}}{\partial n}\Big|_w \tag{2.17}$$

$$T_s = T_{\text{wall}} + \frac{2-\alpha_T}{\alpha_T}\lambda_T \frac{\partial T}{\partial n}\Big|_w. \tag{2.18}$$

Here, T_{wall} is the temperature of the surface and α_v and α_T are the tangential momentum and thermal accommodation coefficients of the surface. The mean free path for momentum (λ_v) and thermal energy (λ_T) were given by Gökçen [39]

$$\lambda_v = \frac{2\mu}{\rho\bar{c}}, \qquad \lambda_T = \frac{2\kappa}{\rho\bar{c}c_v}$$

where $\bar{c} = \sqrt{8RT/\pi}$ is the mean molecular speed. The subscript w indicates conditions at the wall, or surface of the wind tunnel model. The slip velocity is tangent to the surface, and the normal-direction velocity component is set to zero at the surface.

Once the slip temperature is computed, heat flux to the surface is calculated as

$$q_w = -\kappa \frac{\partial T}{\partial n}\Big|_w = -\kappa \frac{T_1 - T_s}{\Delta n}$$

where T_1 is the temperature at the first cell center away from the wall, and Δn is the normal-direction distance from that cell center to the surface.

2.2.4 Limitations of the NS Equations

As stated in Section 2.2.1, the NS equations are derived based on the assumptions of slight deviation from local thermodynamic equilibrium and first-order approximation of the Chapman-Enskog expansion. If the local distribution function is not simply slightly deviated from local equilibrium, higher order terms of the Chapman-Enskog expansion must be retained. The evaluation of the next term in the expansion leads to the so-called *Burnett equations*. However, attempts at solving the Burnett equations have uncovered many physical and numerical difficulties, such as violation of the second law of thermodynamics and numerical instability at high Knudsen numbers [29].

To overcome the violation of the second law of thermodynamics, Balakrishnan and Agarwal [9] have derived the Bhatnagar-Gross-Krook (BGK) Burnett equations by employing the BGK model [12] for the collision integral and using the Navier-Stokes equations to express the material derivatives in the second order distribution function. The BGK-Burnett equations ensure that the Boltzmann H-function is monotonically decreasing at high Knudsen numbers [10] and therefore do not violate the second law of thermodynamics. However, for strongly nonequilibrium flows, more and more terms in the expansion must be involved, resulting in a great challenge to form a set of closed equations [40].

Rather than mathematically dealing with the Boltzmann equation for a gas flow, another branch of numerical methods is based directly on the simulation of the physics of the flow. A technique of this kind generates thousands or millions of simulated particles, each representative of a large number of real molecules, in a computer, moves them, and makes collisions take place between them.

2.3 Particle Method

The molecular dynamics (MD) method is considered to be the first particle method, proposed by Alder and Wainwright in the late of 1950's [2, 3] to study the interactions of hard spheres. In a MD simulation, the time evolution of a set of interacting molecules is followed by integrating the classical Newton's equations of motion. The intermolecular force can be modeled with two-body or many-body potentials or an empirical choice. For instance, Rahman [68] studied a number of properties of liquid argon, using the Lennard-Jones potential on a system containing 864 atoms. The major disadvantage of this method is that the size of the molecular system must be very small. Consider the air at standard temperature and pressure again. A simulation of such gas involving a million simulated particles covers a volume of only 0.037 cubic microns [34]. However, if the density is an order of magnitude higher, the number of simulated particles required is decreased to about 10,000. Due to its nature, the MD technique has proved to be valuable only for the simulations of dense gases and liquids [4] but is not appropriate for dilute gases.

The most commonly used particle method for simulating a rarefied gas flow is the direct simulation Monte Carlo (DSMC) method [16]. This method was first introduced by Bird in the 1960's and has been developed to the state where it is very reliable, accurate, and has gained wide acceptance in the scientific community. The DSMC method emulates the nonlinear Boltzmann equation by simulating the real molecule collisions with collision frequencies and scattering velocity distributions determined from the kinetic theory of a dilute gas. With a sufficiently large number of simulated particles, Bird [14] has shown that the Boltzmann equation can be derived through the DSMC procedures.

2.3.1 DSMC Overview

In a DSMC simulation, the computational domain is divided into a network of cells. The state of the system is described by the positions and velocities of particles, $\{\mathbf{x}_j, \mathbf{c}_j\}$. The evolution of the system is integrated in time steps, Δt, which are typically smaller than the mean collision time for a particle. At each time step, the particles are first allowed to translate at constant velocity as if they did not interact with each other, that is, their positions are updated to $\mathbf{x}_j + \mathbf{c}_j \Delta t$. Some particles may travel from cell to cell. Some particles may escape from the computational domain or hit a solid wall and bounce back. After all particles have been translated, some are randomly selected to collide. The rules of this random selection are developed from kinetic theory, so as to replicate the correct collision frequency. Momentum and energy are conserved in a collision process.

2.3.2 Variable Hard Sphere Model

Conservation of momentum and energy provide four out of the six equations required to determine the post-collision velocities. The remaining two conditions are made with the assumption of isotropic scattering. The azimuthal angle, ϕ, is uniformly distributed between 0 and 2π, so as $\phi = 2\pi\mathfrak{R}$, where $\mathfrak{R}$ is a uniform deviate in $[0, 1)$. The other angle, θ, is computed from $\sin\theta = 2\mathfrak{R} - 1$.

In determining the collision frequency of a gas molecule, the use of the typical inverse power law potential model is inadequate because the model gives an infinite total cross-section. To overcome this difficulty, Bird [15] introduced the Variable Hard Sphere (VHS) model as a practical approximation to the inverse power law potential model. In the VHS model, isotropic scattering is also assumed and its total cross-section, σ, is allowed to vary with the relative speed of the two colliding

molecules, g, as follows

$$\sigma/\sigma_r = g^{1-2\omega}/\overline{g_r^{1-2\omega}}. \tag{2.19}$$

Here, g_r is the relative collision speed at the reference temperature T_r. Also seen in Equation (2.14), σ_r is the reference cross section and is written as $\sigma_r = \pi d_{\text{ref}}^2$, where d_{ref} denotes the reference molecular diameter. Data for ω and d_{ref} at $T_r = 273$ K for several major species are listed in Table 2.1.

	He	Ar	N_2	O_2	Air
Diameter ($d_{\text{ref}} \times 10^{10}$ m)	2.33	4.17	4.17	4.07	4.19
Viscosity index (ω)	0.66	0.81	0.74	0.77	0.77

Table 2.1: VHS molecular diameters and viscosity indexes for some major species at 273 K.

2.3.3 Coefficient of Viscosity

The coefficient of viscosity obtained from the first approximation of the Sonine polynomials is [83]

$$\mu = \frac{5}{8}\sqrt{\pi m k T}\left(\frac{m}{4kT}\right)^{-4}\left[\int_0^\infty g^7 \sigma_\mu(g) \exp\left(-\frac{mg^2}{4kT}\right) dg\right]^{-1} \tag{2.20}$$

where σ_μ is the viscosity cross section and is given as $\sigma_\mu = 2/3\sigma$ for the VHS model. Using Equation (2.19) and the relation

$$\overline{g_r^{2\omega-1}} = (4kT_r/m)^{\omega-1/2}/\Gamma(5/2-\omega)$$

one can obtain

$$\mu = \frac{15\sqrt{\pi m k T_r}}{2\sigma_r(5-2\omega)(7-2\omega)}\left(\frac{T}{T_r}\right)^\omega.$$

This shows that the form taken by the reference viscosity in Equation (2.14) is necessary.

2.3.4 Collisions

To evaluate the collisions in a DSMC simulation, pairs of particles in a cell are randomly selected, regardless of their relative positions and velocities. In Bird's "No Time Counter" (NTC) scheme [16], a total number of

$$1/2n\bar{N}(\sigma g)_{\max}\Delta t$$

pairs are sampled from the cell at each time step and a collision actually takes place if a candidate pair satisfies

$$(\sigma g)/(\sigma g)_{\max} > \mathfrak{R}.$$

The average number of particles in the cell is denoted by $\bar{N}$. The parameter $(\sigma g)_{\max}$ is stored for each cell and is best set initially to a reasonably large value, but with provision for it to be automatically updated if a larger value is encountered during the sampling.

Baganoff and McDonald [8] developed another sampling scheme suited to vector computers. In their scheme, the condition for a candidate pair to actually collide is

$$\frac{1}{2}n^2\left(\frac{g\sigma_r\Delta t}{S}\right)\left(\frac{g_r}{g}\right)^{2\omega-1} > \mathfrak{R}, \tag{2.21}$$

for a general sample size per unit volume, S. Special care must be taken to ensure that the left-hand-side of Equation (2.21) is never greater than unity in a numerical simulation. This can be achieved by reducing the time step, Δt. As long as the left-hand-side is less than unity, the sampling scheme will model the correct physics.

The sampling scheme developed by Baganoff and McDonald is employed throughout the whole thesis.

2.3.5 Rotational Energy Exchange

In a diatomic or polyatmoic gas, energy is transferred between the various internal modes via continuous collisions and these collisions drive the internal energy distribution toward their equilibrium state. The number of collisions required for a particular mode of each molecule to reach equilibrium is called the collision number Z of that mode. Each internal mode has a different collision number and it is generally the case that

$$Z_{\text{translation}} < Z_{\text{rotation}} < Z_{\text{vibration}}.$$

Since only perfect gases are considered in the thesis, the vibrational energy can be completely ignored. The above relation indicates that the number of collisions for the rotational mode to reach equilibrium is greater than the number required for the translational mode.

The transfer of energy between the various modes is usually implemented into the DSMC method by using the Larsen-Borgnakke phenomenological model [17]. In DSMC simulations, this model usual assumes that a constant number of 1/5 of all collisions are considered to be inelastic and the rest of collisions are perfectly elastic. However, this assumption is in direct opposition to the theoretical findings of Parker [66] and Lordi and Mates [55].

Boyd [19, 20], therefore, developed a temperature-dependent expression for the energy exchange probability. In his expression, the rotational collision number is defined as

$$Z_R = \tau_R/\tau_c,$$

where τ_R is the rotational relaxation time and τ_c is the mean time between collisions. In a collision, energy exchange between the translational and rotational modes takes

place if

$$1+\frac{\Gamma(\zeta+5/2-\omega)}{\Gamma(\zeta+3-\omega)}\left(\frac{k\Theta}{E_c}\right)^{1/2}\frac{\pi^{3/2}}{2}+ \\ \frac{\Gamma(\zeta+5/2-\omega)}{\Gamma(\zeta+3/2-\omega)}\left(\frac{k\Theta}{E_c}\right)\left(\frac{\pi^2}{4}+\pi\right)>\frac{(Z_R)_\infty}{Z_t}\mathfrak{R}, \quad (2.22)$$

where Θ is the characteristic temperature of the intermolecular potential and $(Z_R)_\infty$ is the limiting value. The sum of the translational and internal collision energies is denoted by E_c and translational collision number by Z_t with definition similar to Z_R.

2.3.6 Boundary Conditions

The velocity distribution for simulated particles reflecting from a solid wall varies with the type of the wall they hit. Specular and diffuse walls are the two most common types considered in DSMC. When a particle collides with a specular wall, its component of velocity tangential to the wall remains the same and the component normal to the wall changes its sign. When a particle bounces back from a diffuse wall at temperature T_w, its velocity components tangential to the wall are sampled from the standard Maxwellian distribution

$$f(c_t)\,dc_t=\frac{1}{\sqrt{2\pi RT_w}}\exp\left(\frac{-c_t^2}{2RT_w}\right), \quad (2.23)$$

while its normal component is sampled from the biased-Maxwellian distribution

$$f(c_n)\,dc_n=\frac{1}{RT_w}c_n\exp\left(\frac{-c_n^2}{2RT_w}\right). \quad (2.24)$$

A wall with accommodation coefficient α means that a fraction α of all the particles colliding with the wall are thermalized by the wall and the rest fraction $(1-\alpha)$ of the particles are specularly reflected by the wall.

The internal energy of a reflecting particle is handled in the same manner. When a particle strikes a specular wall, its internal energy experiences no change. On the

other hand, when a particle strikes a diffuse wall, its internal energy is reset according to the standard Maxwellian distribution evaluated at the wall temperature.

2.3.7 Limitations of DSMC

The procedures in the DSMC method for the probabilistic selection of a representative set of collisions are directly based on the basic relations of classical kinetic theory. As a result, this method has the same limitations as in all of classical kinetic theory, including the Boltzmann equation. The principal limitations are the assumption of molecular chaos and the requirement of a dilute gas. The molecular chaos assumption means that particles undergoing a collision will not meet again before colliding with other particles many times. The velocities of a collision pair are, therefore, totally uncorrelated. The dilute gas assumption prevents this method from being used for dense gases or for highly ionized plasmas that are dominated by long-range interactions [16].

Another fundamental assumption for DSMC is that particle motion and particle collisions can be decoupled. This assumption requires that the simulation time-step (Δt) be smaller than the local mean collision time (τ). In addition, we are able to randomly select the colliding particles in a cell while ignoring their positions if the computational cell size (Δs) is smaller than the local mean free path (λ), statistically speaking. In other words, we need $\Delta t/\tau < 1$ and $\Delta s/\lambda < 1$.

2.3.8 MONACO

The particular DSMC code, named MONACO, employed in the thesis was first developed by Dietrich and Boyd [30] in 1996. Since then, MONACO has been further modified and applied to a wide variety of rarefied gas problems. It is a general-purpose code for simulating 2D, axi-symmetric, or 3D rarefied gas flows. MONACO

employs the VHS or Variable Soft Sphere [54] (VSS) collision models, the variable rotational energy exchange probability model of Boyd [19, 20], and the variable vibrational energy exchange probability model of Vijayakumar *et al.* [82] although this model is turned off due to the perfect gas assumption. Cell weighting factors and time-steps may be set uniquely for each cell in the grid. A sub-cell scheme is implemented for selection of collision pairs where the number of sub-cells is scaled by the local mean free path.

2.4 The Information Preservation Method

2.4.1 Governing Equations

The Information Preservation (IP) method was first developed by Fan and Shen [33] to overcome the statistical scatter problem in DSMC simulations, especially for systems in which the flow speed is much smaller than the molecular speed. In addition to the ordinary microscopic molecular velocity that is utilized to compute the particle trajectory, each simulation particle in the DSMC-IP method also possesses macroscopic preserved information such as velocity vector ($\boldsymbol{\xi}$) and temperature (T). As a result, the DSMC-IP method uses at most 57% more memory than in the standard DSMC method [77]. This method has achieved great success for solving micro-scale gas flows [24, 32, 79].

At each time step of the DSMC-IP method, simulated particles are first moved and collided in the usual way as in the standard DSMC method. The preserved velocity and temperature of the j-*th* simulated particle in a cell are updated by

solving

$$\frac{\partial}{\partial t}\left(\rho_c \boldsymbol{\xi}_j\right) = -\nabla p_c \tag{2.25}$$

$$\frac{\partial}{\partial t}\left(\frac{1}{2}\rho_c\left(\xi_j^2 + \zeta\, R\, T_j\right)\right) = -\nabla \cdot \left(p_c\, \mathbf{V}_c\right). \tag{2.26}$$

After the preserved information of simulated particles is updated, the preserved information for a cell is updated by taking the arithmetic average over the information of all N particles in the cell,

$$\mathbf{V}_c = \frac{1}{N}\sum_{j=1}^{N} \boldsymbol{\xi}_j \tag{2.27}$$

$$T_c = \frac{1}{N}\sum_{j=1}^{N} \left(T_j + T_{a,j}\right). \tag{2.28}$$

The density is updated by solving the continuity equation

$$\frac{\partial \rho_c}{\partial t} + \nabla \cdot \left(\rho_c\, \mathbf{V}_c\right) = 0. \tag{2.29}$$

The ideal gas law, $p = \rho RT$, is assumed again. The reason for the additional temperature term, T_a, in Equation (2.28) will be given in the next section.

Equations (2.25) and (2.26) are solved using a finite-volume method as

$$\boldsymbol{\xi}_j^{t+\Delta t} - \boldsymbol{\xi}_j^{t} = -\frac{\Delta t}{\rho_c A}\sum_{\text{edges}} p_c\, \mathbf{n}\, \Delta s \tag{2.30}$$

$$\left(\xi_j^2 + \zeta\, R\, T_j\right)^{t+\Delta t} - \left(\xi_j^2 + \zeta\, R\, T_j\right)^{t} = -\frac{2\Delta t}{\rho_c A}\sum_{\text{edges}} (p_c\, \mathbf{V}_c \cdot \mathbf{n})\Delta s \tag{2.31}$$

where $\mathbf{n} = (\Delta y/\Delta s, -\Delta x/\Delta s)$ is the unit vector normal to the cell edge. The cell information on cell edges is linearly interpolated using the information of the neighboring cells. For axisymmetric flows, Equation (2.31) is modified to

$$\left(\xi_j^2 + \zeta\, R\, T_j\right)^{t+\Delta t} - \left(\xi_j^2 + \zeta\, R\, T_j\right)^{t} = -\frac{2\Delta t}{\rho_c A y_c}\sum_{\text{edges}} \bar{y}(p_c\, \mathbf{V}_c \cdot \mathbf{n})\Delta s \tag{2.32}$$

to take into account the effect that the cell has been rotated about the axis of symmetry.

In contrast, the continuity equation, (2.29), must be solved using an adequate numerical scheme due to the possible presence of shock waves in supersonic flows. Since the same equation also appears in the Navier-Stokes equations, the same technique described in Section 2.2.2 is used to solve it.

2.4.2 Additional Temperature

The additional temperature term, T_a, in Equation (2.28) was first introduced by Sun and Boyd [78] to solve the contradiction between the real energy flux and the DSMC-IP representation of the translational energy flux across a cell interface. From gas kinetic theory, the volume averaged translational energy of a molecule at equilibrium temperature T is $3kT/2$, whereas the average translational energy carried by a molecule across an interface at equilibrium is $2kT$. The extra energy, $kT/2$, can be regarded as being "borrowed" from other molecules that do not move across the interface. This energy must be taken into account or the energy of the whole system will not be conserved. Accordingly, each simulation particle in the IP method has an additional temperature T_a and each cell also has an additional temperature $T_{a,c}$ to keep track of the borrowed energy. A more detailed description and implementation of T_a in the DSMC-IP method can be found in Reference [78].

When a simulated particle moves from one cell to the other, the additional temperatures for the particle and for the cell are changed as

$$T'_{a,j} = (T_j - T_{\text{ref}})/(3+\zeta), \tag{2.33}$$

$$T'_{a,c} = T_{a,c} + T_{a,j} - T'_{a,j} \tag{2.34}$$

where T_{ref} is the cell interface temperature interpolated from the preserved cell tem-

peratures of neighboring cells. When a particle bounces back from a specular wall, the additional temperature changes are

$$T'_{a,j} = -T_{a,j},$$
$$T'_{a,c} = T_{a,c} + T_{a,j} - T'_{a,j}.$$

Or, when a particle bounces back from a diffuse wall, the changes are

$$T''_{a,j} = (T_j - T_{\text{ref}})/(3+\zeta),$$
$$T'_{a,c} = T_{a,c} + T_{a,j} - T''_{a,j},$$
$$T'_{a,j} = (T_w - T_{\text{ref}})/(3+\zeta)$$

where $T_{\text{ref}} = \sqrt{T_j\, T_w}$ is the constant gas temperature of a collisionless flow between two plates with one at T_j and the other at T_w [40].

It has been numerically demonstrated that the idea of the additional temperature performs excellently for flows in which nonequilibrium is insignificant, such as Couette flow, Rayleigh flow, Mach 0.8 airflow over a NACA0012 airfoil with a chord length of 4 cm [78] and Mach 0.2 airflow over a 20-micron-long flat plate [80].

2.4.3 Collision

In a $(\mathbf{c}_1, \mathbf{c}_2) \to (\mathbf{c}_1^*, \mathbf{c}_2^*)$ collision, the macroscopic preserved properties of the two particles involved change based on a phenomenological model [78]

$$\boldsymbol{\xi}_1^* = \Lambda_\mu\, \boldsymbol{\xi}_1 + (1-\Lambda_\mu)\, \boldsymbol{\xi}_2, \tag{2.35a}$$
$$\boldsymbol{\xi}_2^* = (1-\Lambda_\mu)\, \boldsymbol{\xi}_1 + \Lambda_\mu\, \boldsymbol{\xi}_2, \tag{2.35b}$$
$$T_1^* = \Lambda_\kappa T_1 + (1-\Lambda_\kappa) T_2 + T_{\xi_1-\xi_2}, \tag{2.35c}$$
$$T_2^* = (1-\Lambda_\kappa) T_1 + \Lambda_\kappa T_2 + T_{\xi_1-\xi_2}, \tag{2.35d}$$

and

$$T^*_{a,1} = \Lambda_\kappa T_{a,1} + (1 - \Lambda_\kappa) T_{a,2}, \tag{2.35e}$$

$$T^*_{a,2} = (1 - \Lambda_\kappa) T_{a,1} + \Lambda_\kappa T_{a,2}. \tag{2.35f}$$

The quantity $T_{\xi_1 - \xi_2}$ in Equations (2.35c) and (2.35d) is due to the relative energy

$$T_{\xi_1 - \xi_2} = (\boldsymbol{\xi}_1 - \boldsymbol{\xi}_2)^2 (1 - C_\mu^2 \cos^2 \chi)/(4\,\zeta\, R).$$

The weighting factors Λ_μ and Λ_κ are functions of the deflection angle χ after collision in the collision plane

$$\Lambda_\mu = \frac{1 + C_\mu \cos(\chi)}{2}, \qquad \Lambda_\kappa = \frac{1 + C_\kappa \cos(\chi)}{2}$$

where C_μ and C_κ are dependent only upon gas species and obtained from numerical experiments. A list of values of C_μ and C_κ for five different gases is given in Table 2.2 for the VHS model.

	He	Ar	N_2	O_2	Air
C_μ	-0.15	-0.18	-0.25	-0.21	-0.21
C_κ	1.15	1.28	0.87	0.87	0.87

Table 2.2: Values of C_μ and C_κ for the VHS molecular model.

2.5 New Energy Flux Model for the DSMC-IP

The additional temperature in the DSMC-IP method is actually evaluated as $(T_j - T_{\text{ref}})/(3 + \zeta)$, as shown in Equation (2.33), by assuming that there is a counterpart particle at temperature T_k moving in the opposite direction and carrying extra energy $k(T_k - T_{\text{ref}})/(3 + \zeta)$ across the same interface. Although the IP method

works well for insignificantly nonequilibrium flows, a numerical experiment of a supersonic flow over a 2-D wedge [88] showed that this method expresses a clear flaw near the leading edge and within the shock, where the flow is believed to be strongly nonequilibrium.

As Mach number is increased to hypersonic conditions, the accuracy of the IP method becomes very poor. A typical example for a Mach 5 shock in argon is displayed in Figure 2.2 in which the results obtained with the IP method are compared with DSMC results. The upstream conditions are $T_1 = 300$ K, $\rho_1 = 1.068 \times 10^{-4}$ kg/m^3 and $a_1 = 322.6$ m/s. The non-dimensional variable is defined as

$$Q^* = \frac{Q - Q_{\text{ref}}}{|Q_2 - Q_1|},$$

where the subscripts 1 and 2 represent upstream and downstream of the shock, respectively. Q_{ref} is ρ_1 and T_1 for density and temperature and u_2 for velocity. In the numerical simulation, the reference time step is 10 nsec and the number of particles per cell in the upstream is about 30 on average. It is clear that the IP method is unable to accurately predict the profile of any of the flow properties. Moreover, because the IP results fail to predict the onset of nonequilibrium at the upstream edge of the shock, the domain interface in a hybrid DSMC/CFD simulation is placed at the wrong location. As a result, the particle domain is always too small. Numerical experiments showed that doubling the number of particles per cell does not resolve the poor prediction. It is really no surprise because the idea of how the IP approach deals with the energy carried by simulation particles from cell to cell is based on the assumption of local thermal equilibrium or weak nonequilibrium.

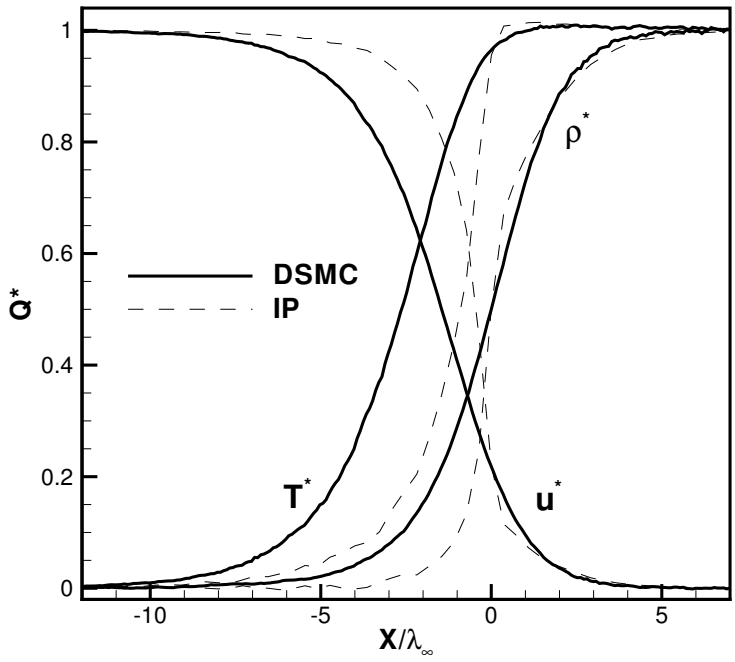

Figure 2.2: Non-dimensional flow properties for a Mach 5 shock in argon.

2.5.1 Construction of F

Since a simulated particle j represents a large number of real molecules, it is reasonable to assume that the real molecules are in some kind of velocity distribution characterized by $\boldsymbol{\xi}_j$ and T_j. In the thesis, the distribution is assumed to be Maxwellian

$$\mathcal{M}_j = \frac{1}{(2\pi RT_j)^{3/2}} \exp(-\frac{|\mathbf{c} - \boldsymbol{\xi}_j|^2}{2RT_j}). \tag{2.36}$$

The local velocity distribution function within a cell with N simulation particles is then assumed to be the arithmetic average of all $\mathcal{M}_j$ in the cell

$$F_c = \frac{n}{N} \sum_{j=1}^{N} \mathcal{M}_j. \tag{2.37}$$

Notice that it is not necessary for the F_c to be Maxwellian. For the sake of simplicity, summation always means from $j = 1$ to N and its upper and lower limits are dropped from now on.

With the above assumption of the local velocity distribution function in a cell, cell velocity and temperature can be determined using Equations (2.4) and (2.6), respectively, and are

$$\mathbf{V}_c = \frac{1}{N}\sum \boldsymbol{\xi}_j, \tag{2.38}$$

$$T_c = \frac{1}{N}\sum \frac{1}{3R}\left|\boldsymbol{\xi}_j - \mathbf{V}_c\right|^2 + T_j. \tag{2.39}$$

Notice that Equation (2.38) is identical with Equation (2.27). Also, notice that T_c is always positive as long as every particle in the cell has a positive IP temperature.

In a strong shock wave, since the pressure is not in equilibrium in all directions, the change of the preserved velocity modeled with Equation (2.25) is not valid any more. As a result, a more general pressure gradient term is involved

$$\frac{\partial}{\partial t}\left(\rho_c \boldsymbol{\xi}_j\right) = -\nabla \cdot \mathcal{P}_c \tag{2.40}$$

where $\mathcal{P}_c$ consists of only the diagonal elements of the pressure tensor

$$\mathbf{P} = m\int_{\mathbb{R}^3} (\mathbf{c}-\mathbf{V})(\mathbf{c}-\mathbf{V})F\, d\mathbf{c}.$$

Substituting F with Equation (2.37) and integrating over the velocity space yields the elements of the pressure tensor

$$\mathcal{P}_{ik} = \delta_{ik}\frac{\rho}{N}\sum(\xi_{j,i}-V_{c,i})(\xi_{j,k}-V_{c,k}) + RT_j$$

where δ_{ik} is the Kronecker delta.

To solve the energy and continuity equations (Equations (2.26) and (2.29), respectively), energy and mass fluxes across a cell interface must be evaluated. A general expression of the flux of $Q(\mathbf{c})$ across a cell interface can be written as

$$J_Q = \int_{\mathbb{R}^2\times\mathbb{R}^+} c_n Q F_c d\mathbf{c}, \tag{2.41}$$

where c_n is the velocity component in the direction normal to the cell interface and is given as $c_n = \mathbf{c} \cdot \mathbf{n}$. One integration in Equation (2.41) has been limited to those molecules moving in the positive $\mathbf{n}$-direction. Mass and energy fluxes can be obtained when Q in Equation (2.41) is replaced with m and $m(c^2 + \zeta RT)/2$. With the help of Equations (2.36) and (2.37), the fluxes can be evaluated as

$$J_m = \frac{1}{N} \sum J_{m,j}, \tag{2.42}$$

$$J_e = \frac{1}{N} \sum J_{m,j} \left[\xi_j^2 + (5+\zeta)RT_j\right]/2 - \rho_c RT_j \bar{c}_j \exp(-s_j^2)/8. \tag{2.43}$$

Here, $J_{m,j}$ is the mass flux resulting from the simulated particle j

$$J_{m,j} = \frac{1}{2}\rho_c \beta_j^{-1} \left\{ s_j \left[1 + \mathrm{erf}(s_j)\right] + \exp(-s_j^2)/\sqrt{\pi} \right\}, \tag{2.44}$$

where $\bar{c}_j = \sqrt{8RT_j/\pi}$, $s_j = \beta_j \xi_{n,j}$ is the speed ratio, $\beta_j^{-1} = \sqrt{2RT_j}$ and $\mathrm{erf}(x)$ is the error function. The IP velocity component in the direction normal to the interface is written as $\xi_{n,j} = \boldsymbol{\xi}_j \cdot \mathbf{n}$.

The rates of change of the density and average energy in a cell are approximated using the surface integrals with respect to the mass and energy fluxes around the cell boundary

$$\rho_c^{t+\Delta t} - \rho_c^t = -\frac{\Delta t}{A} \sum_{\text{edge}} J_m \Delta s \tag{2.45a}$$

$$(\rho_c E_c)^{t+\Delta t} - (\rho_c E_c)^t = -\frac{\Delta t}{A} \sum_{\text{edge}} J_e \Delta s \tag{2.45b}$$

for two-dimensional flows or

$$\rho_c^{t+\Delta t} - \rho_c^t = -\frac{\Delta t}{A y_c} \sum_{\text{edge}} \bar{y} J_m \Delta s \tag{2.46a}$$

$$(\rho_c E_c)^{t+\Delta t} - (\rho_c E_c)^t = -\frac{\Delta t}{A y_c} \sum_{\text{edge}} \bar{y} J_e \Delta s \tag{2.46b}$$

for axi-symmetric flows. A net flux consists of the outlet flux from the cell and the inlet flux from the neighboring cell.

A similar approach was proposed in the Equilibrium Flux Method (EFM) by Pullin [67], but there were no particles involved and all fluxes were evaluated based on cell averaged values. Shen *et al.* [75] attempted to calculate the energy flux in a fashion close to that described here, but they assumed that all particles within a cell have the same preserved information.

Particle IP temperature is updated by assuming that all particles within a cell bear the same amount of temperature change

$$\Delta T = \{E_c - \frac{1}{N}\sum(\frac{1}{2}\xi_j^2 + c_v T_j)\}/c_v.$$

If ΔT is positive, particle temperature in the cell increases and everything is well defined. However, when ΔT is negative, care must be taken to prevent the particle IP temperature from becoming negative or lower than a cut-off temperature T_θ. Therefore an iterative process is employed to update the particle temperature. The loop process starts with a test of each individual particle in a cell to examine whether the particle IP temperature is lower than T_θ when ΔT is applied. If the test is false, the temperature update for the individual particle is allowed. Otherwise, the temperature update is not allowed and an amount of ΔT is banked. After all particles in the cell are finished with the update for a loop, the banked temperature is divided by the number of particles in the cell and the result is a new ΔT whose absolute value is less than the last one. The loop repeats with the new ΔT until there is no banked temperature. From the experience of numerical experiments, the number of loops is always smaller than 50. T_θ is arbitrarily chosen to be 5% of the local cell temperature.

2.5.2 Shock Structure

The new energy flux model is evaluated using 1-D stationary shock wave simulations. A computational domain that is sufficiently large to contain the shock is employed. Particles entering the computational domain from the upstream side are initialized with the upstream conditions. A moving piston boundary described in the book by Bird [16] is applied at the downstream edge. IP properties of the particles reflecting from the moving piston back to the computational domain are set with the downstream conditions.

To emphasize the great improvement by the new energy flux model, only the Mach 5 shock in argon mentioned previously is considered in this section. The results at different Mach numbers and gases can be found in Appendix A or Reference [86]. The reference time step in the numerical simulation with the new energy flux model is 10 nsec and the number of particles per cell in the upstream is about 30.

At Mach number 5, the IP method with the new energy flux model works very well. Comparisons for non-dimensional density, temperature, and velocity of the IP and DSMC methods are displayed in Figure 2.3. It is obvious that the new solution obtained with the new energy flux model is significantly improved, compared to the solution obtained with the additional temperature model. The newly predicted density profile is in excellent agreement with the DSMC results but the discrepancy of the temperature at the shock front still persists. Because for each time step every particle in a cell is taken into account for the flux evaluations, the new energy flux model is slower than the additional temperature model in which only the particles across the cell edges need to be concerned about the extra energy carried away from the cell. The use of time-consuming functions, exp and erf, in the flux evaluations makes the new energy flux model further slower. This issue will be addressed in

the next section. Overall, the new energy model performs much better than the additional temperature model when the same reference time step and number of particles are employed.

2.5.3 Cost and Boundary Condition

It is worth pointing out that the new energy flux model is a very general idea and is believed to work not only for hypersonic flows but also for subsonic and low-speed microscale flows. However, there are three major issues that prevent it from being immediately employed in the current DSMC/CFD hybrid approach. First, numerical efficiency is very poor primarily because two time-consuming functions, exp and erf, are largely involved in Equations (2.42) and (2.43) for flux evaluations. This issue can be resolved by utilizing faster, approximated functions to replace the built-in exact functions. This issue can also be resolved by creating a look-up table containing the value in the curved parenthesis in Equation (2.44) as a function of the speed ratio s_j. Second, the model is sensitive to the number of particles per cell. Numerical experience suggests that it is required to have at least 30 particles in each cell. Combining these two issues implies that the energy flux model is very expensive computationally. The third issue is associated with the development or adoption of a gas-surface boundary condition. This is not an easy task and will be discussed in the last chapter.

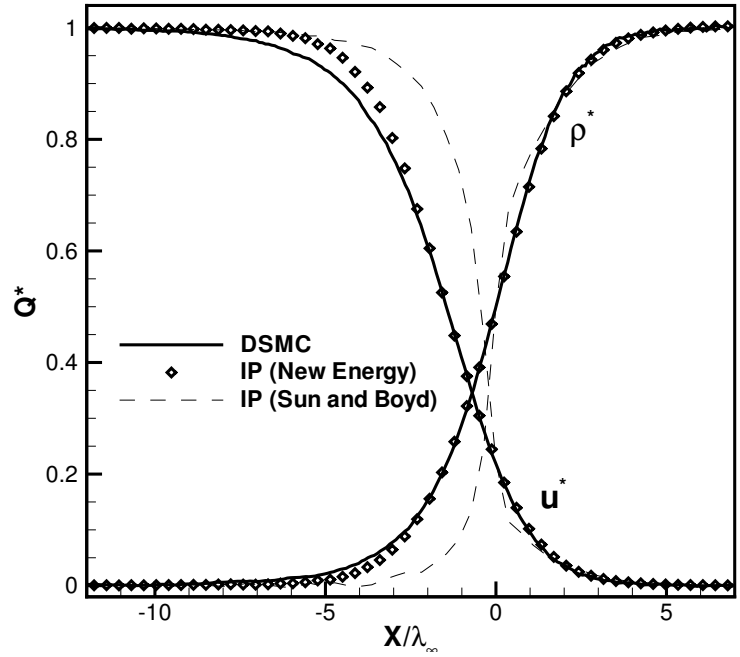

(a) Comparison of density and velocity.

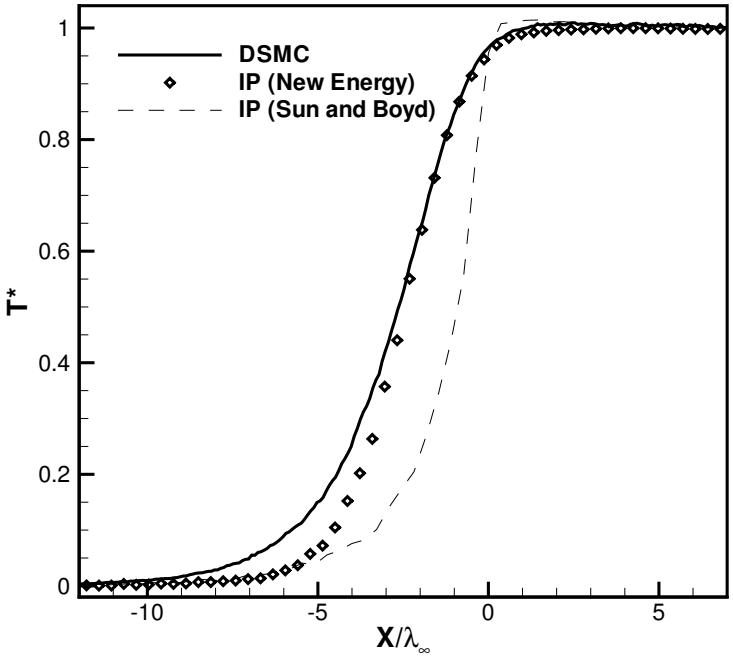

(b) Comparison of translational temperature.

Figure 2.3: Comparison of non-dimensional flow properties for a Mach 5 shock in argon.

CHAPTER III

CODE VALIDATION

Before any study of a hybrid method can be undertaken, a verification of the accuracy and consistency of the constituent numerical methods is required. In this chapter, a number of accuracy issues for the numerical simulations over a blunted cone tip and a hollow cylinder/flare configurations using three numerical methods (NS solver, DSMC, and DSMC-IP) are carefully investigated. For DSMC simulations, solution dependence on numerical parameters, grid resolution, and accommodation coefficient is first examined. The comparisons of DSMC solutions with those obtained with the NS solver and the DSMC-IP method follow.

The gas considered in the entire thesis is pure nitrogen and some of its material properties considered in Chapter II can be found in Tables 2.1 and 2.2. The Prandtl number is assumed to be a constant of 0.72. The freestream conditions are listed in Table 3.1. The conditions for the blunted cone tip and the hollow cylinder/flare correspond, respectively, to the experiments Run 31 and Run 11 conducted in CUBRC [50]. The Reynolds numbers are based on the characteristic lengths in Figure 1.2 and the wall temperature in either case is assumed to be isothermal.

The significant difference between the translational and vibrational temperatures in the freestreams is due to vibration relaxation lagging behind during the rapid

	Blunted Cone Tip	Hollow Cylinder/Flare
M_∞	12.6	12.4
T_∞ (K)	104.4	95.6
T_{wall} (K)	297.2	297.2
V_∞ (m/s)	2630.4	2484.1
ρ_∞ (10^{-4}kg/m^3)	5.618	5.566
T_{vib} (K)	2680.2	2486.7
Re_L (10^4)	6.21	6.35
Kn_L (10^{-4})	9.236	8.264
Kn_R	0.013	-

Table 3.1: Freestream conditions for the flows considered.

expansion of the gas from a high temperature/pressure reservoir tank [26]. Since either experiment lasts only a few millisecond, the assumptions of frozen vibrational energy and vanished vibrational energy accommodation coefficient are therefore made through out all numerical calculations in the thesis. The latter assumption has been verified in many early analytic and experimental work [58].

Notice that if the Knudsen number is evaluated with the characteristic length, the flow field in both cases can be considered as continuum. If the number is evaluated with the cone tip radius in the blunted cone tip case (Kn_R), it is clear that the flow in the vicinity of the cone tip is classified as transitional and should be best simulated with a particle method.

3.1 Blunted Cone Tip

The configuration employed in this case is a blunted 25° half-angle cone as the first cone depicted in Figure 1.2(a). The finest grid used in the code validation has 600 cells along the cone body and 300 cells normal to the body, as shown in

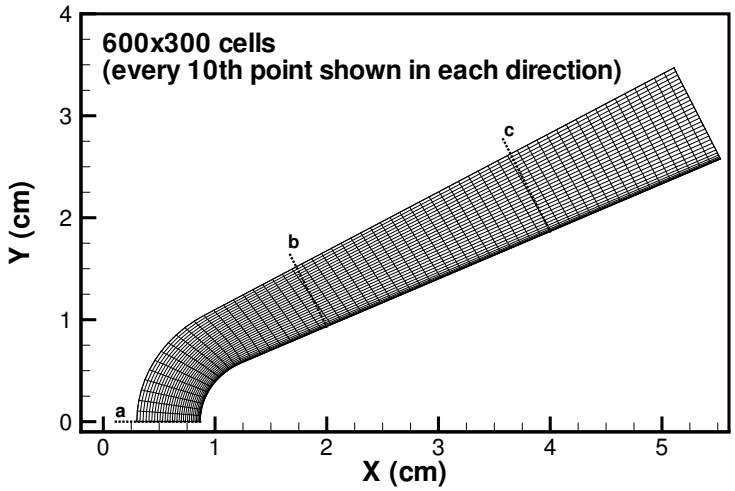

Figure 3.1: Grid employed for a 25° blunted cone.

Figure 3.1. It has increased cell density near the body in order to resolve the local high gradients.

A reference time step of 2 nsec is employed in all the DSMC calculations. The total number of particles in each simulation is about 30 times the total number of cells. A total of 200,000 time steps of computation are performed and the last 20,000 time steps are sampled to obtain the DSMC results. Particles reflecting from the cone surface are assumed to be fully diffuse, $\alpha = 1$, unless otherwise stated.

3.1.1 Numerical Parameters

As described in Section 2.3.7, a fundamental assumption for DSMC is that particle motion and particle collisions can be decoupled and this assumption requires that the simulation time-step be smaller than the local mean collision time, meaning $\Delta t/\tau < 1$. An other numerical requirement for DSMC is to have the cell size smaller than the local mean free path, $\Delta s/\lambda < 1$, making random selections of collision pairs within a cell physically reasonable assumption.

To study the numerical parameters employed, data have been extracted along

three different lines: one along the stagnation line and the other two normal to the cone at $x = 2$ and 4 cm (corresponding to the dotted lines a, b, and c in Figure 3.1, respectively). Figure 3.2 shows the ratio of the simulation time-step to the local mean collision time, with the definition of δn as the normal-distance from the body surface. It is evident that the simulation time-step criterion is satisfied everywhere.

The characteristic cell size in the grid, Δs, is determined by the length scale of a cell in the direction of the maximum gradient of density, pressure, temperature, or velocity and passing through the cell center. Its ratio to the local mean free path is shown in Figure 3.3. The cell size criterion is generally satisfied, except in the shock region in some places along the normal line at $x = 4$ cm. Even in the worst condition, the cell size is no more than twice the local mean free path. In addition, there are at least 40 particles per cell in the shock region as shown in Figure 3.4, and therefore the use of the sub-cell scheme should provide adequate spatial resolution. It is important to note that the criteria for Δt and Δs are met within the boundary layer, which gives one confidence with the DSMC solution in the vicinity of the cone surface.

3.1.2 Grid Sensitivity

In this section, the computed surface quantities at different levels of grid resolution are examined. The two surface quantities considered are pressure coefficient and Stanton number:

$$C_p = \frac{p - p_\infty}{\frac{1}{2}\rho_\infty V_\infty^2}, \qquad St = \frac{q_w}{\frac{1}{2}\rho_\infty V_\infty^3}$$

and they are plotted versus the axial distances.

In Figure 3.5, the surface pressure and Stanton number are shown for the steady state solution. It is clear that the two surface quantities in the two grids are very

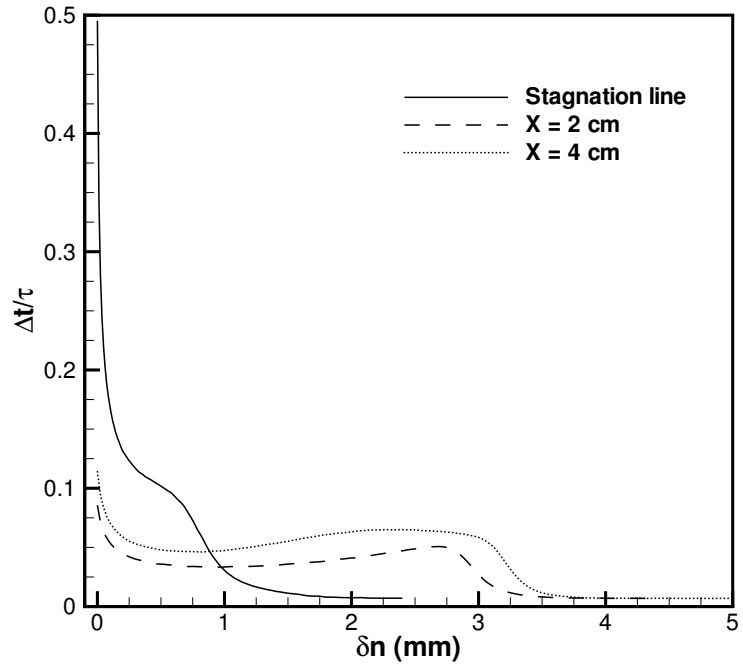

Figure 3.2: Ratio of simulation time-step to local mean collision time along three different lines normal to a 25° blunted cone.

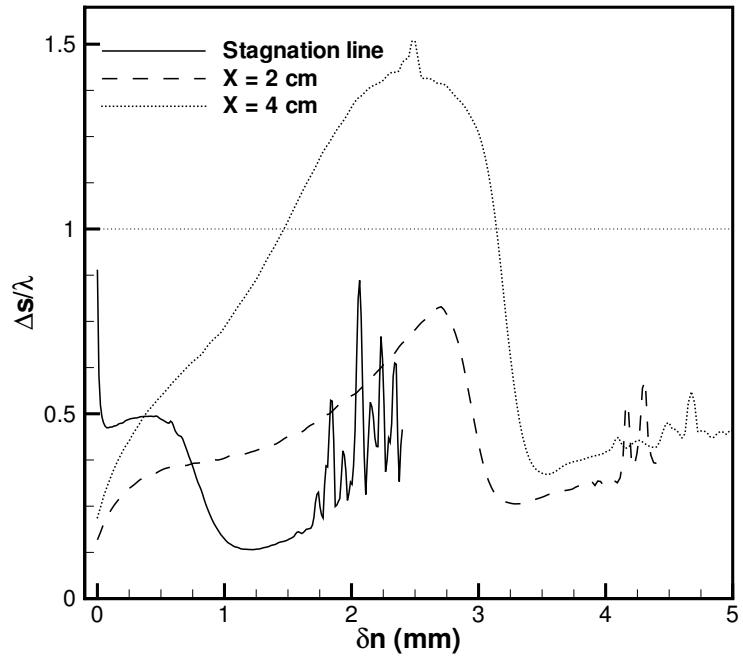

Figure 3.3: Ratio of simulation cell size in direction of maximum gradient to local mean free path along three different lines normal to a 25° cone.

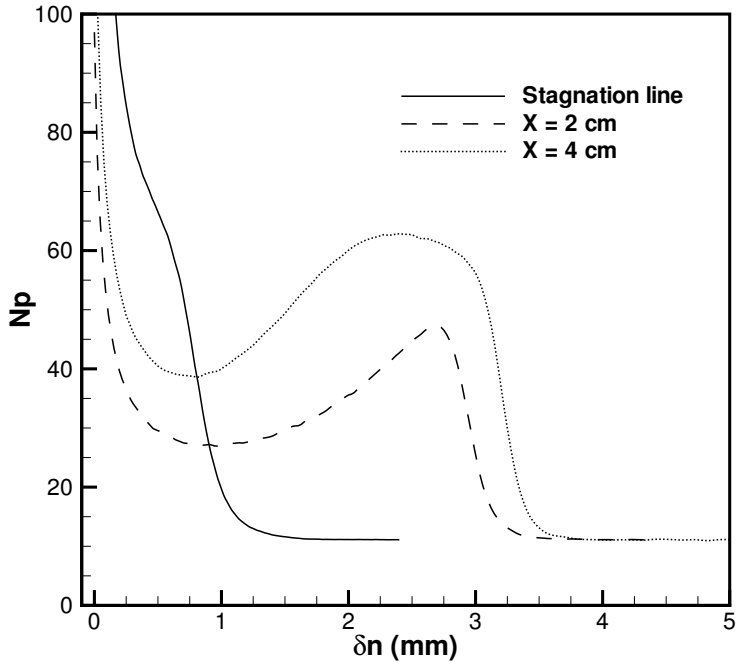

Figure 3.4: Number of particles per cell along three different lines normal to a 25° blunted cone.

close and it is believed that the 600 by 300 grid yields a reliable solution in terms of grid sensitivity and thereafter is used for the further studies of this case.

On a Linux cluster with 20 1-GHz Intel® Pentium® III processors, the time consumed for the simulation on the 600 by 300 grid is about 32 hours. On the same machine but on the 400 by 200 grid, the run time is about 16 hours.

3.1.3 Accommodation Coefficient

The surface pressure coefficient and Stanton number computed with two different accommodation coefficients are displayed in Figure 3.6. It is indicated that only minor differences are observed. From this study, it is concluded that the DSMC results are insensitive to the accommodation coefficient in the range from 0.85 to 1.0.

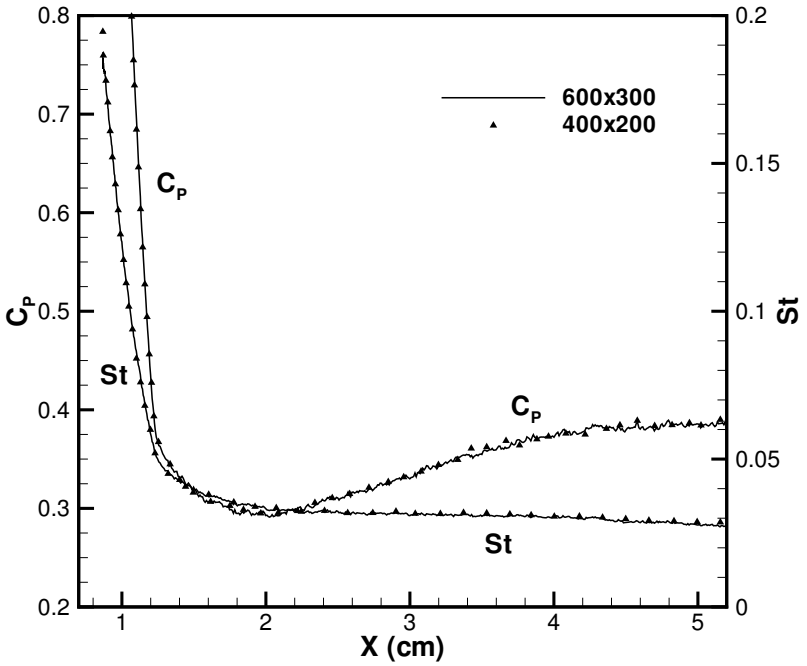

Figure 3.5: Surface pressure and heat transfer coefficients obtained with DSMC at different levels of grid resolution along a 25° blunted cone surface.

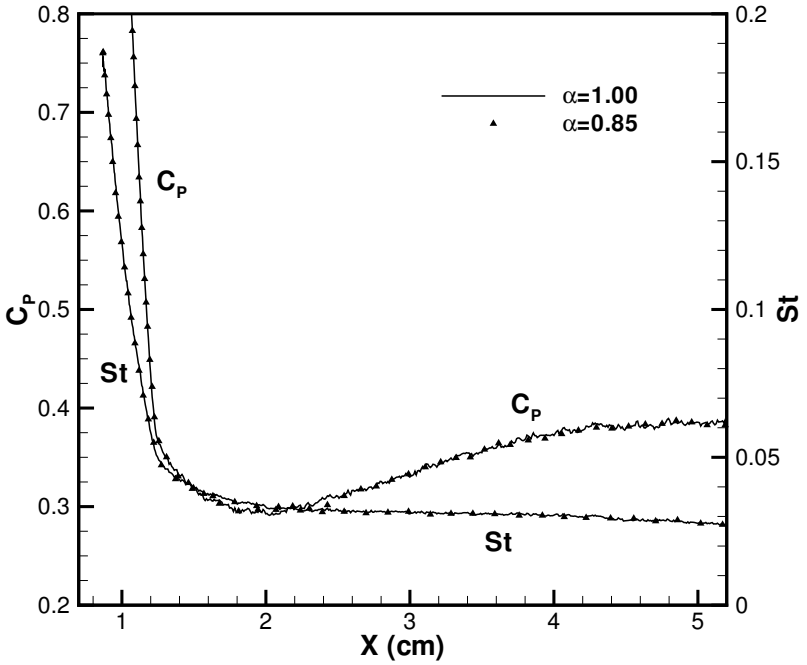

Figure 3.6: Surface pressure and heat transfer coefficients with $\alpha = 0.85$ and 1.0 along a 25° blunted cone surface.

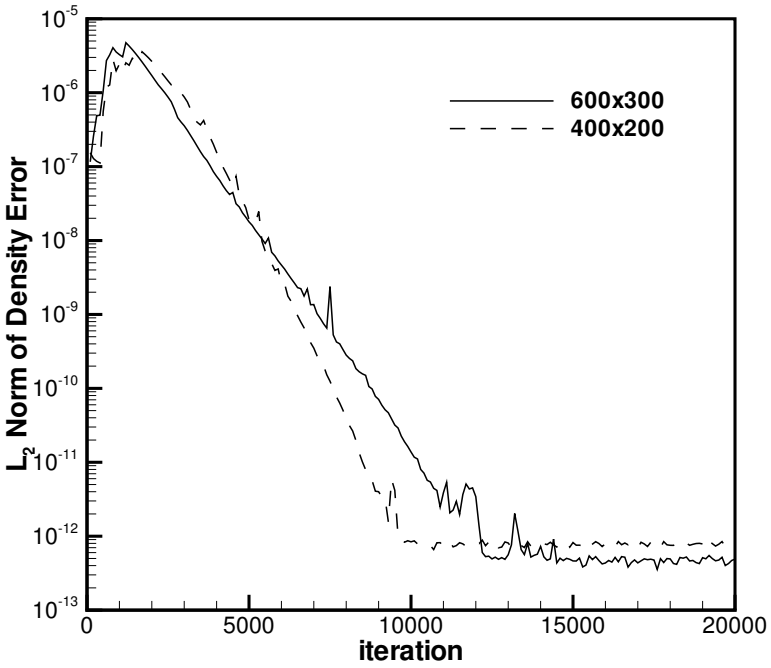

Figure 3.7: Convergence histories for the CFD simulations at different levels of grid resolution for a Mach 12.6 nitrogen flow over a 25° blunted cone.

3.1.4 DSMC and CFD Comparisons

The convergence histories are shown in Figure 3.7 for the CFD simulations obtained with the implicit scheme in the 400 by 200 and 600 by 300 grids. The times required by the CFD calculations on the same Linux cluster machine are 20 and 45 minutes, respectively, for the coarse and fine grids. The surface pressure and heat transfer coefficients for the CFD solutions at different levels of grid resolution are displayed in Figure 3.8 and it is clear that the two surface quantities in the two grids are very close. The CFD solution in the 600 by 300 grid is used in the following validations.

Comparisons of the translational temperature and mass density contours obtained with the DSMC and CFD methods are made in Figure 3.9. It is easy to observe that the bow shock predicted by DSMC is much thicker. Moreover, its positions in front of the cone tip predicted by the two methods are different, as shown in Figure 3.9(b).

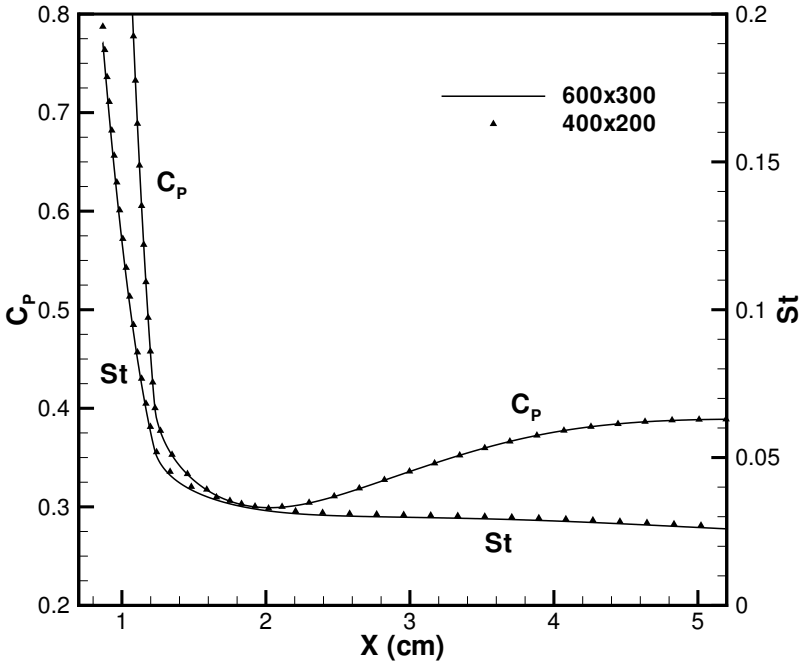

Figure 3.8: Surface pressure and heat transfer coefficients obtained with CFD at different levels of grid resolution along a 25° blunted cone surface.

Otherwise, the DSMC method results are in general in good agreement with the CFD results.

In Figure 3.10, the pressure and heat transfer coefficients obtained with the DSMC and CFD methods are compared with the experimental data [50] along the cone surface. Although the numerical results are slightly over-predicted for both C_p and St, they still agree with the measured data fairly well.

It is worth pointing out that the C_p and St calculated by both numerical methods are very close along the cone surface, suggesting that the flow fields in the boundary layer should be very similar in both numerical solutions. Detailed comparisons of the flow fields for the DSMC and CFD solutions are provided in Chapter VI.

Also shown in Figure 3.10(a) is the profile based on Lees' modified Newtonian law [7]

$$C_p = C_{p_{\max}} \sin^2 \theta \tag{3.1}$$

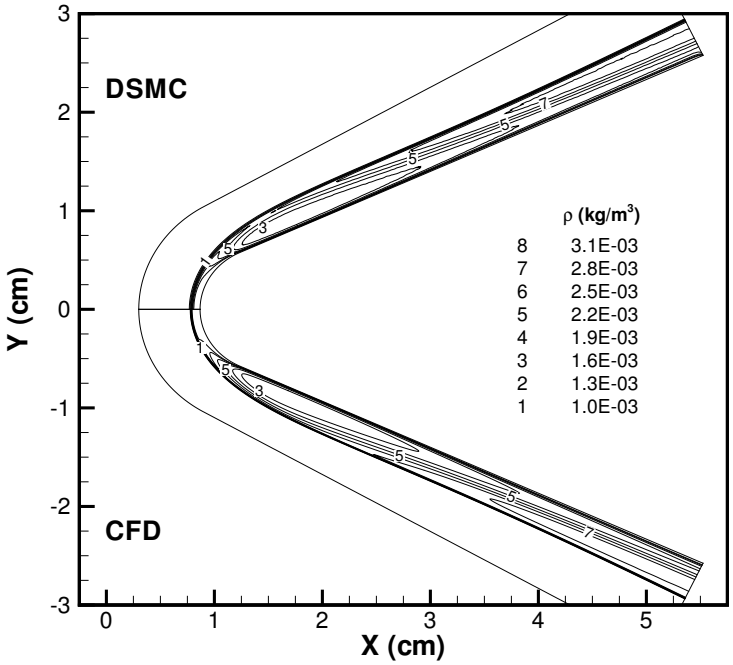

(a) Comparison of mass density.

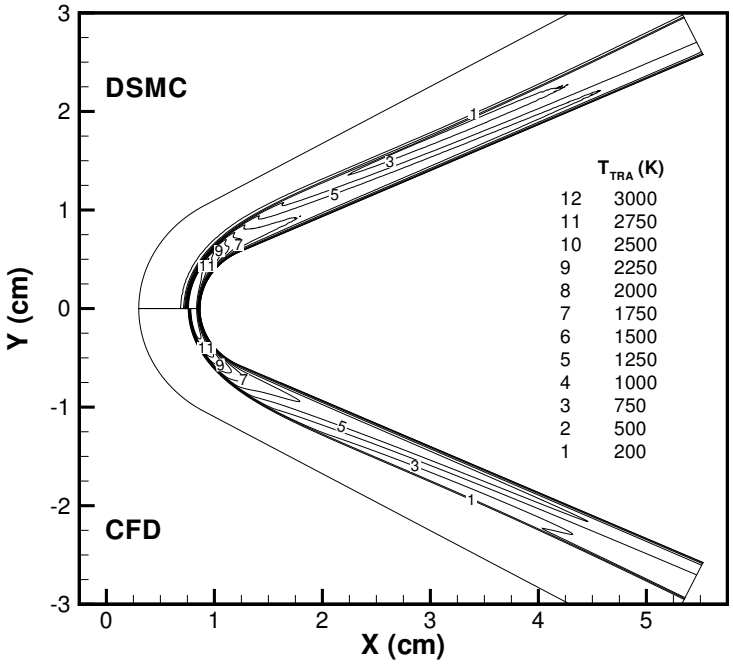

(b) Comparison of translational temperature.

Figure 3.9: Comparison of mass density and translational temperature for DSMC and CFD solutions over a 25° blunted cone.

where $C_{p_{\max}}$ is the pressure coefficient evaluated using the stagnation pressure behind a normal shock wave and θ is the angle between the freestream and the surface. In the limit as the freestream Mach number is increased to infinity, $C_{p_{\max}}$ approaches to 1.839 for a diatomic gas. Despite its simplicity, this model turns out to be capable of predicting the pressure coefficient with good qualitative accuracy.

The Fay and Riddell model [7] is employed to estimate the Stanton number at the stagnation point and gives a value of 0.185. At the same point, CFD predicts 0.190 and DSMC gives 0.188, as shown in Figure 3.10(b). The accuracy of the Fay and Riddell model is very impressive for this case.

3.1.5 DSMC and DSMC-IP Comparisons

A pure DSMC-IP simulation is performed on the same 600 by 300 grid with about 50 particles per cell on average. Based on experience, if a grid satisfies the $\Delta s/\lambda < 1$ requirement for a DSMC simulation, the grid is applicable to the corresponding DSMC-IP simulation. Also based on experience, the time step allowed in a simulation involving the DSMC-IP method must always be approximately an order of magnitude smaller than the one employed in the pure DSMC simulation. Accordingly, the time step is set to 0.3 nsec. In order to reach the steady state, therefore, about one million steps are executed and the last 60,000 steps are sampled once for every three steps.

The mass density and translational temperature contours are compared in Figure 3.11 for the DSMC and the DSMC-IP methods. Basically, the contour distributions exhibit the same flow features from both methods and the agreement between the two solutions is very good. Close-up comparisons for density and temperature near the stagnation point are given in Figures 3.12(a) and 3.12(b), respectively. It is clear that the shock thickness and position predicted with the DSMC-IP method

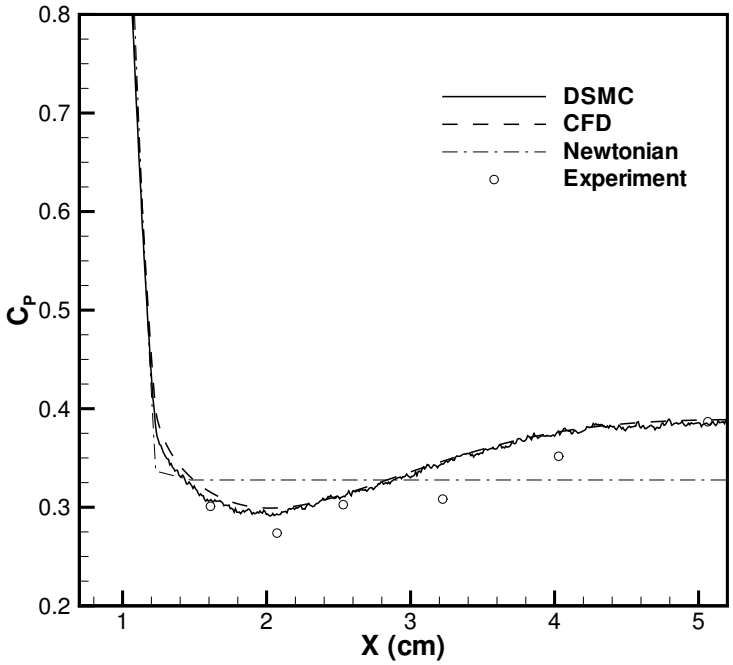

(a) Comparison of surface pressure coefficient.

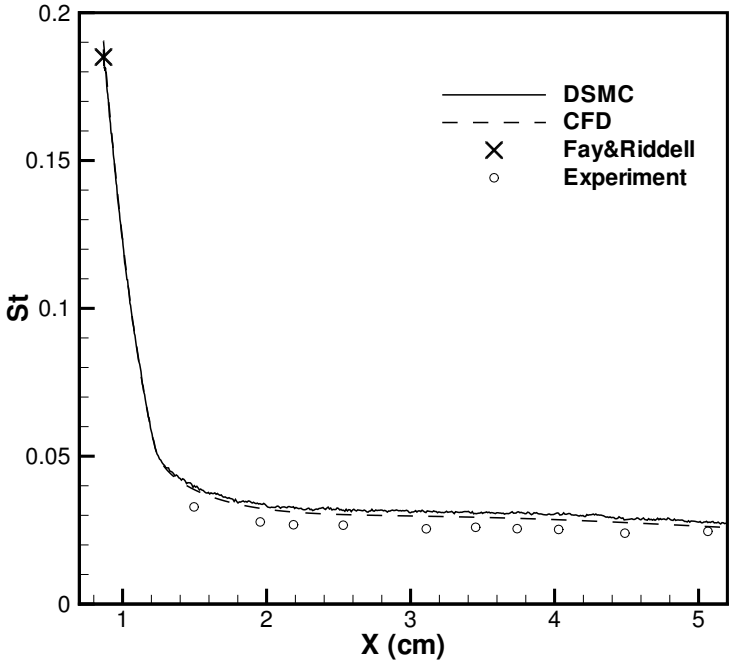

(b) Comparison of heat transfer coefficient.

Figure 3.10: Comparison of surface pressure and heat transfer coefficients for DSMC, CFD, analytic solutions, and measured data along a 25° blunted cone surface.

are different from the DSMC results to some extent.

The surface properties obtained with the DSMC-IP method are also compared with the DSMC results, as shown in Figure 3.13. Generally speaking, the pressure and heat transfer coefficients from both methods are in good agreement, except for discrepancies near the stagnation point.

3.2 Hollow Cylinder/Flare

The configuration considered in this section consists of a hollow cylinder followed by a 30° conical flare, as depicted in Figure 1.2(b). The structured grid employed for the code validation has 200,000 cells, with 1,000 cells along the body surface and 200 cells normal to the body surface, as displayed in Figure 3.14.

In all the DSMC simulations, a reference time step of 3 nsec is employed, 300,000 time steps of computation are performed, and the last 20,000 time steps are sampled to obtain the results. The total number of particles used at the end of each simulation varies with the grid resolution and other numerical parameters and will be given later. As in the blunted cone tip case, particles bouncing back from the body surface are assumed to be fully diffuse, $\alpha = 1$, unless otherwise indicated.

Detailed flow structures can be observed in Figure 3.15. A general impression of the complex flow is the gas density is reduced by a factor of about 2 from the freestream value in the region above the cylinder and then compressed more than 7 times by the shock at the flare. The temperature above the cylinder is increased due to viscous interaction and reaches a peak value of about 1,000 K. The strong compression caused by the shock leads to further heating with a peak value of approximately 1,500 K. There is a circulation region in the vicinity of the conjunction of the cylinder and flare.

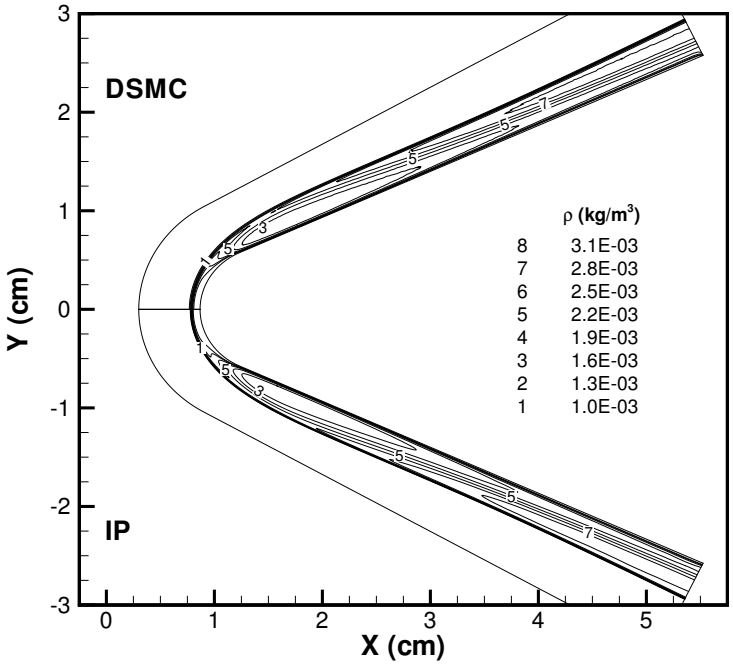

(a) Comparison of mass density.

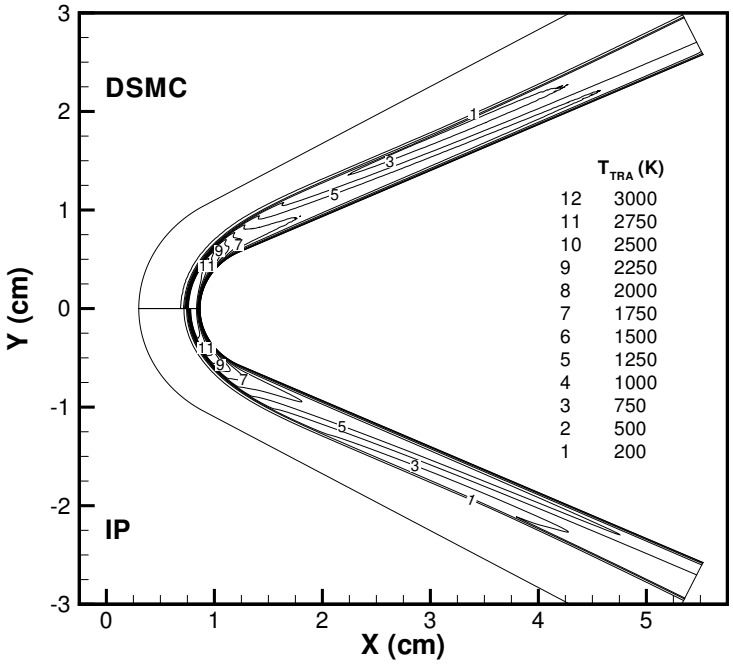

(b) Comparison of translational temperature.

Figure 3.11: Comparison for mass density and translational temperature of DSMC and DSMC-IP solutions over a 25° blunted cone.

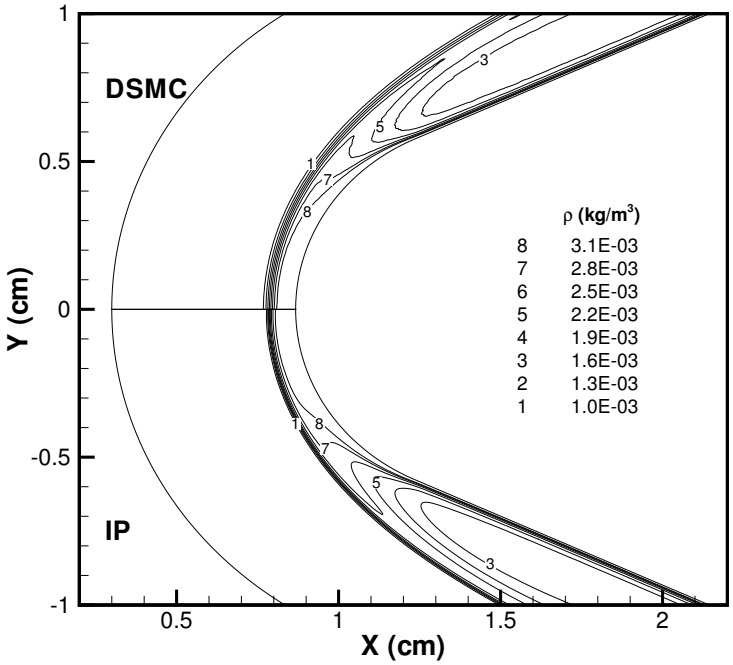

(a) Comparison of mass density.

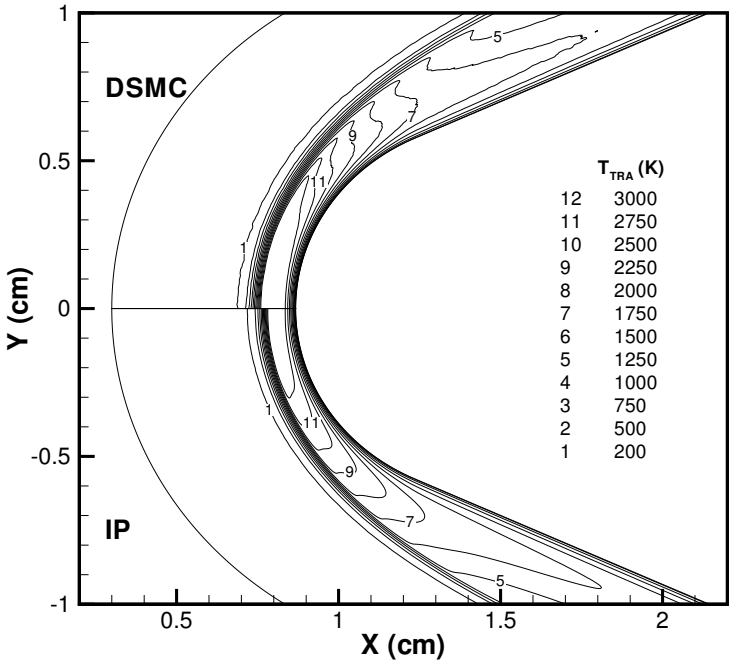

(b) Comparison of translational temperature.

Figure 3.12: Close-up comparison for mass density and translational temperature of DSMC and DSMC-IP solutions over a 25° blunted cone.

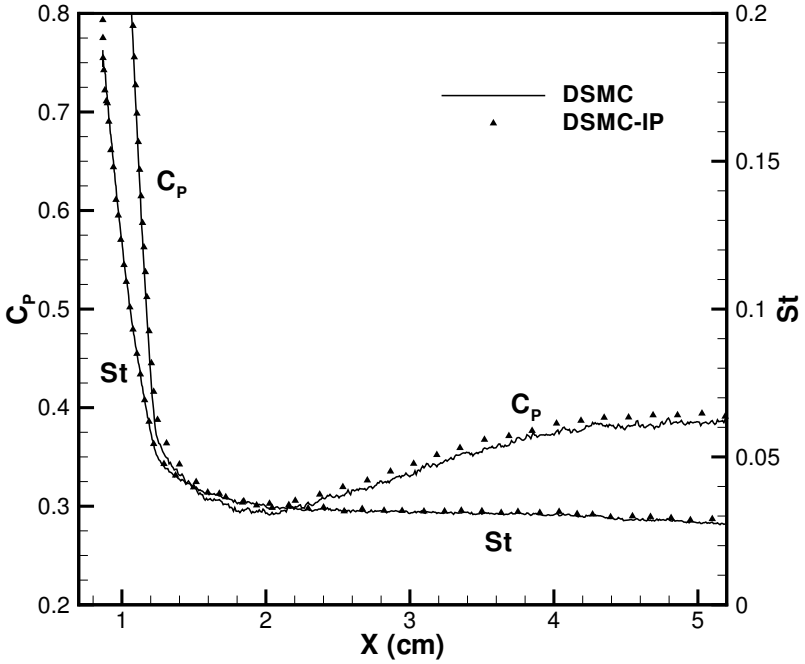

Figure 3.13: Surface pressure and heat transfer coefficients of DSMC and DSMC-IP solutions along a 25° blunted cone surface.

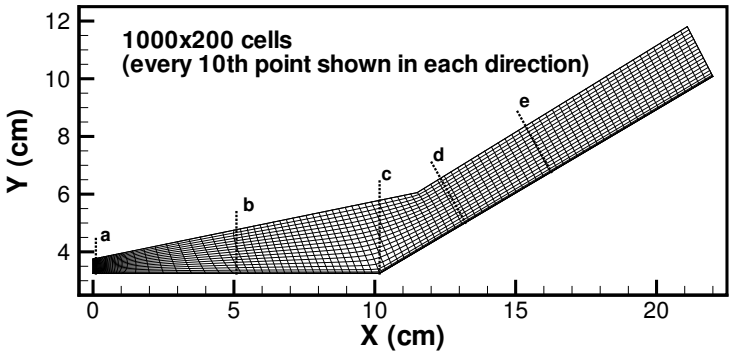

Figure 3.14: Grid employed for a hollow cylinder/flare.

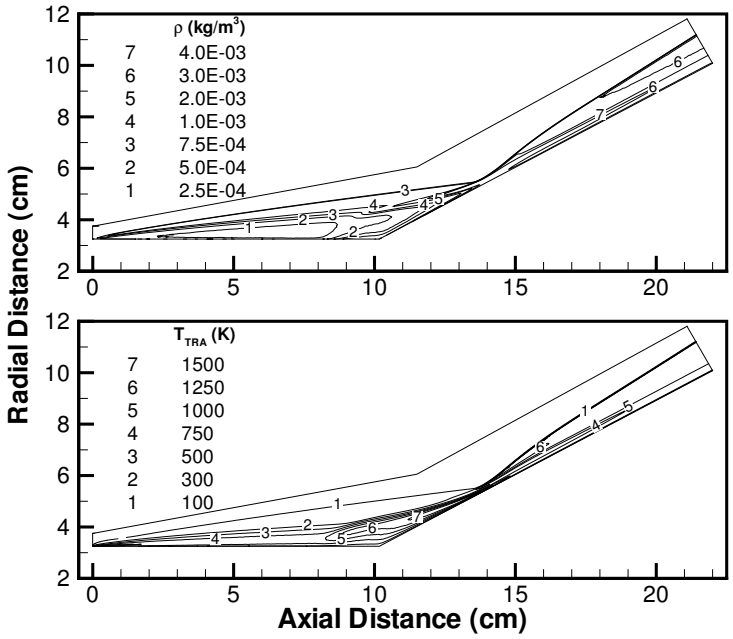

Figure 3.15: Mass density and temperature contours of the DSMC solution for the flow over a hollow cylinder/flare.

3.2.1 Numerical Parameters

The first step to validate the DSMC solution is to again examine the numerical parameters employed, including the simulation time-step, cell size, and number of particles per cell. Data have been extracted along five lines normal to the hollow cylinder/flare body at $x/L = 0.01, 0.5, 1.0, 1.3$, and 1.6 (corresponding to the dotted lines $a, \ldots, e$ in Figure 3.14).

In Figure 3.16, the ratio of the simulation time-step to the local mean collision time along each line is plotted as a function of the normal-distance from the body, δn. It is obvious that the criterion $\Delta t/\tau < 1$ is met everywhere.

To examine the cell size criterion, the ratio of the characteristic cell size to the local mean free path along each line is displayed in Figure 3.17 also as a function of δn. The characteristic cell size is again defined as the length scale of a cell in the direction of the maximum gradient of density, pressure, temperature, or velocity. It

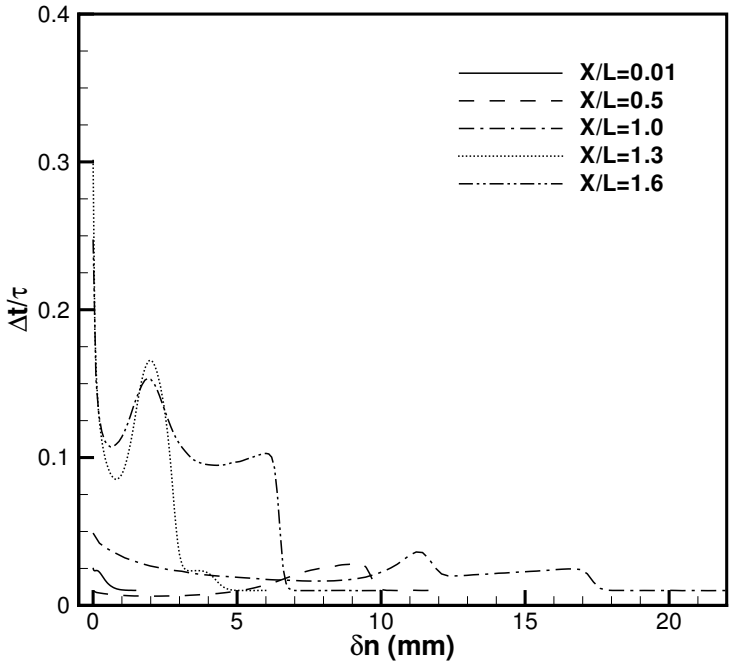

Figure 3.16: Ratio of simulation time-step to local mean collision time along five different lines normal to a hollow cylinder/flare body.

is evident from this figure that the current grid resolution is too coarse for the flow, particularly in the flare region where a strong shock is formed. Along the line at $x/L = 1.3$, for example, the grid size should be decreased by a factor of 11 in some places. However, due to limited computing resources, it is very expensive to employ such a fine grid. An alternative is to increase the number of simulated particles and utilize the sub-cell scheme in the DSMC code. Therefore, about 27 million particles are employed in this simulation to ensure that there is a sufficient number of particles in each sub-cell. Taking the line at $x/L = 1.3$ for example, when $\Delta s/\lambda$ reaches its maximum of about 11, there are about 600 particles per cell as shown in Figure 3.18. It is reasonable to believe that there are enough particles in each sub-cell and, as a result, the DSMC solution based on the current numerical parameters is correct. The total run time of the DSMC simulation on a Linux cluster with 40 2.4-GHz Intel® Xeon™ processors is about 280 hours.

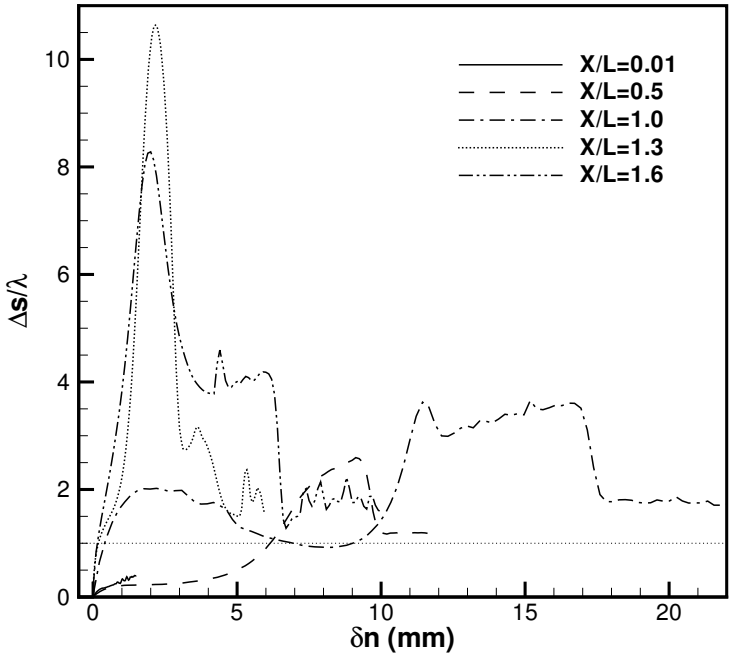

Figure 3.17: Ratio of simulation cell size in direction of maximum gradient to local mean free path along five different lines normal to a hollow cylinder/flare body.

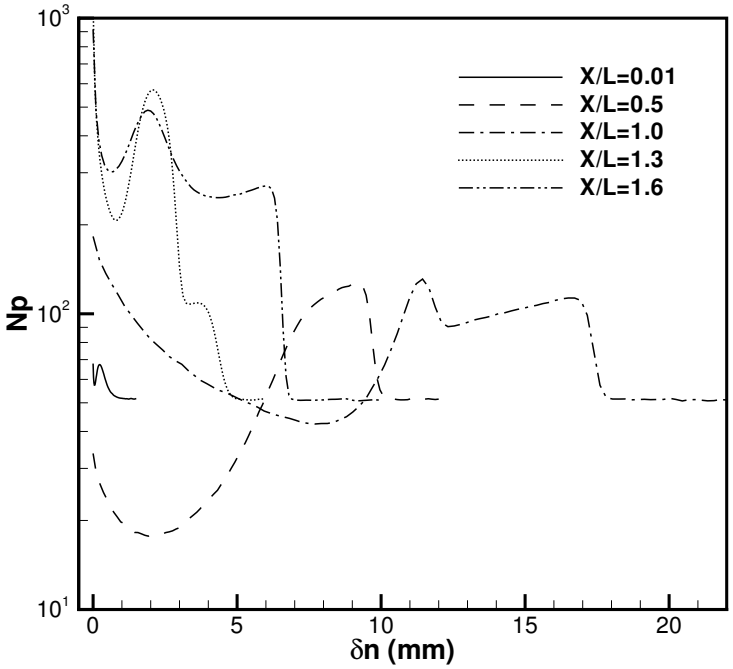

Figure 3.18: Number of particles per cell along five different lines normal to a hollow cylinder/flare body.

It is indicated in Figures 3.16 and 3.17 that the criteria for Δt and Δs are both satisfied near the body surface. This leads to good accuracy of the DSMC solution in this region.

3.2.2 Grid Sensitivity

A finer grid, consisting of 2,000 cells along the body surface and 400 cells normal to the body, is used to test the sensitivity of the steady state solution to the grid resolution. On this finer grid, there are more than 29 million particles employed at the end of the simulation. Comparisons of the surface pressure coefficient and heat transfer coefficients obtained with the finer and the coarse 1,000 by 200 grids are made in Figure 3.19. When the finer grid is employed, the shock position is slightly shifted downstream and the size of the circulation region is a little larger, as seen in Figure 3.19(c) for the calculated skin friction coefficient. Other than these small differences, the two solutions are very close. Since this is an extremely time-consuming flow to simulate, only the coarse 1000 by 200 grid is considered from now on.

3.2.3 Accommodation Coefficient

Also shown in Figure 3.19 are the surface pressure coefficient and Stanton number computed with the accommodation coefficient α equal to 0.85. Generally speaking, the solutions for $\alpha = 0.85$ and 1 are very similar. Minor discrepancies can be found about the shock position and the size of the circulation region. Interestingly, the heating rate on the flare behind the shock is slightly higher for the condition of $\alpha = 0.85$. Overall, it is concluded that the DSMC results are not very sensitive to the accommodation coefficient in the range from 0.85 to 1.

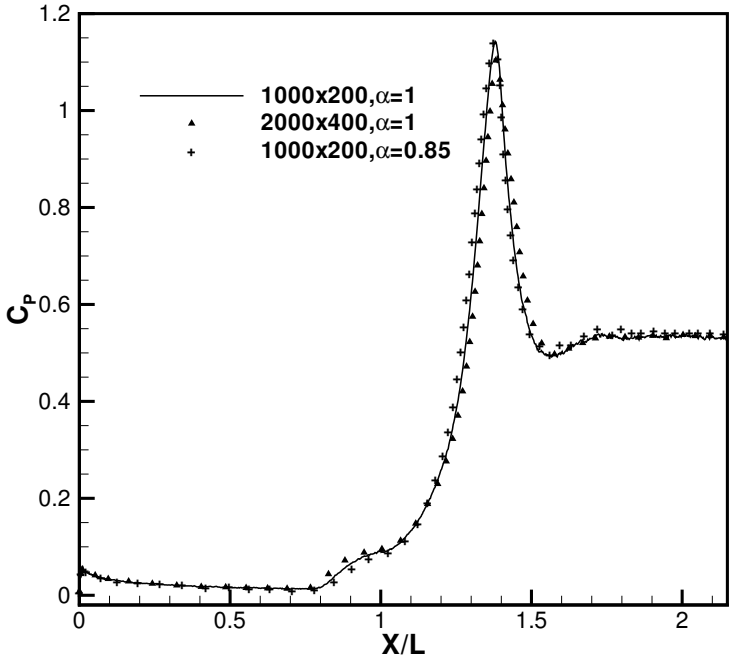

(a) Comparison of surface pressure coefficient.

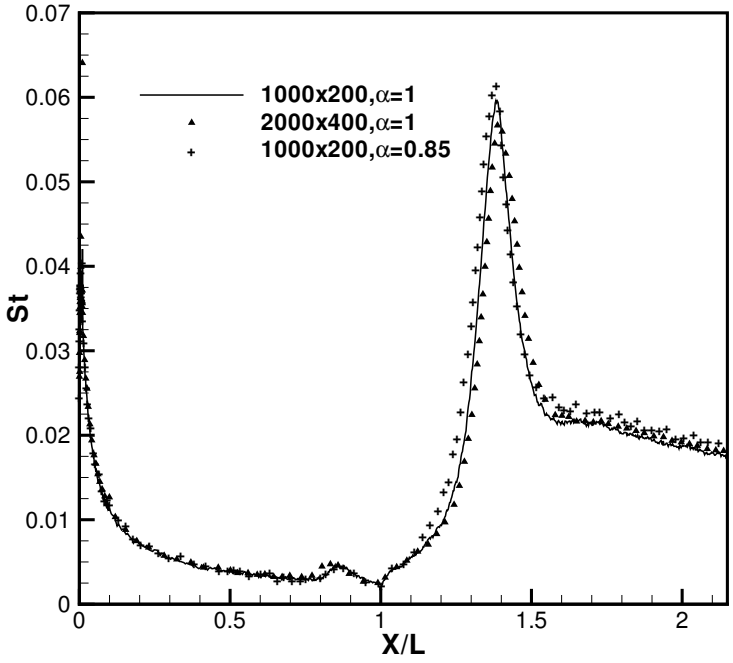

(b) Comparison of heat transfer coefficient.

Figure 3.19: Surface pressure, heat transfer, and skin friction coefficients at different levels of gird resolution and different accommodation coefficients along a hollow cylinder/flare surface.

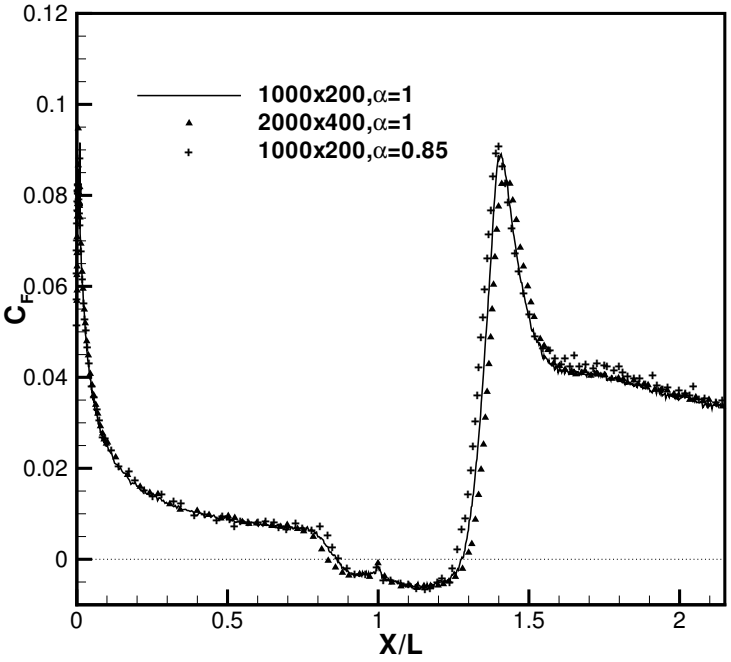

(c) Comparison of skin friction coefficient.

Figure 3.19: Surface pressure, heat transfer, and skin friction coefficients at different levels of gird resolution and different accommodation coefficients along a hollow cylinder/flare surface. (continued)

3.2.4 DSMC and CFD Comparisons

A pure CFD simulation [62] is also performed on the same 2.4-GHz Linux cluster on a much finer grid with 2048 cells along the surface and 512 cells normal to the surface. The simulation takes about 8 hours for the CFD method to converge to the steady state solution.

Comparisons of the mass density and translational temperature obtained with the DSMC and CFD methods are made in Figure 3.20. Although the two solutions look similar, differences between them can be observed. A major difference is the size of the circulation region near the conjunction of the cylinder and flare. It is clear that CFD predicts a much larger circulation region. This can be verified in Figure 3.21 in which the skin friction coefficients from the two numerical methods are shown.

In Figure 3.22, the pressure and heat transfer coefficients obtained with the DSMC and CFD methods are compared with the measured data [50] along the hollow cylinder/flare body surface. It is again shown in the figures that the circulation region is significantly larger in the CFD solution, causing the shock position in the CFD solution to be a little further downstream than the shock position predicted with DSMC. When the numerical results are compared with the measured data, it is evident that DSMC provides a more accurate solution in terms of the size of the circulation region. A flow of this kind is a great challenge for a hybrid particle-continuum method because a good hybrid method must successfully reduce the size of the circulation region from that predicted by CFD to that predicted by DSMC.

The surface pressure coefficient calculated with the modified Newtonian model is also displayed in Figure 3.22(a). This model predicts the surface pressure as a step function as can be easily verified from Equation (3.1). Because some important

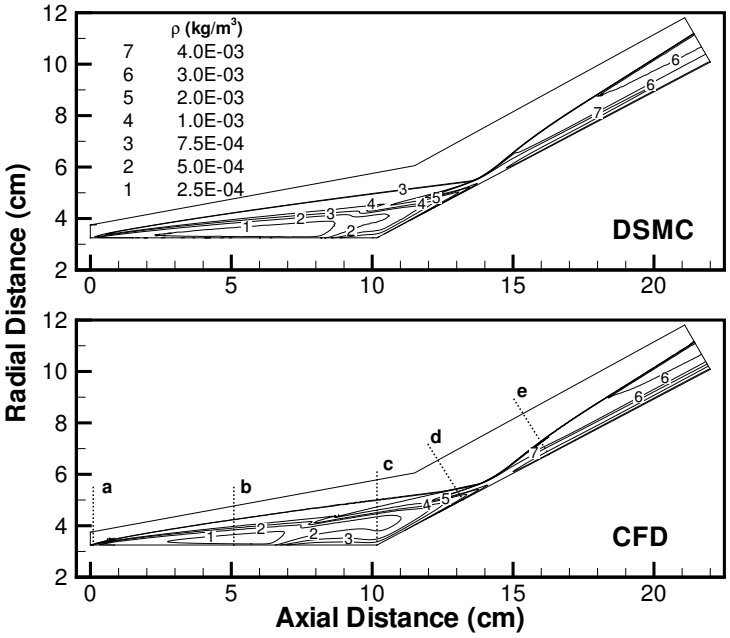

(a) Comparison of mass density.

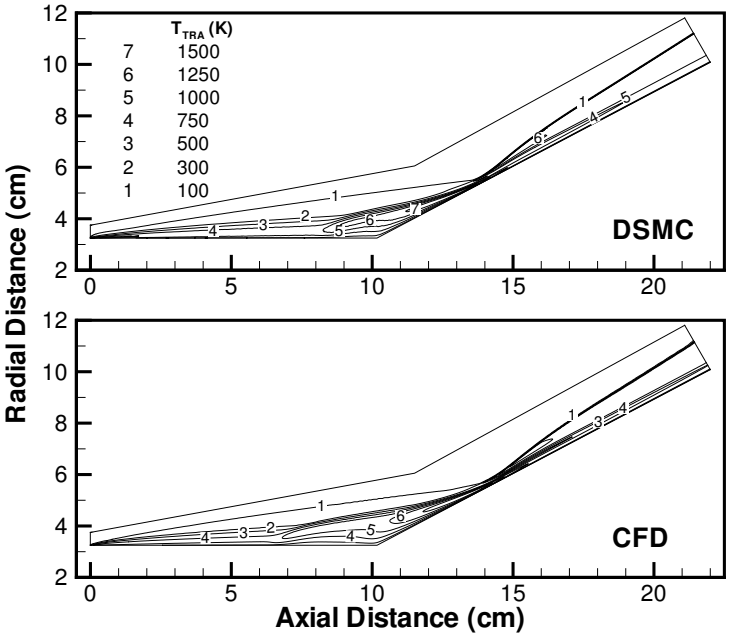

(b) Comparison of translational temperature.

Figure 3.20: Comparison of mass density and translational temperature of DSMC and CFD solutions over a hollow cylinder/flare.

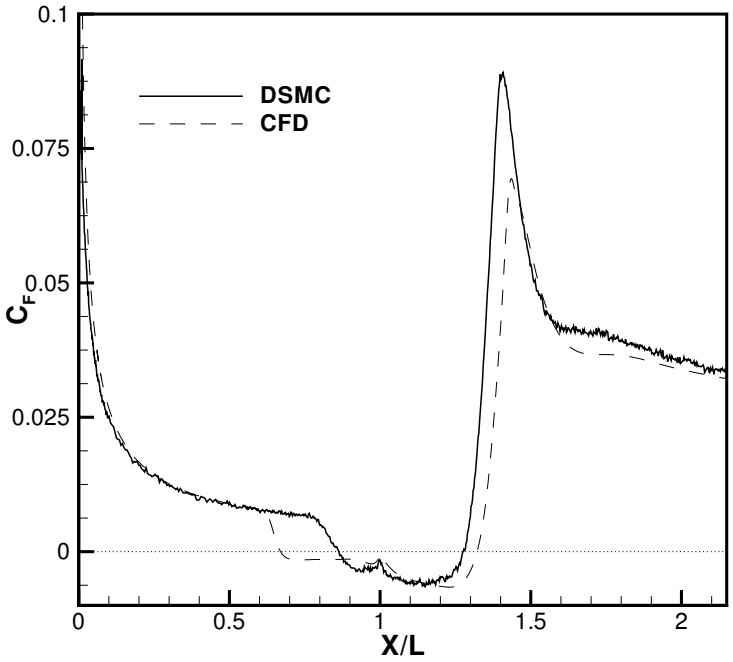

Figure 3.21: Comparison of skin friction coefficient for DSMC and NS solutions along a hollow cylinder/flare surface.

flow features, such as shock wave and boundary layer, are not taken into account in this simple model, it is not surprised that it does not predict this complex flow accurately.

3.2.5 DSMC and DSMC-IP Comparisons

It would be very interesting to apply the DSMC-IP method to the more complex hollow cylinder/flare flow. However, as stated in Section 3.1.5, the time-step allowed in a DSMC-IP simulation is always an order of magnitude smaller than the one in the pure DSMC simulation. Therefore, due to the computing resources available, such a validation is not provided in the thesis.

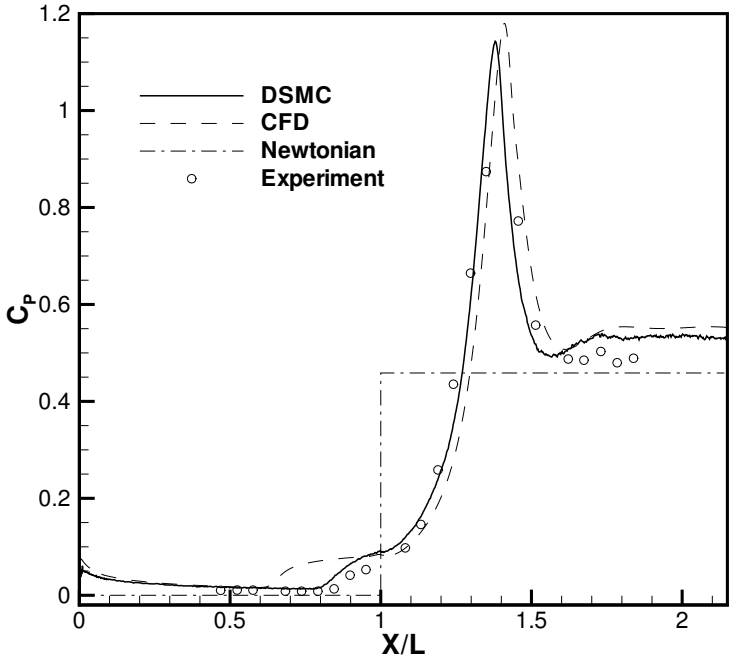

(a) Comparison of surface pressure coefficient.

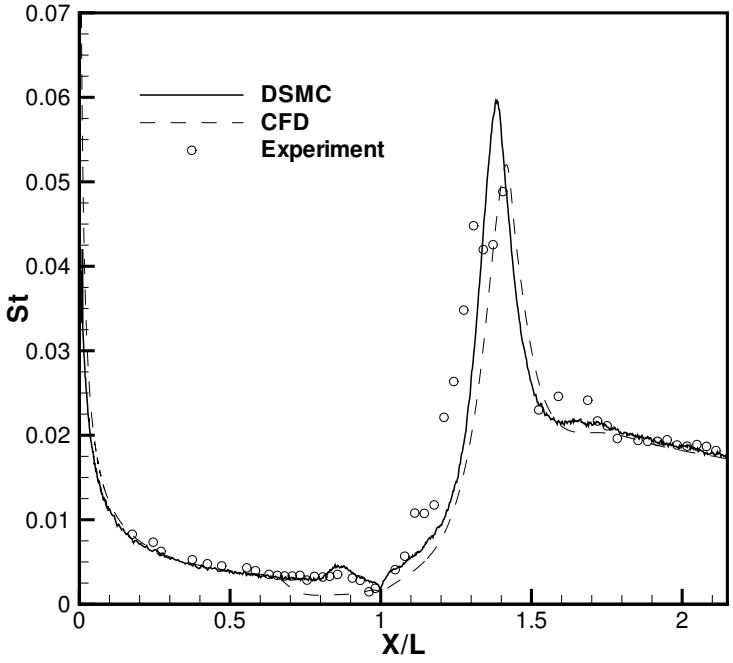

(b) Comparison of heat transfer coefficient.

Figure 3.22: Comparison of surface pressure and heat transfer coefficients for DSMC, NS and analytic solutions, and measured data along a hollow cylinder/flare surface.

CHAPTER IV

CONTINUUM BREAKDOWN

As already discussed in Chapter I, there are two primary issues associated with the combination of two numerical methods. The first issue regarding the strategy of switching between the methods is addressed in this chapter. Because the Navier-Stokes equations are not valid under rarefied conditions, it is general to use a continuum breakdown parameter as the criterion for switching. Investigation will be focused on predicting the conditions under which the continuum approach may be expected to fail in hypersonic viscous flows. A breakdown criterion is developed by detailed comparisons of CFD and DSMC solutions.

4.1 Continuum Breakdown Parameters

In prior works of continuum breakdown, Bird [13] proposed a semi-empirical parameter for steady state expanding flows

$$P = \frac{U}{\rho\nu}\left|\frac{d\rho}{ds}\right| = M\sqrt{\frac{\pi\gamma}{8}}\frac{\lambda}{\rho}\left|\frac{d\rho}{ds}\right|,$$

where U is the local velocity, ν is the collision frequency, M is the local Mach number, γ is the ratio of specific heats, and s is the distance along a streamline. Although studies by Bird [13] indicate the value for P of about 0.05 is a good criterion for continuum breakdown in steady expanding flows, it is believed that in complicated

flows density is not the only flow property needed to be taken into account. By the same definition, any flow property Q (e.g. density, temperature, etc) can be employed to obtain

$$P_Q = M\sqrt{\frac{\pi\gamma}{8}}\frac{\lambda}{Q}\left|\frac{dQ}{ds}\right|. \tag{4.1}$$

It is a problem because M approaches to zero at stagnation points. Boyd *et al.* [22] carried out an extensive numerical investigation of one-dimensional normal shock waves and two-dimensional bow shocks comparing DSMC and CFD results, to determine an appropriate breakdown parameter. They concluded that the gradient-length local (GLL) Knudsen number

$$\mathrm{Kn}_{\mathrm{GLL}} = \frac{\lambda}{Q}\left|\frac{dQ}{dl}\right|,$$

where l is some distance between two points in the flow field, provides a better indication of continuum breakdown than P for hypersonic compressed flows. They also showed that the distance l should be taken approximately along the line of the steepest gradients in the flow properties. In this chapter, however, dQ/dl is evaluated as ∇Q without projecting it onto a preferential direction. For simplicity, the subscript GLL is removed from now on and the GLL Knudsen number for property Q is expressed as

$$\mathrm{Kn}_Q = \frac{\lambda}{Q}\left|\nabla Q\right|. \tag{4.2}$$

The Knudsen number of this form has a great physical meaning. When its value is much less than unity the flow can be regarded as locally slightly perturbed from equilibrium [40] that is a fundamental assumption of the NS equations. Therefore, it is an appropriate parameter to predict continuum breakdown.

It is apparent that Equations (4.1) and (4.2) are not independent and have the

relation

$$\frac{P_Q}{\mathrm{Kn}_Q} = M\sqrt{\frac{\pi\gamma}{8}}\cos\theta \tag{4.3}$$

where θ is the angle between gradient ∇Q and the flow direction. Since $\sqrt{\pi\gamma/8} < 1$ for all gases, the value of P_Q is always less than Kn_Q in subsonic regions. In the region immediately adjacent to the wall surface, because both M and $\cos\theta$ decrease towards zero, P_Q is always several orders of magnitude smaller than Kn_Q. The differences between P_Q and Kn_Q will be demonstrated numerically in the next section.

Because the breakdown of the NS equations is related to viscosity and heat transfer, both transport phenomena have to be taken into account. As a result, density(D), the magnitude of velocity(V) and translational temperature(T) are the flow properties usually considered in the breakdown parameters. A new parameter is defined for P and Kn, respectively,

$$P_{\max} \equiv \max\left(P_D, P_T, P_V\right) \tag{4.4}$$

$$\mathrm{Kn}_{\max} \equiv \max\left(\mathrm{Kn}_D, \mathrm{Kn}_T, \mathrm{Kn}_V\right) \tag{4.5}$$

to be utilized as the actual breakdown parameter for switching between the numerical methods.

4.2 Numerical Studies

The numerical examples considered in this chapter again refer to the experiments performed in CUBRC impulse test facilities by Holden [49]. The fluid is pure nitrogen and the freestream conditions are listed in Table 4.1. The wall temperature, T_{wall}, of both examples is assumed constant in the computations.

	Sharp Cone Tip	Hollow Cylinder/Flare
M_∞	11.3	11.3
Re_L (10^4)	1.45	1.38
T_∞ (K)	138.9	128.9
T_{wall} (K)	296.1	297.2
V_∞ (m/s)	2712.2	2609.1
ρ_∞ (10^{-4}kg/m^3)	5.515	5.066

Table 4.1: Freestream conditions for the flows considered for continuum breakdown.

4.2.1 Sharp Cone Tip

The first configuration studied in this chapter covers the first 5 cm of the forecone in Figure 1.2(a). The DSMC computation employs a structured grid with 1200 cells along the cone surface by 400 cells normal to the cone. A reference time step of 0.5 nsec is used. More than 8 million simulation particles are employed at the end of the computation that consumes a total of 82 hours on 16 processors on an IBM-SP machine. The results presented below are obtained by sampling over 50,000 time steps. The CFD simulation [61] is performed on a structured grid with 288 cells along the body and 512 cells normal to the body.

Comparisons of the density and translational temperature contours obtained with CFD and DSMC are made in Figures 4.1(a) and 4.1(b), respectively. Good agreement is shown in general between the two solutions.

A detailed comparison of the flow properties obtained with the NS and DSMC approaches is made in Figure 4.2(a) at $x/L = 0.92$ cm [dotted line b in Figure 4.1(a)], where x is the axial distance from the leading edge of the cone tip. In this figure, δn

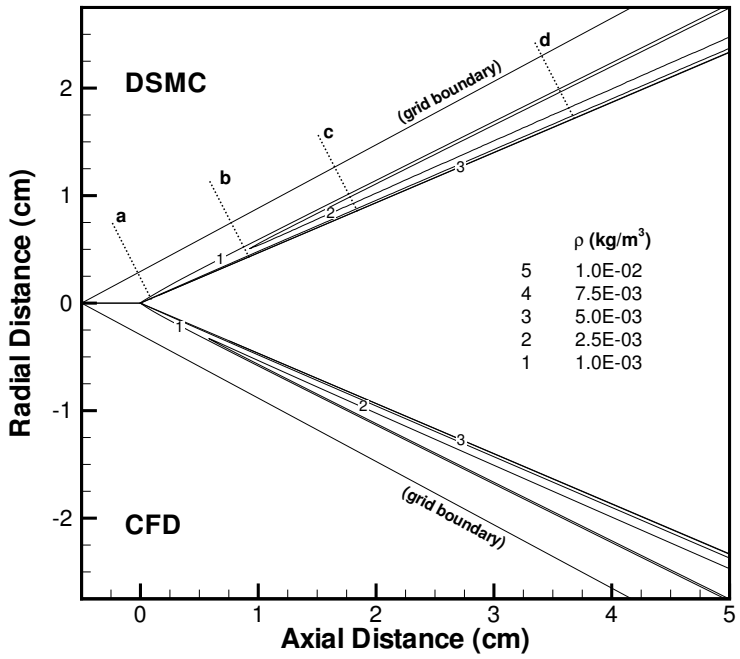

(a) Comparison of density.

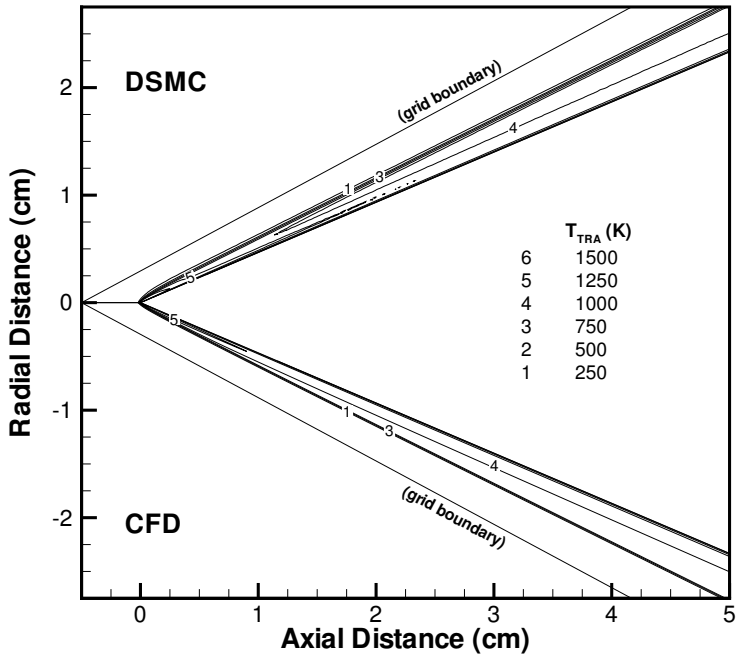

(b) Comparison of translational temperature.

Figure 4.1: Comparison of DSMC and CFD solutions of mass density and translational temperature for hypersonic flow over a 25° sharp cone.

is the distance from the cone surface and ϵ_Q is defined as

$$\epsilon_Q \equiv \frac{Q_{\text{CFD}}}{Q_{\text{DSMC}}} - 1 \tag{4.6}$$

and represents the degree of difference between the NS and DSMC solutions. Throughout this chapter, for the purposes of discussion, failure of the continuum approach is defined to occur whenever $|\epsilon_Q| > 0.05$. It is shown in this figure that the DSMC shock is much thicker than the CFD shock, suggesting strong nonequilibrium effects. The thicker DSMC shock results in negative values of ϵ for density and temperature ahead of the shock predicted by CFD. Near the cone surface, the substantially large values of ϵ are assumed to indicate the failure of the NS approach. In particular, the NS density close to the surface is about 70% higher than the DSMC solution. In contrast, the NS velocity and temperature are, respectively, 40% and 90% lower than the DSMC solutions, indicating a prediction of less slip by the model employed in CFD. In between the shock and near-body regions, the solutions of the CFD and DSMC techniques agree approximately.

Profiles of P and Kn based on the NS solutions are shown in Figure 4.2(b). A 0.05 line is also shown in the figure to indicate the breakdown of the NS approach. All breakdown parameters vanish in the free-stream and increase rapidly across the shock wave. As discussed above, the continuum approach fails in the region immediately adjacent to the wall surface. It is clear that the Kn parameters capture the breakdown very well in this region. In other words, the hybrid code will successfully detect the continuum breakdown and prepare to switch to the DSMC method. By comparison, the P parameters are not able to predict breakdown close to the wall since these values become very small. This is attributed to the small value of the Mach number and approximate right angle between the flow and gradient directions.

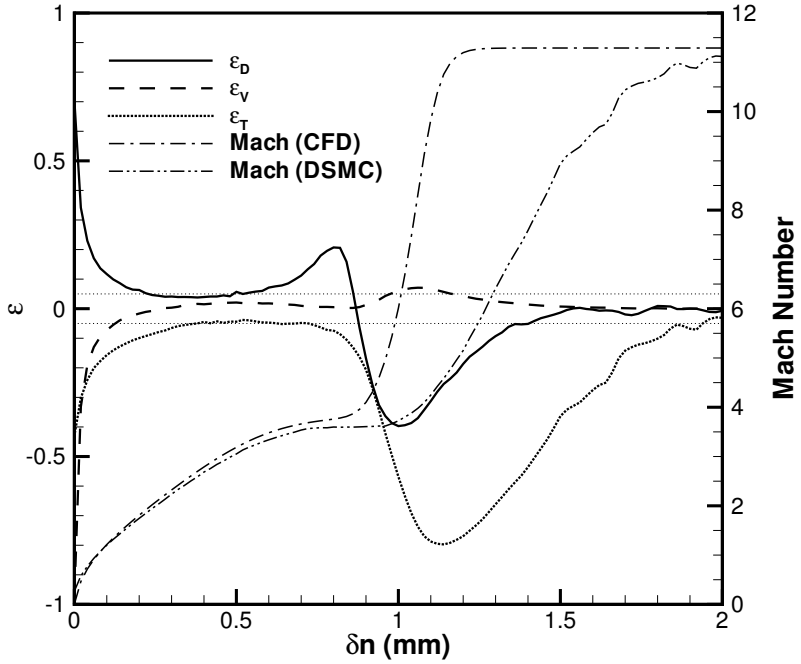

(a) Comparison of density, velocity, temperature and Mach number.

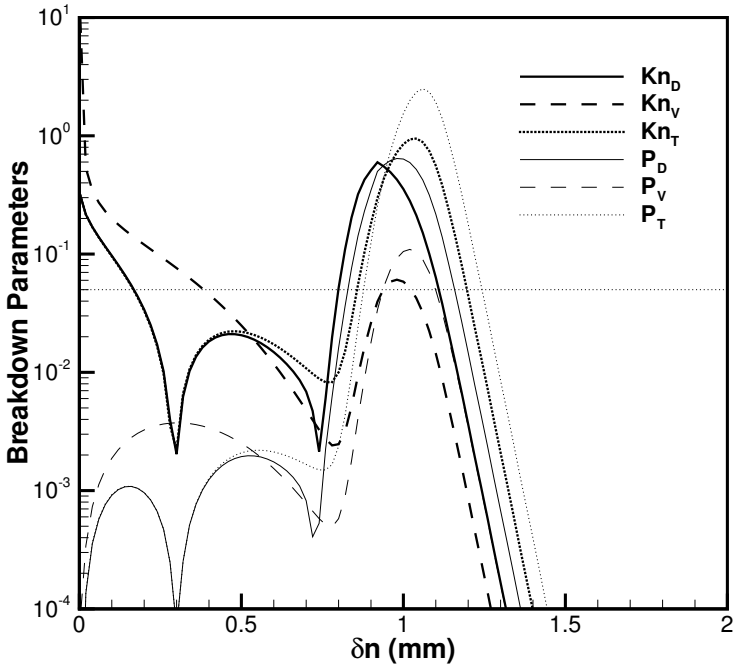

(b) Breakdown parameters based on NS solutions.

Figure 4.2: Profiles along the line normal to the 25° cone surface at $x = 0.92$ cm. (continued)

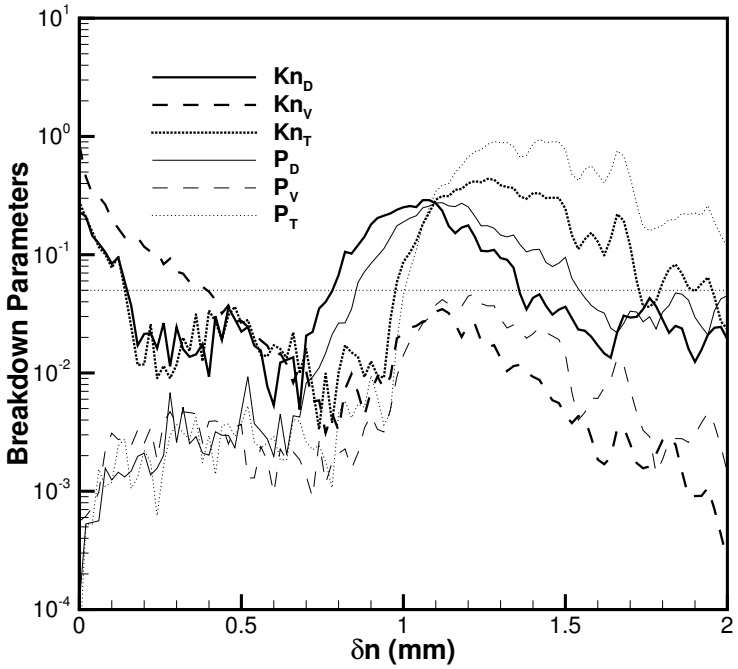

(c) Breakdown parameters based on DSMC solutions.

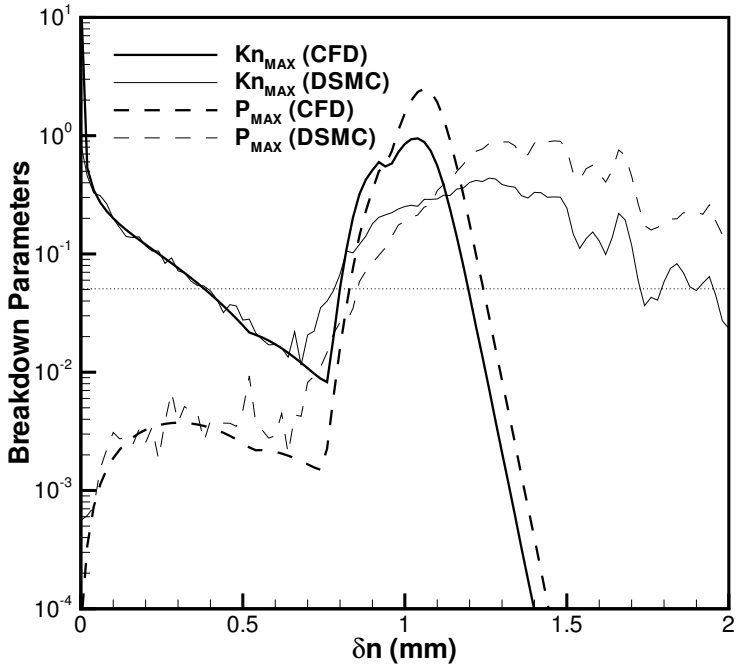

(d) Variation of $\mathrm{Kn}_{\max}$ and $P_{\max}$ based on NS and DSMC solutions.

Figure 4.2: Profiles along the line normal to the 25° sharp cone surface at $x = 0.92$ cm.

Similarly, profiles of P and Kn based on the DSMC solutions are illustrated in Figure 4.2(c). The profiles qualitatively agree with the profiles in Figure 4.2(b) in the region close to the body surface. The peak of each DSMC parameter across the shock is lower than the corresponding value of the CFD results in Figure 4.2(b) because of weaker gradients over the thicker shock in the DSMC solutions.

In Figures 4.2(b) and 4.2(c), it is easy to observe that Kn_D and Kn_T are almost identical near the wall. A proof of this observation is given in Appendix B.

It is shown in Figure 4.2(a) over $0 < \delta n < 0.38$, that $|\epsilon_T| > 0.05$ and in Figures 4.2(b) and 4.2(c) Kn_V is the only parameter that can predict the continuum breakdown in this region. However, Kn_V does not accurately predict the continuum breakdown at the shock. At about $\delta n = 1.15$, ϵ_T is approximately -0.8. At the same location, Kn_V is about 0.006 and 0.03 for the CFD and DSMC solutions, respectively, both below the cut-off value of 0.05. In comparison, Kn_T reaches about 0.2 for both solutions. Therefore, it is necessary to evaluate Kn based on various flow properties at each location in order to predict the continuum breakdown accurately.

In Figure 4.2(d) profiles of $P_{\max}$ and $\mathrm{Kn}_{\max}$ defined in Equations (4.4) and (4.5) are displayed. It is clear that near the body surface, $\mathrm{Kn}_{\max}$ evaluated with the CFD and DSMC results are very close to each other and predict continuum breakdown whereas the values of $P_{\max}$ are much lower than 0.05. In comparison of Figures 4.2(a) and 4.2(d), it is found that the use of $\mathrm{Kn}_{\max}$ for predicting the failure of the continuum approach is quite successful. In the region of δn from 0 to about 0.38, Figure 4.2(d) has values of $\mathrm{Kn}_{\max}$ higher than 0.05 and Figure 4.2(a) shows the corresponding continuum breakdown. From $\delta n \sim 0.38$ to $\delta n \sim 0.8$, $\mathrm{Kn}_{\max}$ evaluated with the CFD solution is below the breakdown criterion and flow properties from the two methods agree except for a small fraction of the post-shock region. For the rest of

the region from $\delta n \sim 0.8$ to the free-stream boundary, $\mathrm{Kn}_{\max}$ calculated with the DSMC solution is higher than the criterion in general and continuum breakdown is observed in Figure 4.2(a).

In Figure 4.3(a), the NS and DSMC solutions are compared in detail along a line normal to the cone at $x = 1.84$ cm [dotted line c in Figure 4.1(a)]. It is evident that the differences of the two solutions at this station are similar to those in Figure 4.2(a). The $\mathrm{Kn}_{\max}$ and $P_{\max}$ values based on the CFD and DSMC solutions are illustrated in Figure 4.3(b). The continuum breakdown near the wall of the cone is predicted by $\mathrm{Kn}_{\max}$ but not by $P_{\max}$. The same CFD/DSMC switch discussed above can be observed. Similarly, the profiles of comparison and breakdown parameters are displayed in Figure 4.4 along the line normal to the cone at $x = 3.68$ cm [dotted line d in Figure 4.1(a)].

Although $\mathrm{Kn}_{\max}$ in Figures 4.2 through 4.4 has not demonstrated the capability of prediction of the failure of the continuum approach in some regions, especially in the post-shock region, this is not a serious concern at this point. Keep in mind the comparisons are made of the steady state solutions obtained with two different numerical techniques. The flow details, such as the shock angle and thickness, are not identical in the two solutions. As a result, significant differences in the post-shock region were expected. The answer to whether Kn can completely predict all occurrences of breakdown will not be revealed until it is actually employed in the hybrid code.

Strong thermal nonequilibrium near the leading edge of the cone has been reported by Wang and Boyd [87]. The profiles of the comparisons between the NS and DSMC solutions for the flow properties near the leading edge at $x = 0.92$ mm [dotted line a in Figure 4.1(a)] are shown in Figure 4.5(a). Clearly, the shock angle and

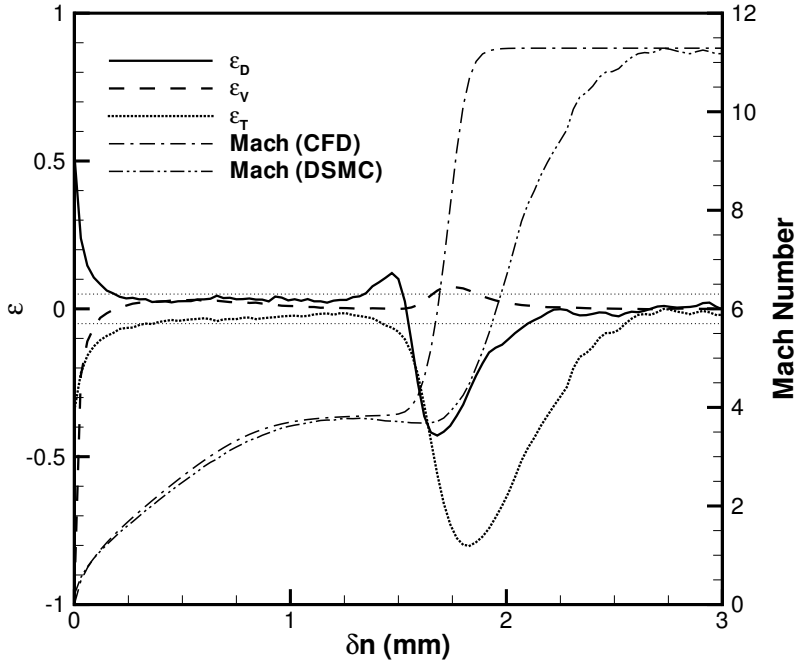

(a) Comparison of density, velocity, temperature and Mach number.

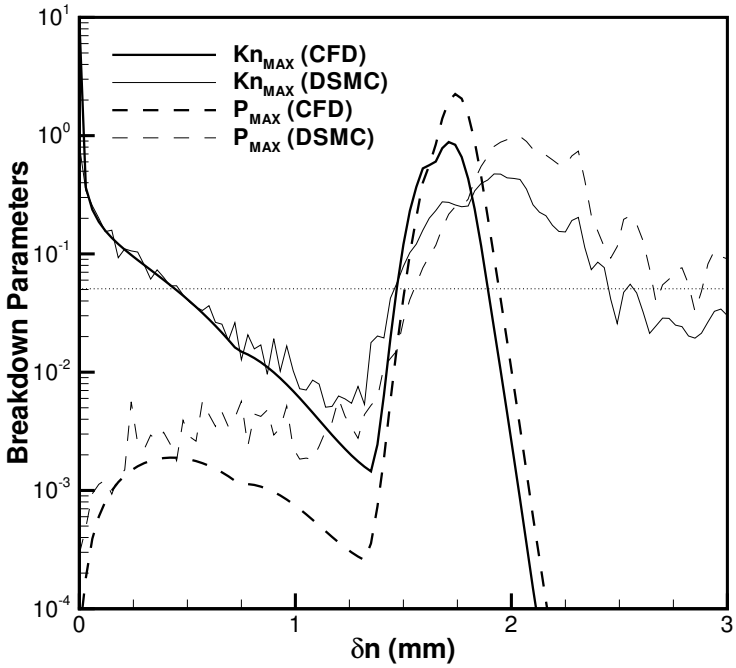

(b) Variation of Kn and P based on NS and DSMC solutions.

Figure 4.3: Profiles along the line normal to the 25° sharp cone surface at x = 1.84 cm.

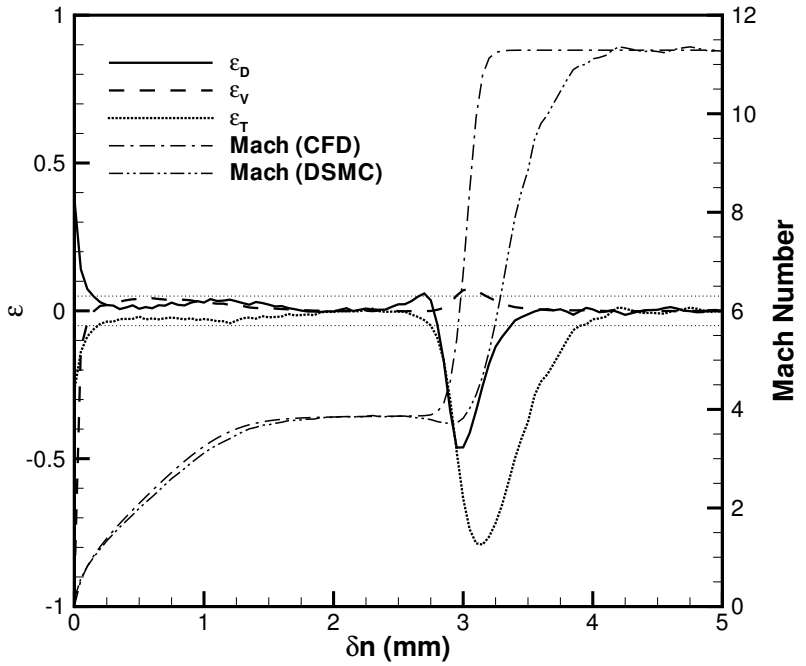

(a) Comparison of density, velocity, temperature and Mach number.

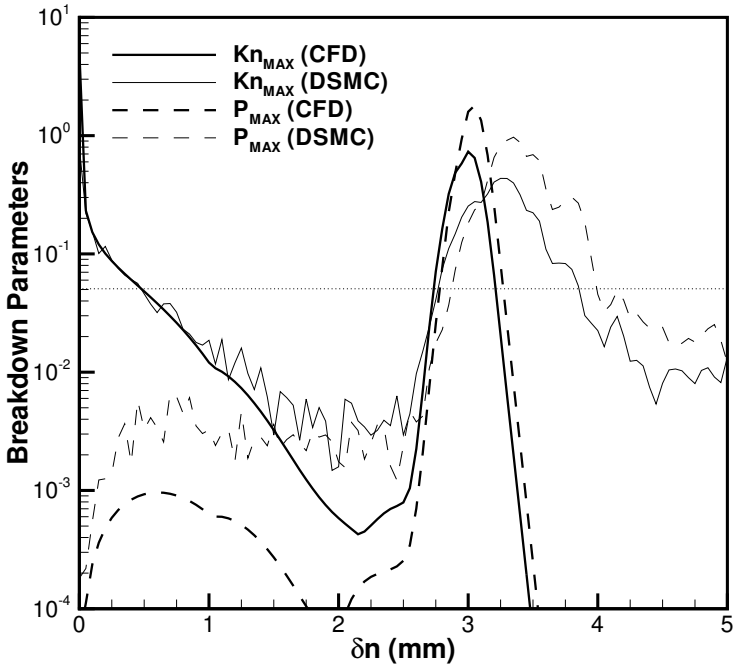

(b) Variation of Kn and P based on NS and DSMC solutions.

Figure 4.4: Profiles along the line normal to the 25° sharp cone surface at x = 3.68 cm.

thickness calculated with the CFD technique do not agree with the DSMC results. The rarefaction parameter [60], $\overline{V}$, is evaluated locally as about 0.74. This value is about 5 times higher than the upper limit, $\overline{V} \approx 0.15$, for the Rankine-Hugoniot shock structure theory to be valid. The accuracy of the NS approach at this station must be consequently poor. Note the mix of the post-shock region with the boundary layer, which indicates interactions between the two regions. $\mathrm{Kn}_{\max}$ based on the DSMC solutions is higher than the criterion over the entire region considered [see Figure 4.5(b)]. This suggests the use of the DSMC approach near the leading edge is necessary.

It is interesting to point out that the failure of the NS equations near the leading edge should have a connection with the continuum breakdown in the rest of the flow field. One can image that the continuum breakdown from the shock and near-body in the region close to the leading edge is mixed together and separates gradually in the downstream. One branch follows the path of the shock, which departs from the cone surface. The other branch stays in the region immediately adjacent to the wall. By the same token, some of the differences between NS and DSMC for large x are due to differences that first occur at the leading edge and then propagate.

The results shown in Figures 4.2 through 4.5 for the hypersonic flow over a sharp 25° half-angle cone tip may be summarized as follows. Near the body surface, the steep flow gradients cause the continuum equations to fail and to predict the flow properties incorrectly. This has a great impact for the continuum estimation of surface values such as heat transfer rate and pressure. Accordingly, the DSMC technique must be employed in this region. Moving away from the body, there is a region where the solutions of the NS and DSMC approaches agree approximately. The NS method should be used in this region. Moving further away from the body

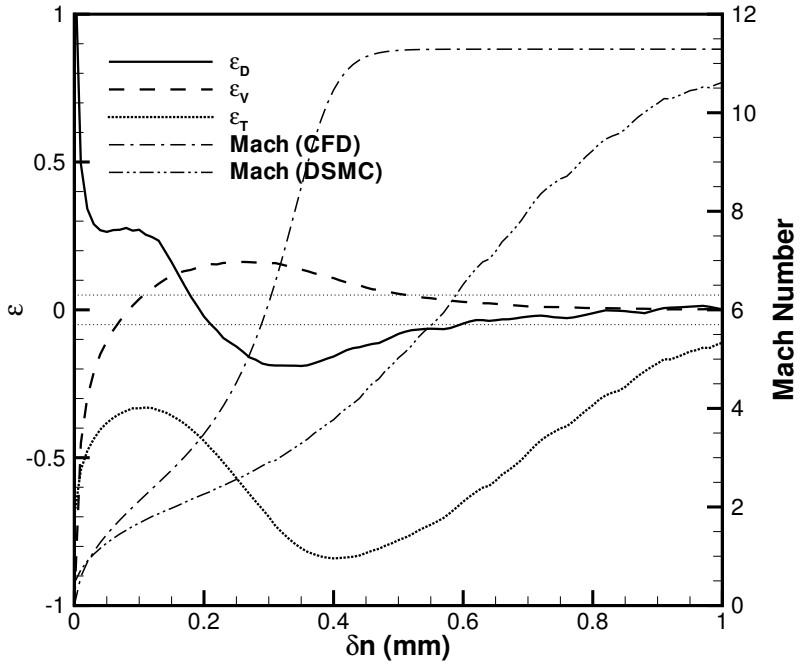

(a) Comparison of density, velocity, temperature and Mach number.

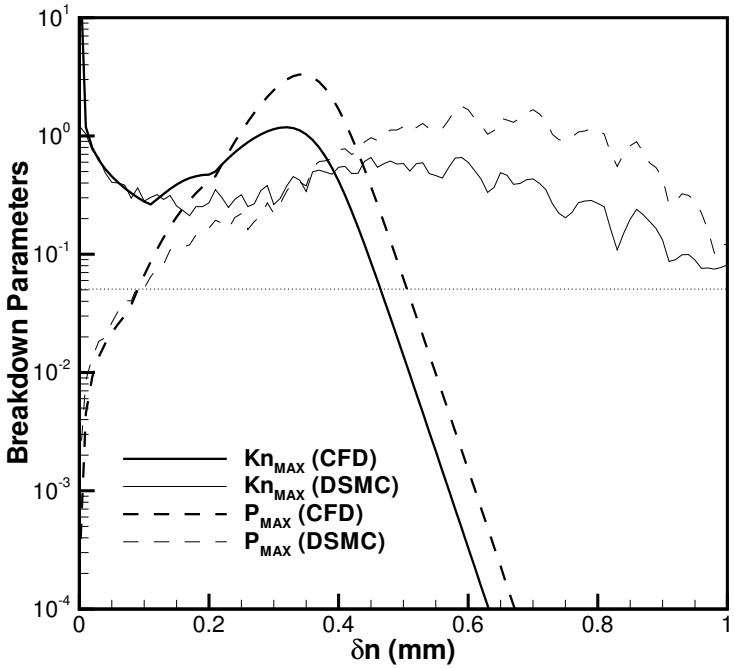

(b) Variation of Kn and P based on NS and DSMC solutions.

Figure 4.5: Profiles along the line normal to the cone surface at $x = 0.92$ mm.

and approaching the shock where the flow gradients are steep and the continuum equations break down again, the flow should be calculated using the DSMC method from here out to the free-stream boundary. $\mathrm{Kn}_{\max}$ is found to be quite successful for the prediction of the breakdown using a value of 0.05 for the criterion for switching between the numerical methods.

4.2.2 Hollow Cylinder/Flare

The second configuration investigated in this chapter consists of a hollow cylinder followed by a 30° conical flare, as depicted in Figure 1.2(b). The cylinder is aligned with the free stream. The leading edge is sharp and the hypersonic flow entering the hollow body does not interact with the external flow. Only the external flow is considered.

The DSMC computation employs 1000 by 200 cells with a total of more than 3.5 million simulation particles. The reference time step of this computation is 5 nsec. 800,000 time steps are computed on an IBM-SP machine to consume a total of about 176 hours on 16 processors and the last 100,000 time steps are sampled to obtain the results presented below. The CFD [61] simulation is performed on a structured grid with 2048 cells along the body surface and 512 cells normal to the body surface.

In Figures 4.6(a) and 4.6(b) comparisons of the density and translational temperature contours obtained with CFD and DSMC are shown. A general impression of the complex flow is the gas density is reduced by a factor of about 3 from the free-stream value in the region above the cylinder and then compressed more than 5 times by the flare. The temperature above the cylinder is increased due to viscous interaction and reaches a peak value of about 1,000 K. The strong compression caused by the flare leads to further heating with a peak value of approximately 1,500 K.

Detailed numerical studies of this flow can be found in References [25, 23, 43]. Notice the significant differences between the CFD and DSMC solutions around the compression corner. There is a larger separation and re-attachment region in the CFD solutions.

To study the continuum breakdown near the leading edge of the hollow cylinder in this case, comparisons for density, velocity and translational temperature along the line normal to the body at $x/L = 0.01$ [dotted line a in Figure 4.6(a)] are made in Figure 4.7(a). Since there are strong interactions between shock and viscous effects near the leading edge, the post-shock flow quickly merges with the boundary layer. Continuum breakdown is expected, as shown in the figure. The breakdown occurs from $\delta n = 0$ to about 1.1 mm. Breakdown parameters evaluated with various flow properties based on the CFD solution are displayed in Figure 4.7(b). The value of 0.05 is again chosen to be the criterion. Like the previous cone tip case, the Kn parameters predict the failure of the continuum approach at the body surface but the P parameters do not. The profiles of Kn and P calculated using the DSMC solution are shown in Figure 4.7(c). Again, the various forms of Kn can capture the continuum breakdown but the various forms of P do not. Focus on the $\mathrm{Kn}_{\max}$ and $P_{\max}$ that are shown in Figure 4.7(d). Keeping in mind that the DSMC technique must be applied in the region near the body surface, as discussed above, it is clear that $\mathrm{Kn}_{\max}$ based on DSMC crosses the 0.05 criterion line at about 1.1 mm which is the boundary of the continuum breakdown. Other parameters either under-estimate the breakdown range or fail to predict the breakdown in the region very close to the body.

Next, the middle of the cylinder is studied, where the shock and boundary layers separate. In Figure 4.8, profiles along the dotted line b in Figure 4.6(a) are shown

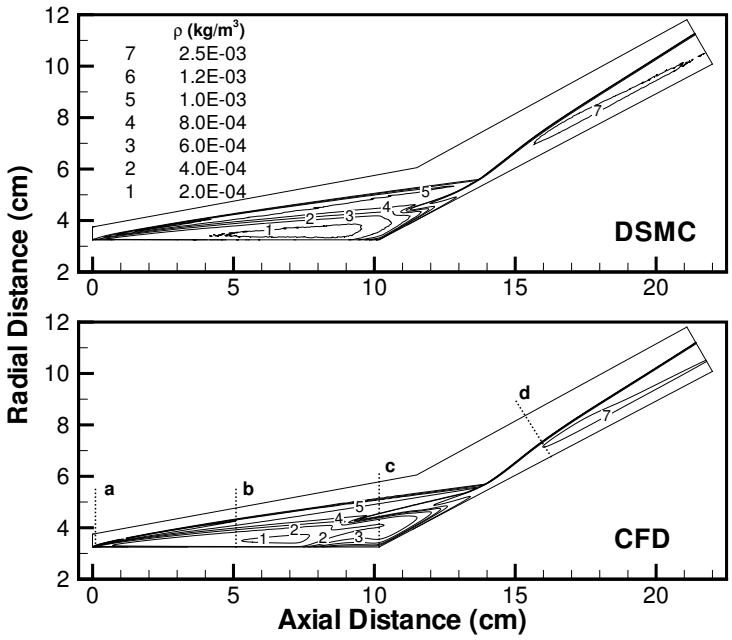

(a) Comparison of density.

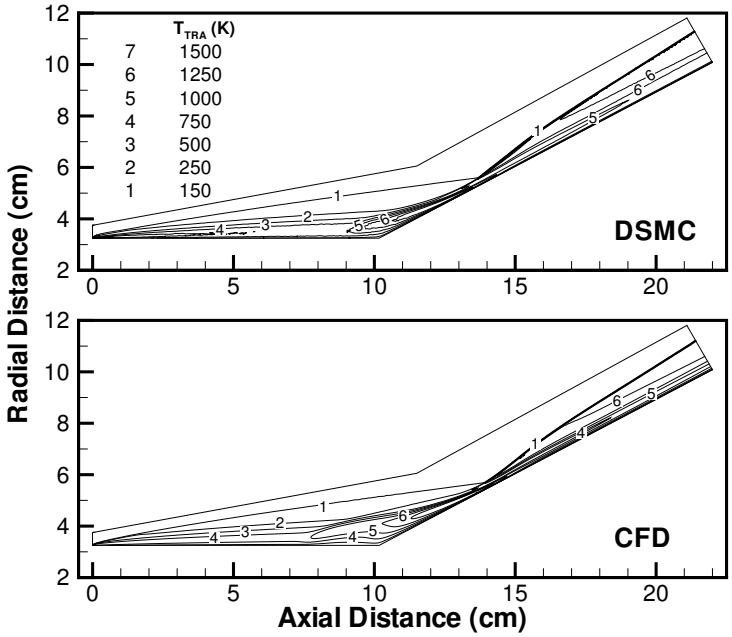

(b) Comparison of translational temperature.

Figure 4.6: Comparison of DSMC and CFD solutions of mass density and translational temperature for hollow cylinder/flare.

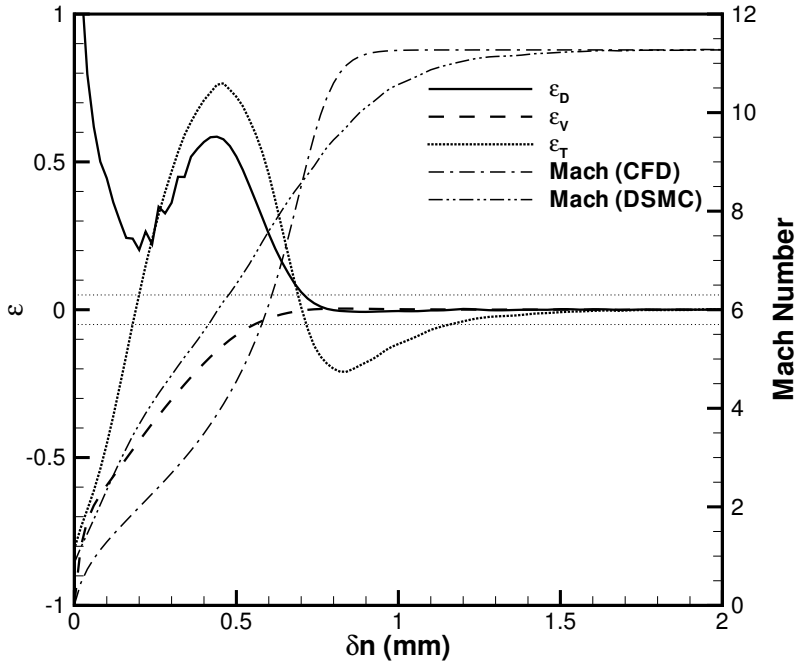

(a) Comparison of density, velocity, temperature and Mach number.

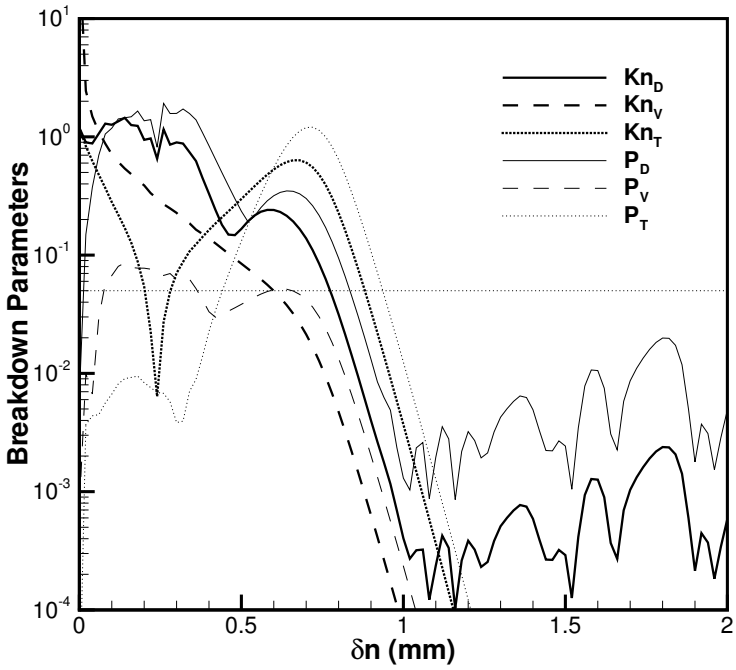

(b) Breakdown parameters based on NS solutions.

Figure 4.7: Profiles along the line normal to the cylinder surface at $x/L = 0.01$. (continued)

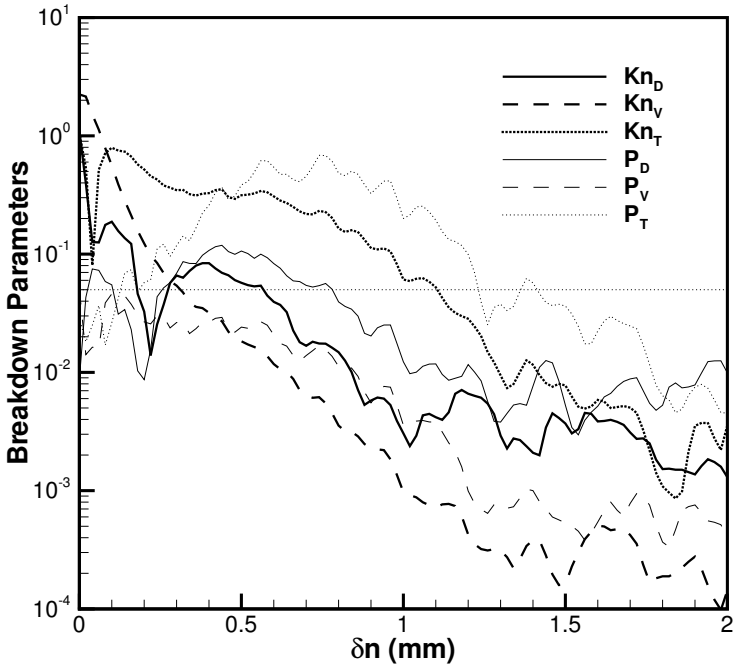

(c) Breakdown parameters based on DSMC solutions.

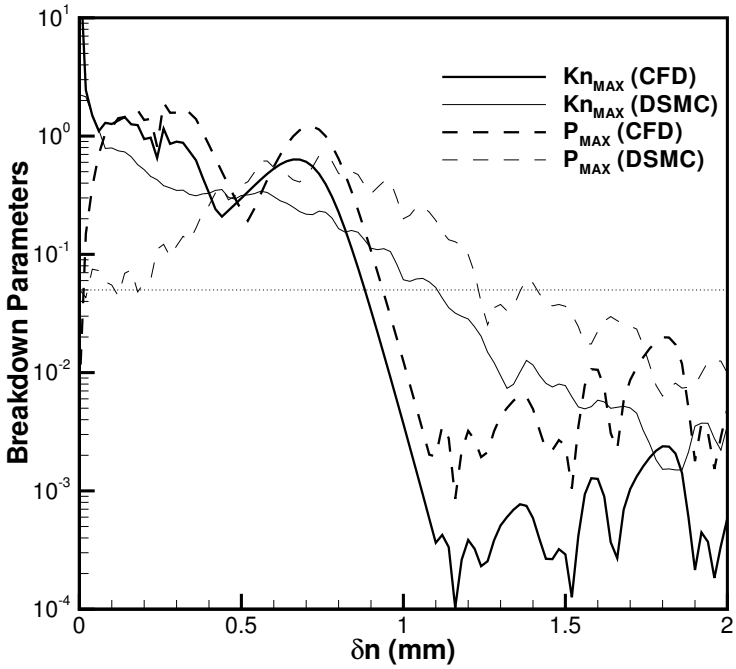

(d) Variation of $\mathrm{Kn}_{\max}$ and $P_{\max}$ based on NS and DSMC solutions.

Figure 4.7: Profiles along the line normal to the cylinder surface at $x/L = 0.01$.

of the flow properties considered and the breakdown parameters. Notice that the CFD shock is a little further from the wall than the DSMC shock at this station but their thicknesses are about the same. In the range of δn shown, there is not a single place where all the ϵ_Q considered lie within the $\pm 5\%$ band, except in the free stream. This is in part because of different shock locations obtained with the DSMC and CFD methods. More importantly, it is also in part because of the strong continuum breakdown from the steep flow gradients near the body. This can be verified in Figure 4.8(b) in which the values of $\mathrm{Kn}_{\max}$ based on both CFD and DSMC solutions are above the criterion line until about 6.5 mm. Although it is not a precise prediction for the range of the continuum breakdown, it is indeed an indication of $\mathrm{Kn}_{\max}$ being promising for prediction of the continuum breakdown in complex flows.

As mentioned in the beginning of this subsection, the flow structures obtained with the CFD and DSMC approaches are quite different around the junction of the cylinder and the flare. Flow properties along the dotted in c in Figure 4.6(a) are displayed in Figure 4.9(a). The profiles of Mach number for the CFD and DSMC solutions in the boundary layer are inconsistent to a large extent. Attention should be paid to the lower left corner of the figure where each Mach number profile shows two stagnation points, one is right at the junction and the other is in the separation zone. The second stagnation point is at about 5 mm for the CFD method and about 1.5 mm for DSMC above the body. One can also find a huge value of ϵ_V at about 1.5 mm. This is because Q_{DSMC} in Equation (4.6) is very small at a stagnation point.

The profiles of $\mathrm{Kn}_{\max}$ and $P_{\max}$ at the station are shown in Figure 4.9(b). The $\mathrm{Kn}_{\max}$ evaluated with the DSMC solution is still promising to predict the breakdown at the wall and covers the major portion of the region where the NS equations fail. At the shock front, the $\mathrm{Kn}_{\max}$ based on the CFD solution once again predicts the

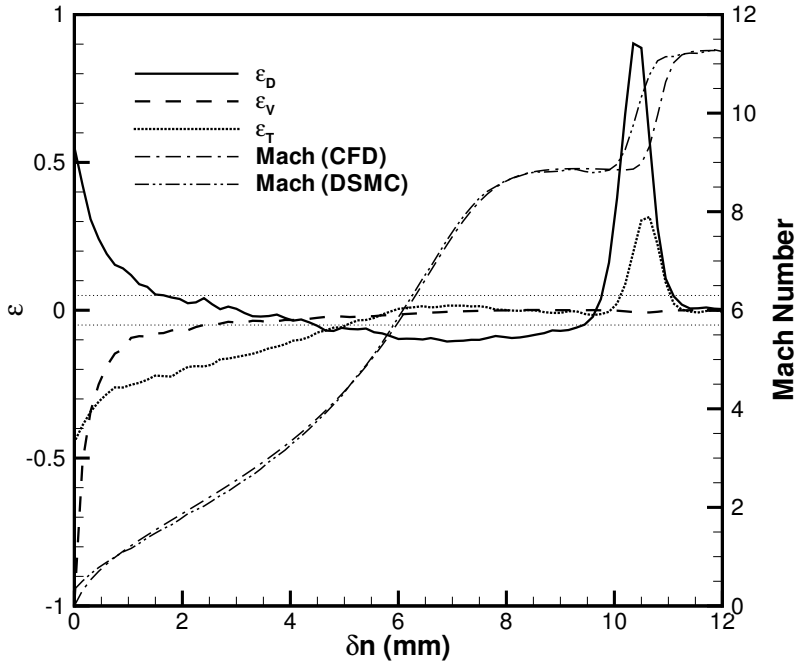

(a) Comparison of density, velocity, temperature and Mach number.

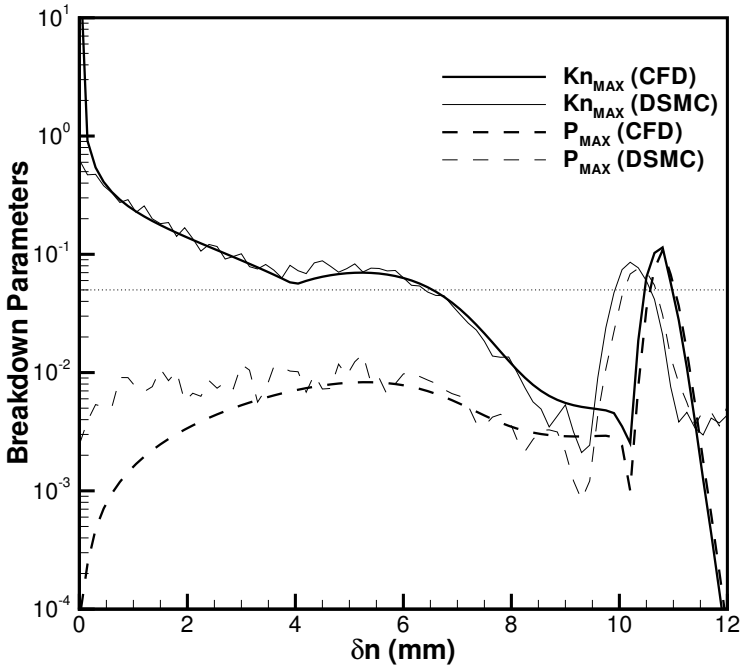

(b) Variation of Kn and P based on NS and DSMC solutions.

Figure 4.8: Profiles along the line normal to the cylinder surface at $x/L = 0.5$.

breakdown.

Finally, a station on the flare [dotted line d in Figure 4.6(a)] is examined where the free stream crosses a strong oblique shock [see Figure 4.10(a)]. The solutions of the CFD and DSMC methods have a large discrepancy in most regions, except for a narrow region close to the flare surface. As shown in Figure 4.10(b), $\mathrm{Kn}_{\max}$ successfully captures the breakdown on the wall but not in most regions of the boundary layer. On the other hand, $P_{\max}$ completely fails to predict the breakdown of the NS equations in the boundary layer. Both $\mathrm{Kn}_{\max}$ and $P_{\max}$ predict very well the breakdown across the shock.

Analogous to the first example, the hypersonic flow over the hollow cylinder/flare configuration is not described accurately using the NS equations in the regions near the body surface and the shock and the DSMC technique has to be used. Upstream of the shock, the CFD method can of course be employed.

4.3 Summary

The focus of the chapter is to identify a criterion that can successfully predict the conditions under which the continuum Navier-Stokes equations may be expected to fail in the hypersonic flows considered. Investigation was carried out by the detailed comparisons of numerical solutions obtained with CFD and DSMC techniques.

A new parameter, $\mathrm{Kn}_{\max}$, is proposed that is modified from original $\mathrm{Kn}_{\mathrm{GLL}}$ parameter. It is concluded that continuum breakdown is best predicted wherever the value of $\mathrm{Kn}_{\max}$ exceeds 0.05. For the simple sharp cone flow, the $\mathrm{Kn}_{\max}$ parameter can predict the failure of the continuum approach accurately in terms of the positions of significant differences between the CFD and DSMC solutions, including the regions immediately adjacent to the cone surface and at the shock front. For the

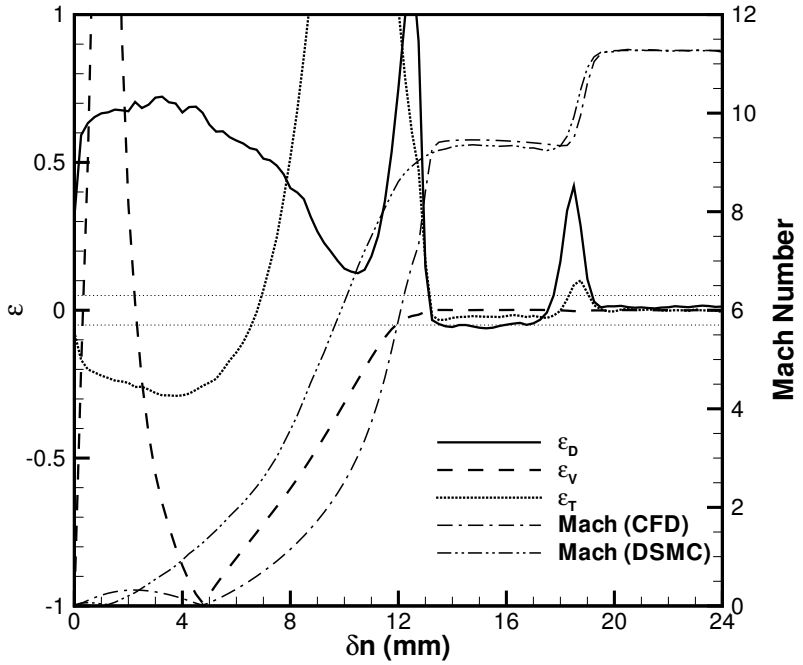

(a) Comparison of density, velocity, temperature and Mach number.

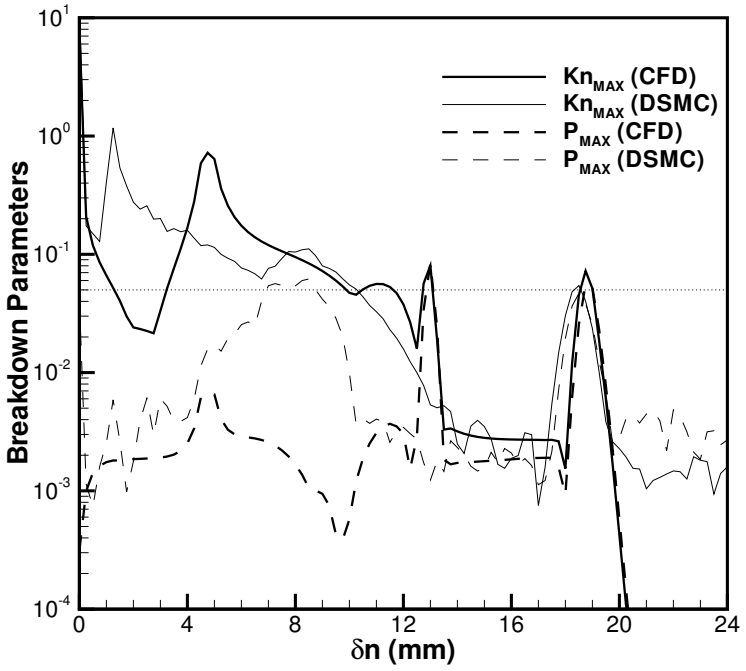

(b) Variation of Kn and P based on NS and DSMC solutions.

Figure 4.9: Profiles along the line normal to the cylinder surface at $x/L = 1.0$.

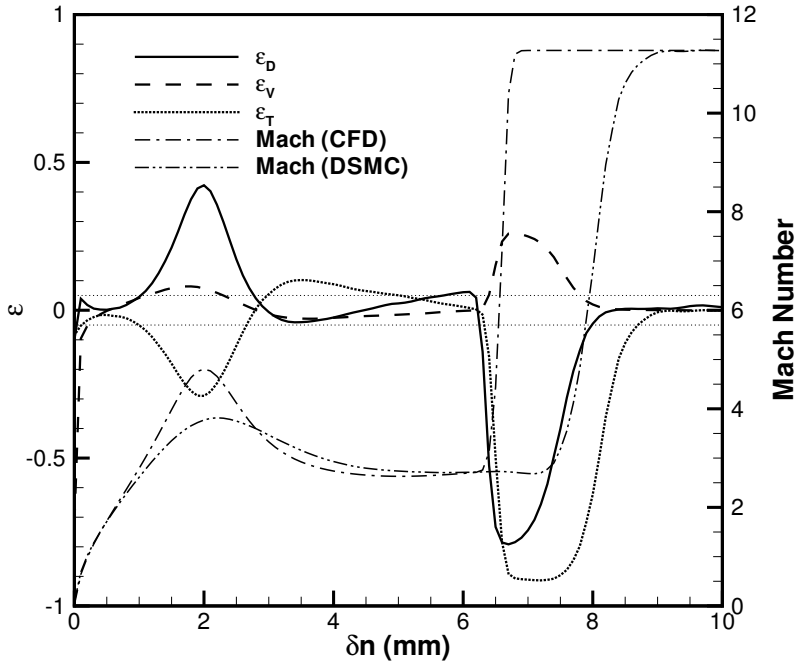

(a) Comparison of density, velocity, temperature and Mach number.

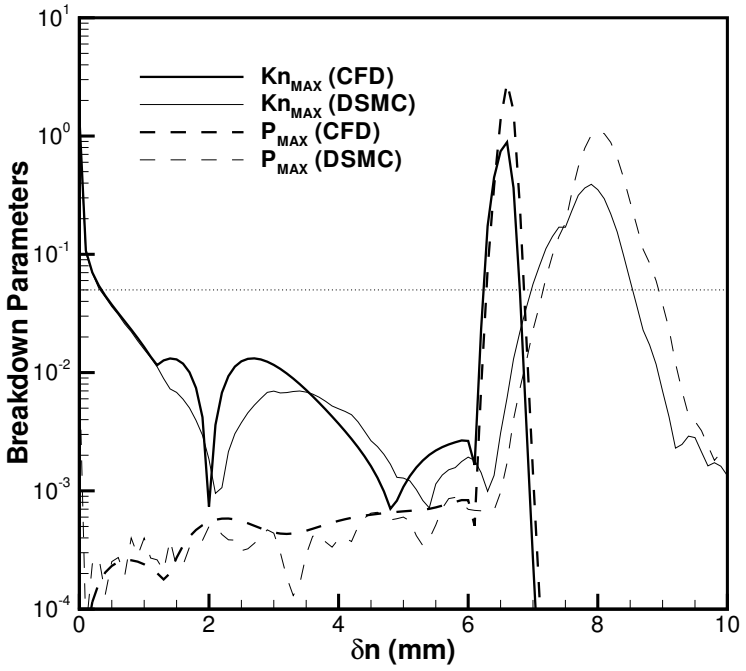

(b) Variation of Kn and P based on NS and DSMC solutions.

Figure 4.10: Profiles along the line normal to the flare surface at $x/L = 1.6$.

more complex hollow cylinder/flare flow, the parameter works fairly well to predict the continuum breakdown at the shock front and at the body surface. In general, Kn_{max} does not successfully capture the breakdown in the boundary layer. Since the detailed flow structures of the CFD and DSMC results for this complex flow do not agree to some extent in the boundary layer, whether Kn_{max} will work in this region is unknown until it is actually applied in the hybrid code.

When the Kn_{max} parameter is utilized in the coupled DSMC-CFD computations, it is expected that the entire flow field will be approximately separated into four layers. In the region very close to the body surface, the DSMC technique will be employed. In between the near-body region and the shock region, the CFD technique will be used. The DSMC technique will be employed again throughout the shock. In the free-stream region, it is efficient to utilize the CFD technique.

CHAPTER V

HYBRID PARTICLE/CONTINUUM APPROACH

In this chapter, the details of the hybrid approach that combines the CFD and DSMC methods are described. Specifically, the following four issues are addressed: (1) how the boundary conditions for the CFD method are provided at the domain interface, (2) how particles are handled when they escape from the DSMC domain, (3) how particles are generated in the CFD domain before they enter the DSMC domain, and (4) how the domain interface is determined based on the hybrid information. In addition, the strategy of the parallelization of the hybrid approach is described.

5.1 Domain Coupling

At the interface between the DSMC and CFD domains, macroscopic flow properties must be provided to the CFD method for evaluating the net fluxes and to the DSMC method for initializing the particles entering from the continuum region into the particle region. It is always a major issue for CFD to be provided with decent flow properties from the particle region because of the large statistical scatter associated with the DSMC method. However, the IP method preserves the macroscopic information in cells with very small statistical scatter. Therefore, it is a natural choice

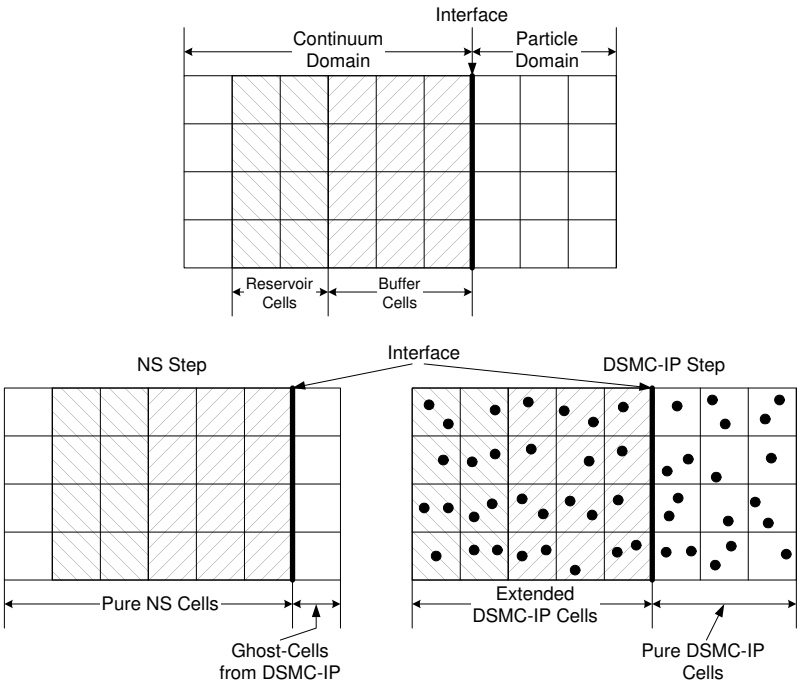

Figure 5.1: Interface cell types.

to utilize the IP information as the flow properties provided to the CFD method through the domain interface.

To implement the coupling between the particle method and the NS solver, buffer and reservoir DSMC-IP cells are introduced in the continuum domain adjacent to the domain interface, as depicted in Figure 5.1. A similar concept of reservoir cells was first proposed by Rovedo *et al.* [70].

The buffer DSMC-IP cells work as an extension of the particle domain (see lower right of the figure). Simulated particles that end their movement phase within the pure particle domain or in the buffer cells are retained. Those that leave these two regions are removed. For each time step, all simulation particles in the reservoir cells are first deleted and then re-generated based on the cell-centered NS information. The number of new particles is evaluated from the cell density value and the particle velocities are initialized to the Chapman-Enskog distribution based on the

corresponding cell values. The newly generated particles are randomly distributed within the reservoir cells.

In the continuum domain, the NS solver determines the interface continuum fluxes by using the NS variables and DSMC-IP cell macroscopic information. Since the macroscopic information in the particle cells is known at each time step, the DSMC-IP cells adjacent to the domain interface are treated as the ghost cells that provide the boundary conditions for flux computations (see lower left of the Figure 5.1).

Based on this coupling technique, there are six different types of cell: (1) pure particle cell, (2) particle interface cell, (3) continuum interface cell, (4) pure buffer cell, (5) reservoir cell, and (6) pure continuum cell. For each time step, cells of various types have their own different operations.

Pure particle cell A cell in the particle domain that handles particle movements and collisions and evaluates the IP fluxes in Equations (2.30) and (2.31).

Particle interface cell A cell on the boundary of the particle domain that handles particle movements and collisions and evaluates the IP fluxes in Equations (2.30) and (2.31) and the NS fluxes in Equation (2.16).

Continuum interface cell A cell on the boundary of the continuum domain that handles particle movements and collisions and evaluates the IP fluxes in Equations (2.30) and (2.31) and the NS fluxes in Equation (2.16).

Pure buffer cell A cell in the continuum domain that handles particle movements and collisions and evaluates the NS fluxes in Equations (2.16).

Reservoir cell A cell in the continuum domain that deletes all its particles, regenerates new particles based on its own NS information, handles particle

movements and collisions, and evaluates the NS fluxes in Equation (2.16).

Pure continuum cell A cell in the continuum domain that evaluates the NS fluxes in Equation (2.16).

5.2 Velocity Distribution In The Reservoir Cells

As studied in Chapter IV, the interface between the particle and continuum domains is located wherever the difference of the DSMC and NS solutions of a flow is 5%. Generally speaking, the flow in the vicinity of the interface, including the region covered by the buffer and reservoir cells, should not be considered as being in a state of equilibrium. It has been shown [28, 44] that initializing particles with the Maxwellian distribution is unacceptable in a particle method coupled with a Navier-Stokes solver and the Chapman-Enskog distribution must be employed. Unlike sampling of the Maxwellian distribution, which is trivial because the distribution has an analytical inverted form, sampling of the Chapman-Enskog distribution is complicated and needs some extra work.

The normalized Chapman-Enskog distribution can be expressed in the form

$$f(\mathbf{C}) = \mathcal{M}(\mathbf{C})\Gamma(\mathbf{C}), \tag{5.1}$$

where $\mathbf{C} = \mathbf{c}'/\sqrt{2kT/m}$ is the normalized thermal velocity and $\mathcal{M}$ is the Maxwellian distribution

$$\mathcal{M}(\mathbf{C}) = \frac{1}{\pi^{3/2}} \exp(-C^2).$$

The $\Gamma(\mathbf{C})$ term in Equation (5.1) represents the first order expansion in Sonine polynomials and is given as

$$\Gamma(\mathbf{C}) = 1 + (\mathbf{q}^* \cdot \mathbf{C})(\tfrac{2}{5}C^2 - 1) - \boldsymbol{\tau}^* : (\mathbf{CC}), \tag{5.2}$$

with

$$\tau_{ij}^* = \frac{\mu}{p}\left(\frac{\partial u_i}{\partial x_j} + \frac{\partial u_j}{\partial x_i} - \delta_{ij}\frac{2}{3}\frac{\partial u_k}{\partial x_k}\right),$$
$$q_i^* = -\frac{\kappa}{p}\sqrt{\frac{2m}{kT}}\frac{\partial T}{\partial x_i}.$$

The use of the astral symbol differentiates the above stress tensor and heat-flux vector from those in Equations (2.12).

In a reservoir cell, the macroscopic (IP) information for newly generated particles is set to the cell-centered NS values and the microscopic velocities are initialized to the Chapman-Enskog distribution using the acceptance-rejection scheme by Garcia and Alder [35]. To generate a thermal velocity vector for a particle, the scheme starts with finding $B \equiv \max(|\tau_{ij}^*|, |q_i^*|)$ and setting the amplitude parameter $A = 1 + 30B$. A vector $\mathbf{C}_{\text{try}}$ is then generated from the Maxwellian distribution $\mathcal{M}(\mathbf{C})$. The $\mathbf{C}_{\text{try}}$ is accepted if $A\mathfrak{R} \leq \Gamma(\mathbf{C}_{\text{try}})$; otherwise a new vector $\mathbf{C}_{\text{try}}$ is generated until the inequality is true. Finally, the molecular velocity vector for the particle is $\mathbf{c} = \sqrt{2kT/m}\,\mathbf{C}_{\text{try}} + \mathbf{V}$.

5.3 Hybrid Approach Profiling

It is interesting to study how the time spent in a hybrid simulation is shared by the CFD, DSMC, and IP components. A study of this kind is usually called *profiling*. A simple 1-D uniform argon flow is set up to investigate this issue. The uniform flow has a velocity of 500 m/s, a temperature of 300 K, and the number density in the flow is about $1.609 \times 10^{21}\,\text{m}^{-3}$. The particular selection of flow type for the profiling study is not too important based on two main reasons. First, the operations performed in CFD are almost the same for each time step regardless of the flow type. Second, particle movement and the determination of particle collisions take most of

the time in the particle method for each time step and their operations are relatively independent of the flow type. The number of collisions depends on flow type but actual collisions take place for a very small portion of all the simulated particles due to the mean collision time limitation. Therefore, the effect of the number of collisions is considered insignificant in the profiling study.

Numerical experiments for the profiling study are performed on a grid that has 400 uniform cells and spans 0.04 m. In all experiments, 10 layers of buffer cells and 2 layers of reservoir cells are employed. To simplify the analysis, all the cells in the particle domain and buffer zone are regarded as particle cells. The percentage of the particle cells is defined as the ratio of the number of the particle cells to the number of all the cells in the grid. The time usages by the CFD, DSMC, and IP components can be described as functions of the percentage of the particle cells and the number of particles per cell. It is easy to understand that when a pure CFD simulation is performed, the majority if not all the time spent belongs to CFD. In contrast, when a pure particle simulation is performed, the majority of the time spent is by the DSMC and IP methods. It is also easy to understand that at a certain percentage of particle cells, increasing the number of particles per cell increases the time taken by the particle methods because more particles need to be processed but this change has no effect on CFD.

The correlations between the time usages by the CFD, DSMC, and IP components and the percentage of particle cells in the present hybrid approach are shown in Figure 5.2 for the cases of 50 particles and 100 particles per cell. The percentage of time for an individual method in a simulation is defined as the time spent by the method divided by the overall duration of the simulation. It is shown that the percentage of the time consumed by CFD is monotonically decreasing with the

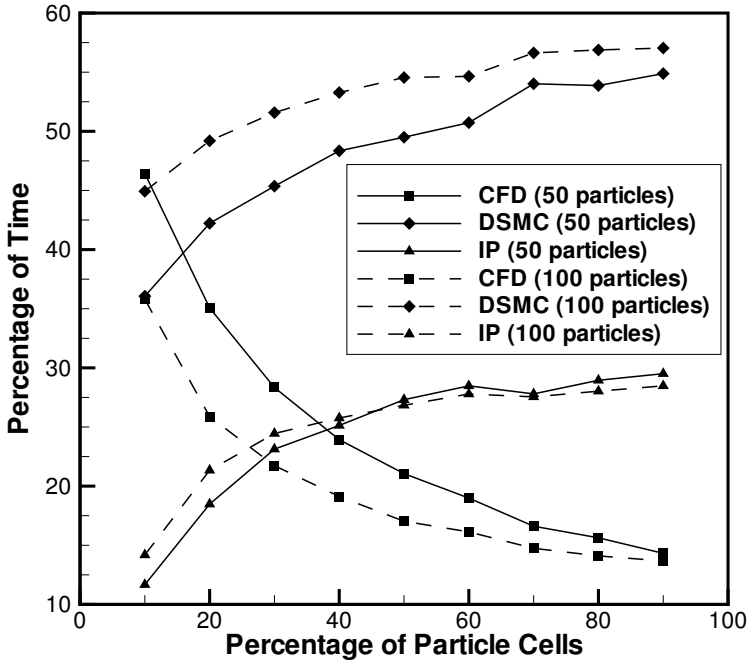

Figure 5.2: Correlations between time usages by the numerical methods and percentage of particle cells.

percentage of particle cells increasing. On the other hand, the percentages of the time spent by the DSMC and IP methods are approximately monotonically increasing with the percentage of particle cells increasing. In the case where 50 particles are employed in each cell and 10% of the total number of cells are particle cells, the CFD method consumes about 46% of the total simulation time. This is the only case among all the cases considered where the CFD time usage is higher than the other two methods.

A typical hybrid simulation usually has 40-50% of the total number of cells in the particle domain and buffer zone. In this range, the time usages by the DSMC and IP methods are, respectively, about 48-54% and 25-27% of the total simulation time. In the same range, CFD always spends the least amount of time and its time usage is between 17% to 24%. Because the percentages of particle cells in the two hybrid simulations in Chapter VI are about 40% to 50% and there are 50 to 80 particles

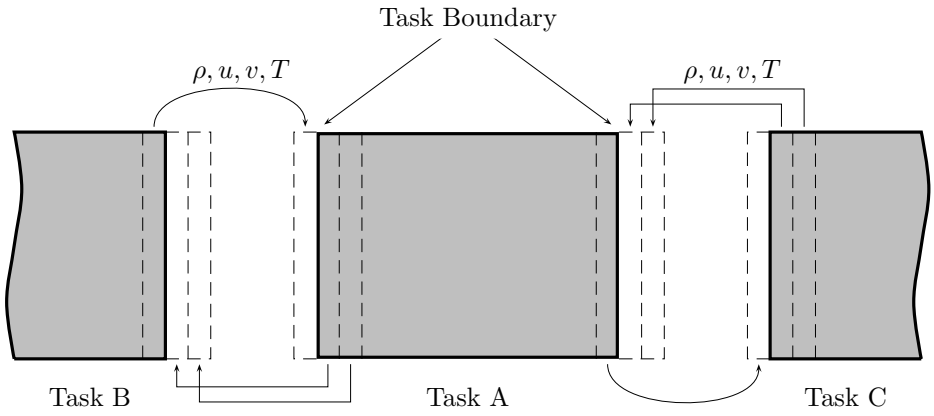

Figure 5.3: Information communication between parallel tasks.

per cell, it is expected that the time usages by CFD, DSMC, and IP approximately follow the values just mentioned.

5.4 Parallelization

Consider that a structured grid is employed and that the whole computational domain is divided into several rectangular blocks such that the boundary between two adjacent blocks is a vertical line, as depicted in Figure 5.3. In a parallel computer, each individual block is handled by a processor and is termed a *task*. Under such a setup, particle movements between two adjacent tasks are easy to be carried out. When a simulated particle needs to move across the boundary of the task which it is within, only its velocity components and final position are required to be sent to the neighboring task. For instance, assuming that a simulated particle is originally in Task A in Figure 5.3 and is about to move across the right task boundary and enter Task C, only the particle's velocity components and final position are passed to Task C and all records associated with the particle in Task A can be removed.

On the other hand, special attention is necessary for the flux evaluation described in Section 2.2.2. It is clear from Figure 2.1 that the flux evaluation on the right

boundary of a task, say Task A in Figure 5.3, needs information in two layers of cells from the right neighboring task, Task C. Analogously, the flux evaluation on the left boundary of Task A needs information in one layer of cells from the left neighboring task, Task B. Accordingly, when the hybrid approach is performed on a parallel computer, each individual task, except for the right-most and left-most tasks, has three extra layers of cells, with two attached to its right boundary and one attached to its left boundary. Before each time step is started, IP or NS information in the cells of the extra layers is acquired from the neighboring tasks, as shown in Figure 5.3.

5.5 Information Interpretation

Imagine the hybrid solution is extracted from a line crossing a particle region that lies between two continuum regions. There are three types of information along this line, as illustrated in Figure 5.4. There is only the NS information in the continuum regions whereas there is both the DSMC and the IP information in the particle region. Since the IP and the NS information are coupled at the domain interface, they form a continuous profile in a natural manner. Moreover, it is this NS-IP-NS information that is used to evaluate the breakdown parameter in Equation (4.2). On the other hand, the DSMC information is isolated in the particle region. This kind of profile will be largely seen in the hybrid results presented in the next chapter.

It is interesting to point out that the DSMC information at the domain interface is not necessarily the same as the IP, or NS, information. This is because the buffer cells are part of the continuum domain and the DSMC information in them is not usually shown. If the DSMC information in the buffer cells is included, as illustrated in Figure 5.5, the DSMC information at the edge of the buffer cells should be consistent

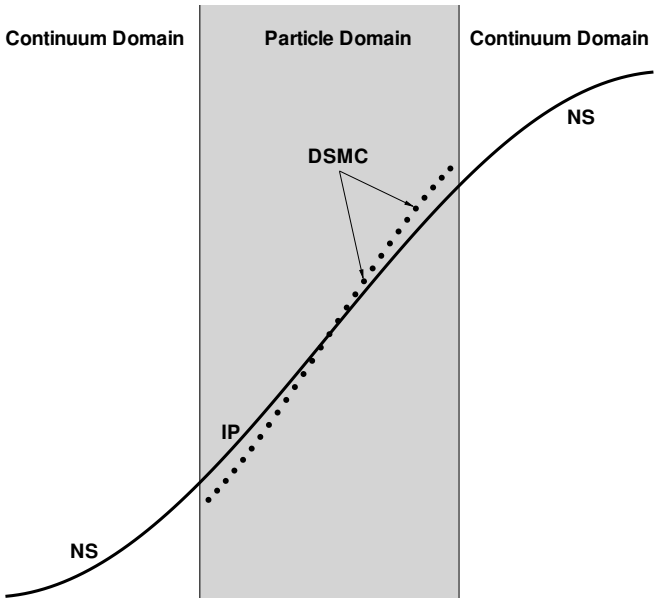

Figure 5.4: Simulation information in each various domain.

with both IP and NS information. A numerical example for a Mach 1.55 shock in argon is provided in Figure 5.6. Significant differences between the DSMC and IP information can be found on the boundary of the particle region (shaded area) and the differences largely vanish at the edge of the buffer cells (dotted lines).

5.6 Outline of The Hybrid Approach

Since the current hybrid code can be run in pure CFD or hybrid DSMC/CFD modes, the procedure of performing a hybrid simulation is outlined as follows.

1. Obtain a steady state CFD solution.

2. Use the CFD solution to determine the interface(s) between the particle and continuum domains and to assign a cell type for each cell.

3. Perform a hybrid simulation for a certain number of time steps.

4. Check if the hybrid solution is satisfactory by comparing it with either exper-

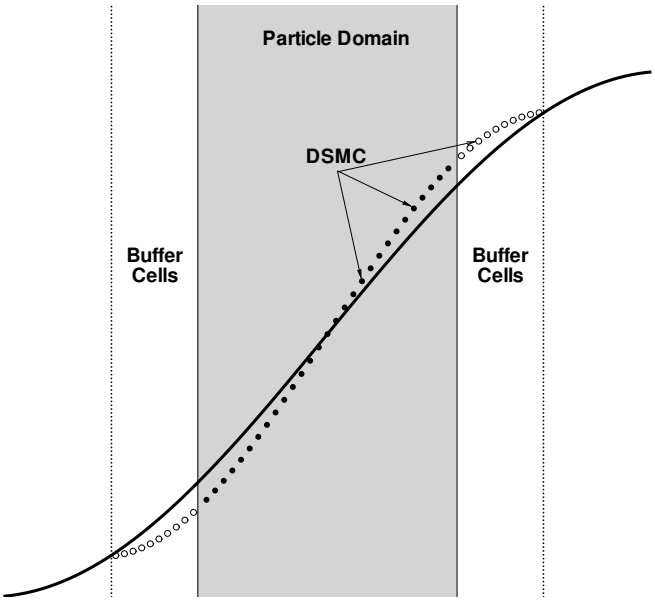

Figure 5.5: DSMC information in particle and buffer cells.

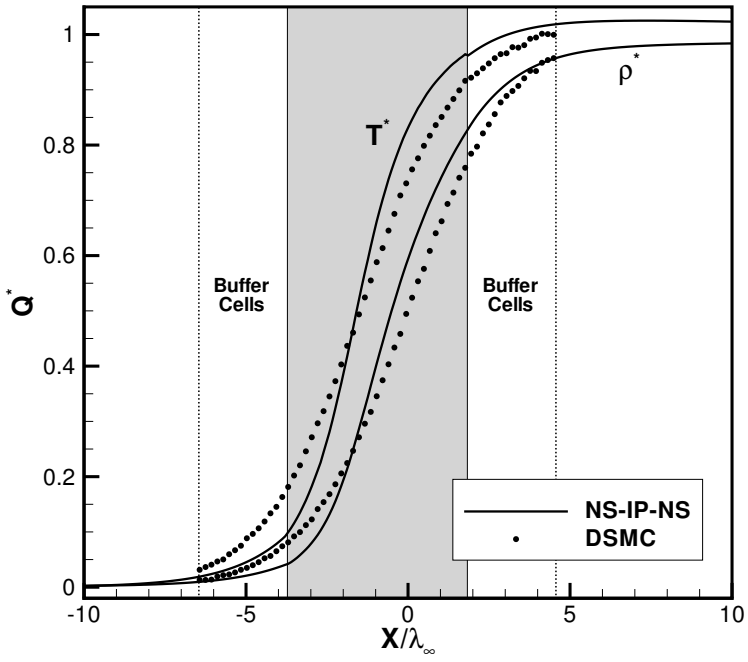

Figure 5.6: DSMC and IP/NS information for a Mach 1.55 shock in argon.

imental data or a pure DSMC solution. If the hybrid solution is satisfactory, stop the hybrid simulation. Otherwise,

5. Use the hybrid solution to determine the new domain interface and assign a new cell type for each cell.

6. Go back to Step 3 and repeat the loop.

In cases where the initial CFD solution is difficult to obtain in Step 1, the domain interface and a cell type for each cell can be given manually. The whole computational domain can be initialized by a set of reference values, for instance, the freestream conditions. Steps 3 to 6 of the above procedure are then applicable.

CHAPTER VI

HYBRID SIMULATIONS OF HYPERSONIC FLOW OVER BLUNTED AND SHARP BODIES

Two numerical examples are considered in this chapter to test the accuracy and efficiency of the hybrid approach. The first example is a Mach 12.6 nitrogen flow over a 25° half angle blunted cone and the second example is a Mach 12.4 nitrogen flow over a hollow cylinder/flare. The freestream conditions of both examples are given in Table 3.1.

Although it has been concluded in Chapter IV that $\mathrm{Kn}_{\max} = 0.05$ is a good criterion for determining the rarefied and continuum domains, a more conservative criterion of $\mathrm{Kn}_{\max} = 0.03$ is actually set in the hybrid simulations, unless stated otherwise. Besides, two layers of reservoir cells are employed in all hybrid simulations.

6.1 Blunted Cone Tip

The configuration of the blunted cone tip has been discussed earlier in Chapter III. All simulations in this section are performed on a structured grid that has 600 cells along the cone body and 300 cells normal to the body. In the hybrid simulation, a steady state solution is first obtained by computing the entire flow field with an implicit CFD scheme. Using the steady state solution and breakdown crite-

rion, locations of the interfaces between the continuum and the particle domains are determined. In the particle region, cell values are set to the CFD steady state results and simulation particles are initialized to the local Chapman-Enskog distribution. During the process of a hybrid simulation, domain interfaces are re-evaluated every 100,000 time steps.

6.1.1 Results Obtained With 6 Layers of Buffer Cells

The hybrid code is first run with 6 layers of buffer cells. The particle domains initially and after a million hybrid simulation iterations are illustrated in the shaded areas of Figure 6.1. At the beginning of the hybrid simulation, about 25.9% (46,589) of the total number of cells are in the particle domain. This value increases gradually with time and reaches about 33.4% (60,051) at the end of the simulation. Each cell in the particle domain has about 50 simulation particles on average. The reference time step in the hybrid computation is 0.5 nsec. The hybrid method results presented here are obtained by sampling once for every three steps over the last 60,000 time steps.

The total run time of the hybrid simulation on an Intel Linux cluster with 20 1-GHz processors is approximately 130 hours. A detailed comparison for the computational time consumed by various numerical methods will be given later.

Flow Fields

Comparisons of the translational temperature and density contours obtained with pure DSMC and the hybrid methods are made in Figure 6.2. It it easy to observe in Figure 6.2(b) that the bow shock in front of the leading edge of the cone is thicker in the DSMC solution. Otherwise, the hybrid method results are in good general agreement with the pure DSMC results. Additionally, the hybrid method provides

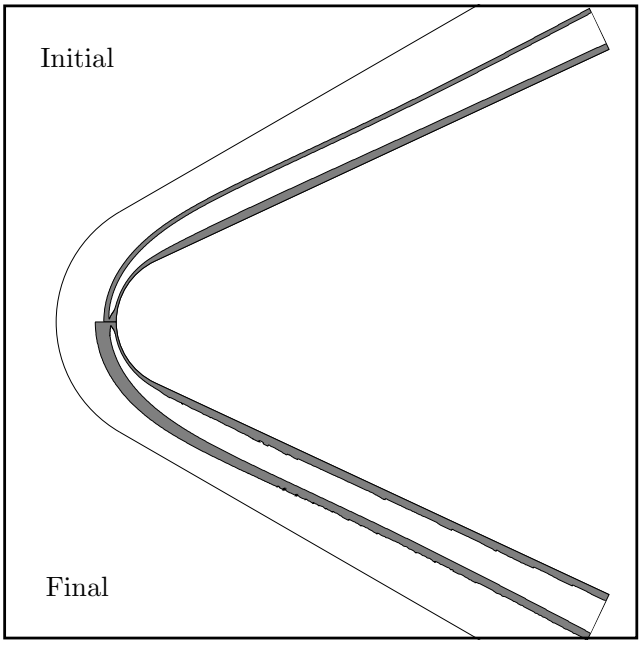

Figure 6.1: Particle domain in hybrid simulation for a blunted cone.

much smoother results.

As pointed out in Section 5.5, the hybrid results in Figure 6.2 comprise two kinds of information. In the particle domains (the shaded areas in Figure 6.1) hybrid results are represented by IP information and in the continuum domains by NS information.

Surface Properties

In Figure 6.3, comparisons of surface pressure and heat transfer coefficients obtained with numerical methods and the experiment are made. In these figures, the profiles labeled "Hybrid (DSMC)" represent only the DSMC information. The profiles labeled "Hybrid (IP)" represent only the IP information because the cone body is entirely enveloped by particle cells. Generally speaking, the flow properties predicted by the hybrid method along the wall are in excellent agreement with the DSMC solutions.

Keep in mind that the hybrid simulation is initialized with the steady state CFD

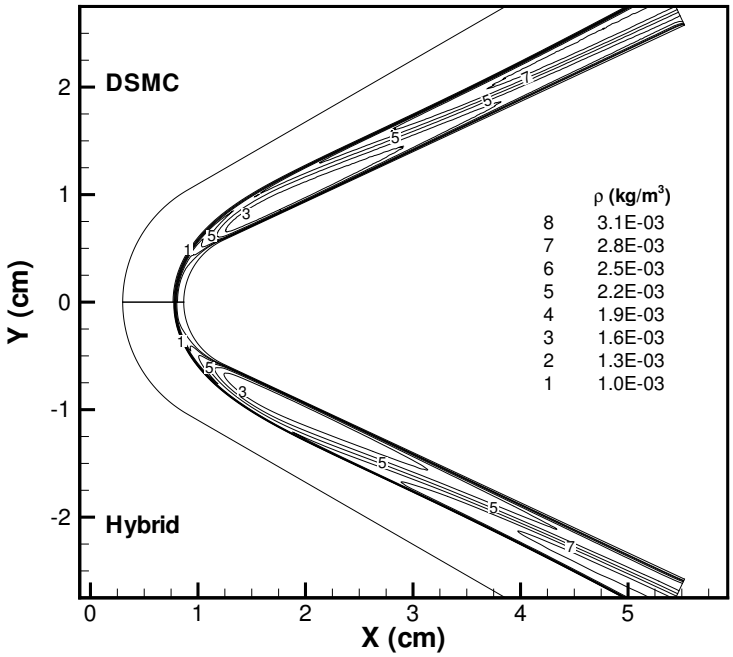

(a) Comparison of mass density.

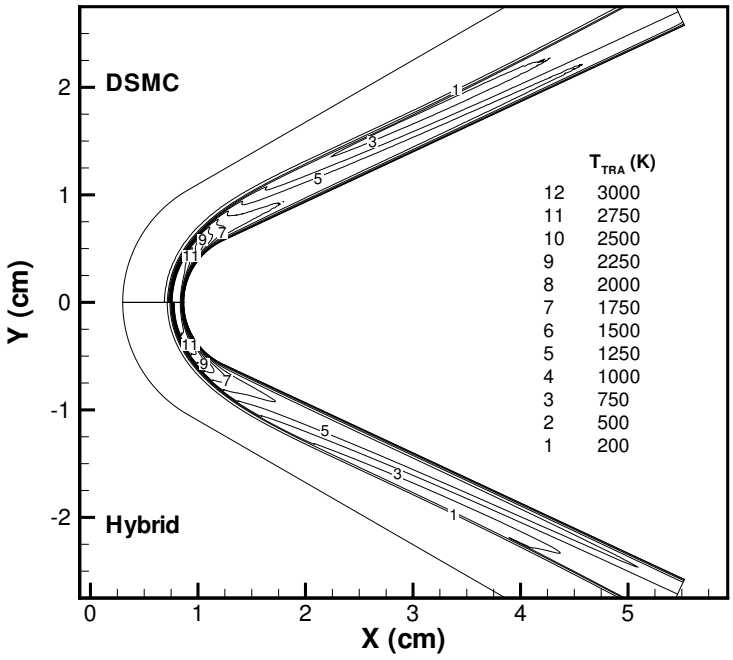

(b) Comparison of translational temperature.

Figure 6.2: Comparison for mass density and translational temperature of DSMC simulation and hybrid simulation with 6 layers of buffer cells for the flow over a 25° blunted cone.

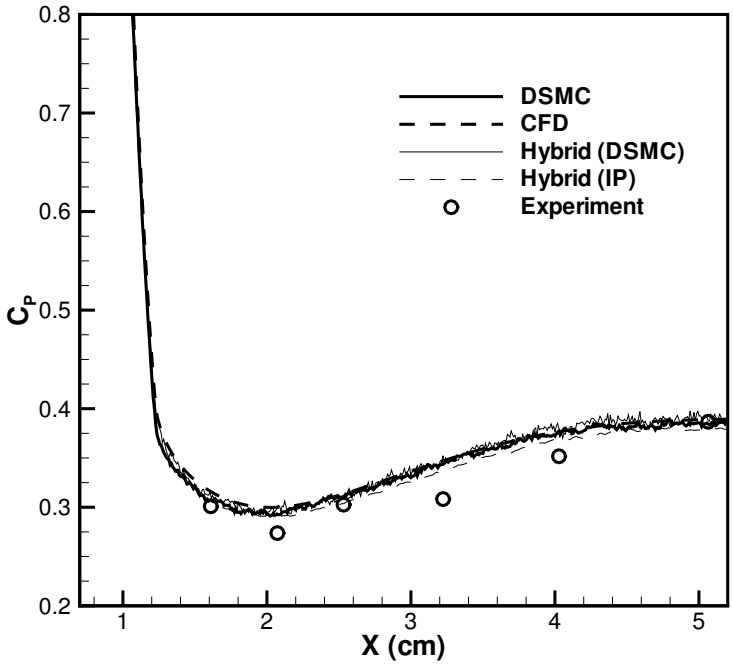

(a) Comparison of surface pressure.

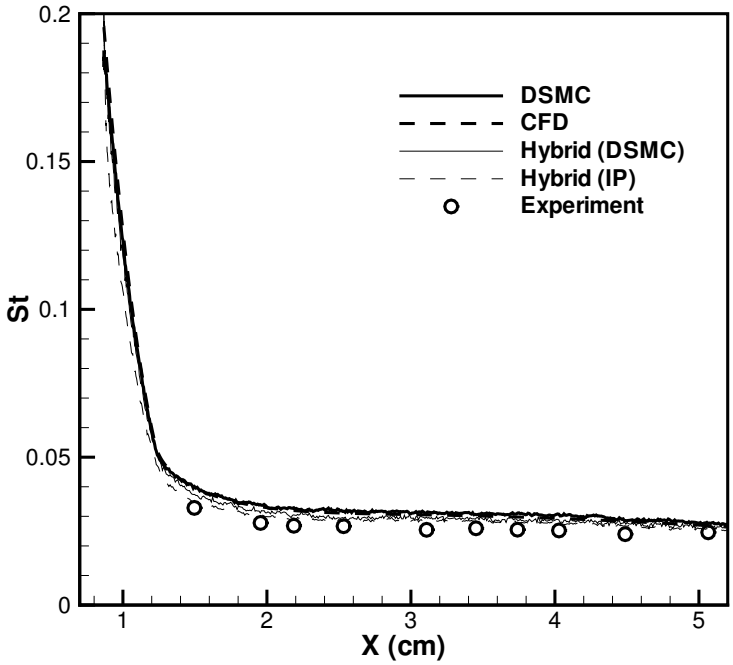

(b) Comparison of surface heat transfer rate.

Figure 6.3: Comparison of surface properties with different numerical methods and experimental data for the flow over a 25° blunted cone.

solution, the CFD solution is very close to the DSMC solution on the cone surface, and the hybrid results are very similar to the CFD results on the cone surface. This suggests that CFD, DSMC, and hybrid solutions are approximately the same in the vicinity of the cone body. This also suggests that if the initialized CFD solution is close to the DSMC solution, the hybrid solution will stay with the solution. More detailed comparisons are provided in the next section.

Detailed Comparisons

In Figure 6.4, profiles of the pure DSMC, CFD and hybrid solutions are plotted in detail along the stagnation line for comparison. The vertical dotted lines in the figures indicate the interfaces between the continuum (right) and particle (left) domains. Similar to the contour plots above, the profiles labeled "Hybrid (IP/NS)" consist of two kinds of information which are IP information in the particle domain and NS information in the continuum domain. The profiles labeled "Hybrid (DSMC)" contain only the DSMC information in the particle domain and no information in the continuum domain.

Flow along the stagnation line can be viewed as a hypersonic flow that passes through a strong normal shock and rapidly decelerates to rest at the wall. In the shock wave, the flow is strongly nonequilibrium, and the CFD, IP, and pure DSMC solutions are therefore expected to be different to a large extent. In the temperature profile, it is evident that the shock thickness and strength represented by the CFD and hybrid-IP/NS results are significantly different from the DSMC result. This is consistent with the results shown in Figure 3.9(b) and Figure 6.2(b), respectively. On the other hand, the hybrid-DSMC results are in outstanding agreement with the pure DSMC results and prove that the hybrid technique really improves the physical

accuracy compared to CFD.

A similar comparison between the pure DSMC, CFD, and hybrid solutions for translational temperature, density and velocity at $x = 2$ cm is displayed in Figure 6.5. At this location, the nonequilibrium effects start to weaken, and the Navier-Stokes equations coupled with the slip-boundary models perform fairly well. As shown in the figures, the CFD and DSMC solutions are close to each other except in the shock region.

The whole computational domain at this location is divided into four sub-domains along the δn direction: particle (I: $0 < \delta n < 0.72$), continuum (II: $0.72 < \delta n < 3.1$), particle (III: $3.1 < \delta n < 3.96$), and continuum (IV: $\delta n > 3.96$). It is shown that the temperature and density predicted by the hybrid approach are in good agreement with the pure DSMC solutions, except near the shock region.

The whole computational domain is also divided into four sub-domains along the δn direction at $x = 4$ cm. Comparisons of translational temperature, density and velocity profiles obtained with different methods are plotted in Figure 6.6. In general, the results calculated by using the hybrid approach are very close to the pure DSMC results in the region near the cone surface but just qualitatively agree with the pure DSMC results in the shock region.

6.1.2 Results Obtained With 10 Layers of Buffer Cells

Since buffer cells work as an extension of the particle domain, the more layers of buffer cells that are employed, the more collisions are experienced by the particles before they enter from the continuum region to the particle region. As a result, the velocity distribution of the particles can deviate more from the Chapman-Enskog distribution and is better able to describe the nonequilibrium state in the rarefied

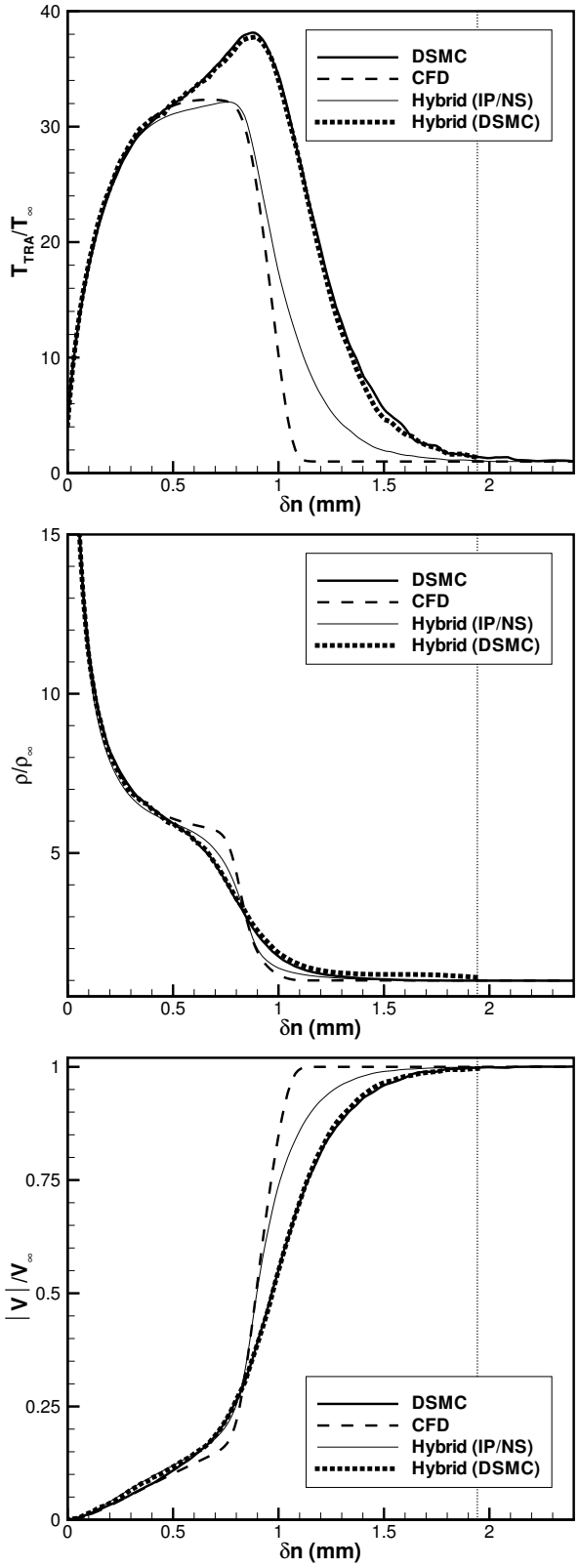

Figure 6.4: Comparisons for profiles along the stagnation line when 6 layers of buffer cells are employed.

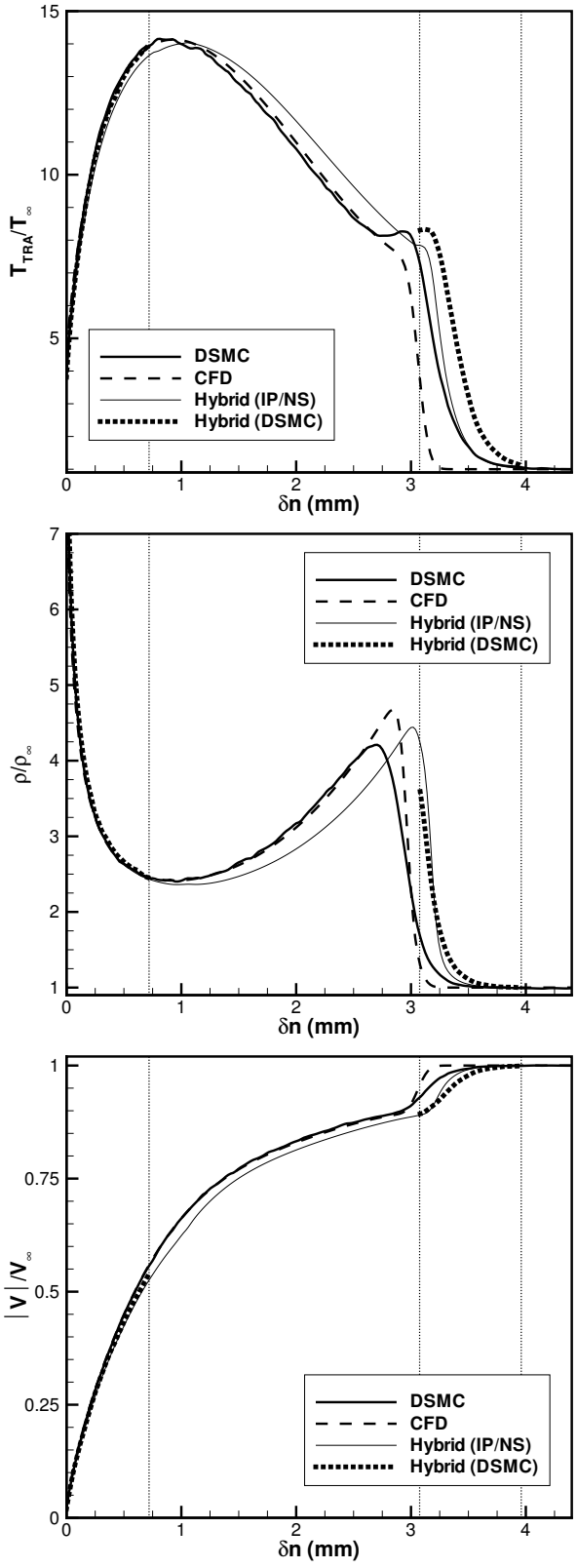

Figure 6.5: Comparisons for profiles along the line normal to the cone at $x = 2$ cm when 6 layers of buffer cells are employed.

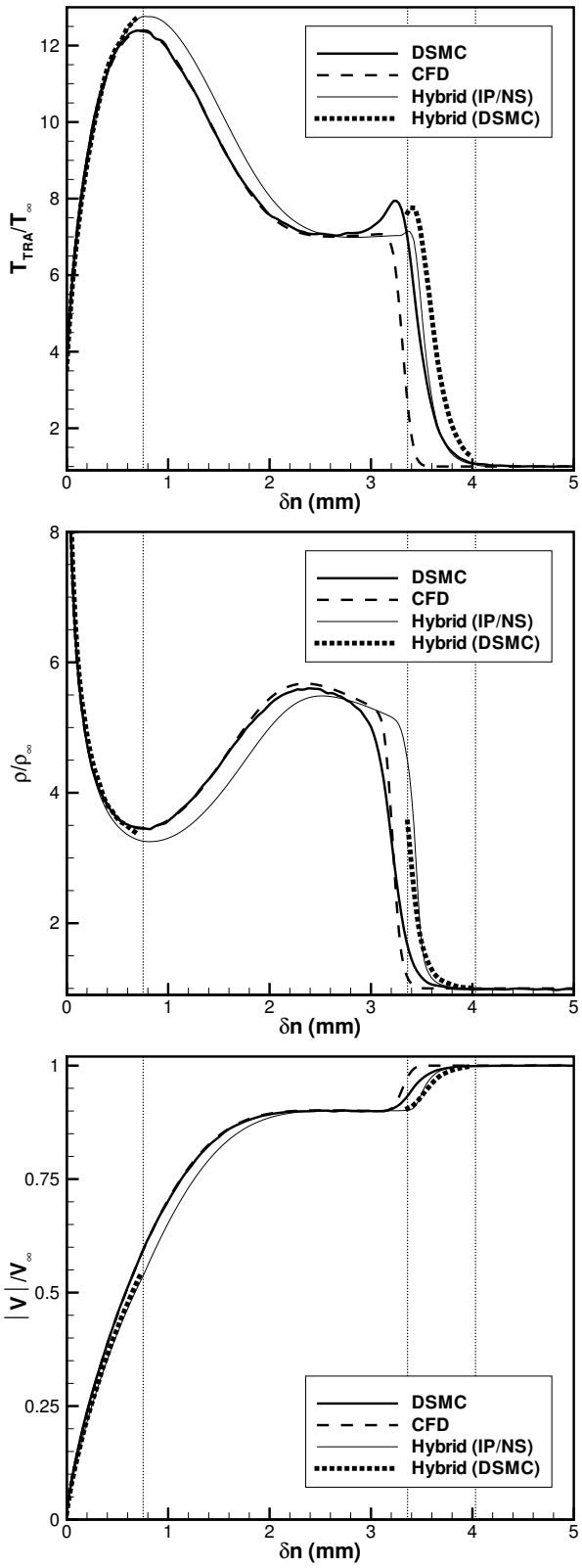

Figure 6.6: Comparisons for profiles along the line normal to the cone at $x = 4$ cm when 6 layers of buffer cells are employed.

region.

In this section, the number of layers of buffer cells is increased to 10 while the other parameters remain the same as in the last section. The number of particle cells after one million hybrid simulation steps is 57,208 that is slightly less than in the last section. The flow property profiles along the stagnation line and the lines normal to the cone at $x = 2$ and 4 cm are shown in Figures 6.7 to 6.9. It is evident that the hybrid-DSMC results are improved substantially in the shock region and are in very good agreement with the pure DSMC results. By contrast, the change in the regions near the wall is insignificant.

As described in Section 5.5, interfaces between continuum and particle domains are determined from the hybrid-IP/NS information. However, careful examination of the flow property profiles reveals that some interfaces are placed at locations with very large gradients. Take the density profile in Figure 6.9 for example. The domain interface near the shock rear edge is at about $\delta n = 3.3$ where a significant density gradient is observed. Similar behavior can be found in Figure 6.6 and in the profiles obtained with 6 layers of buffer cells. Since it is generally believed that the particle domain should be sufficiently large to contain the entire shock, the domain interface is obviously being placed at a wrong location. The reason for the wrong placing is because the breakdown parameter in terms of density, $\lambda|\nabla\rho|/\rho$, is evaluated by dividing a large gradient by a high value of density. As a result, the breakdown parameter in terms of density is lower than the cut-off value. This issue must be addressed in the future and will be discussed in the last chapter.

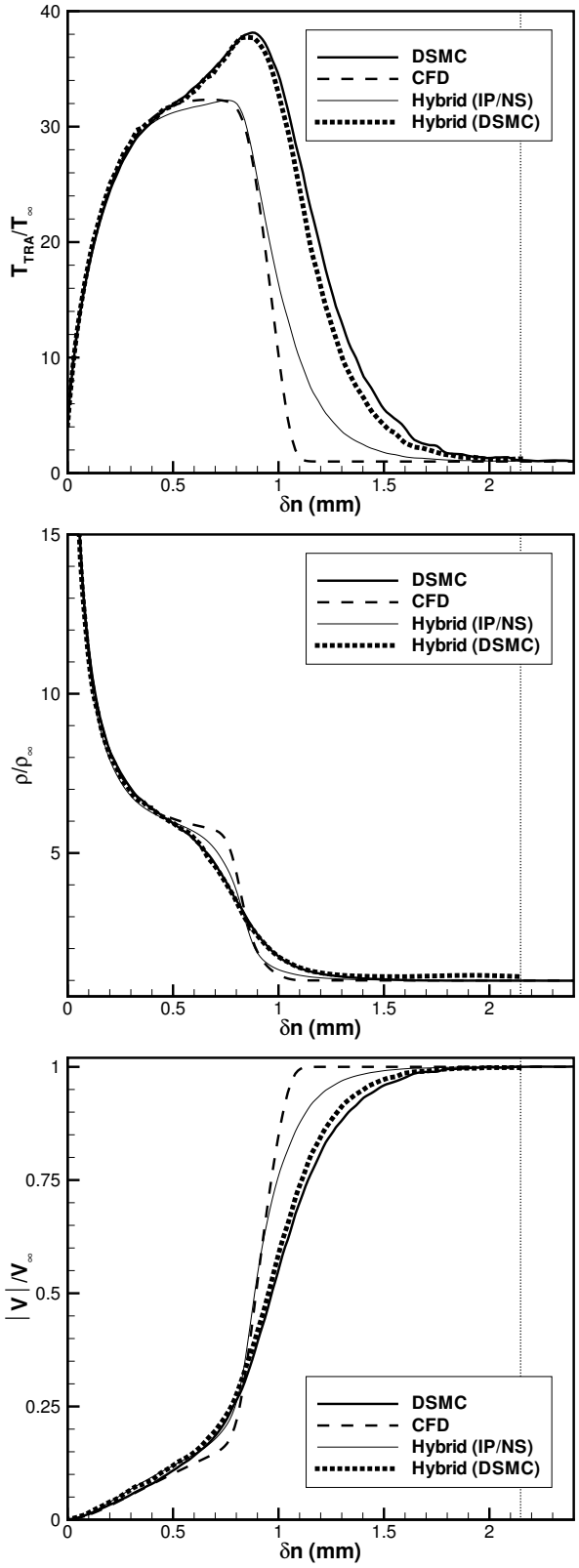

Figure 6.7: Comparisons for profiles along the stagnation line when 10 layers of buffer cells are employed.

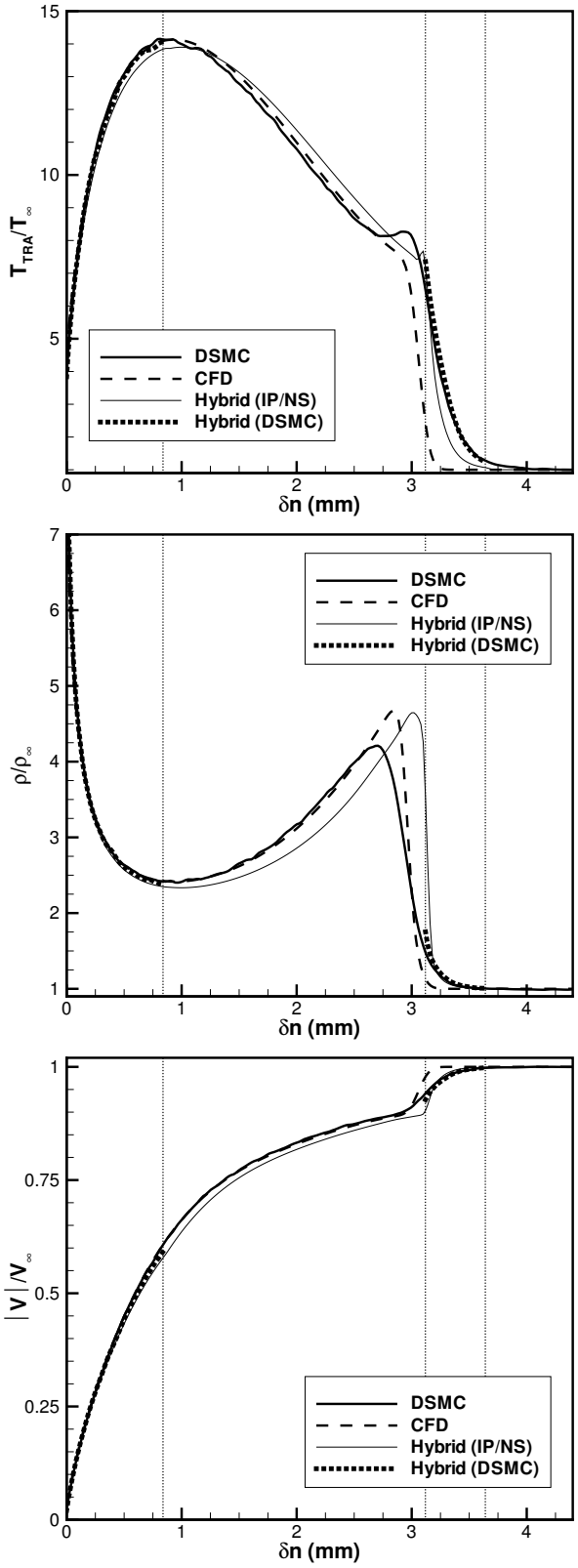

Figure 6.8: Comparisons for profiles along the line normal to the cone at $x = 2$ cm when 10 layers of buffer cells are employed.

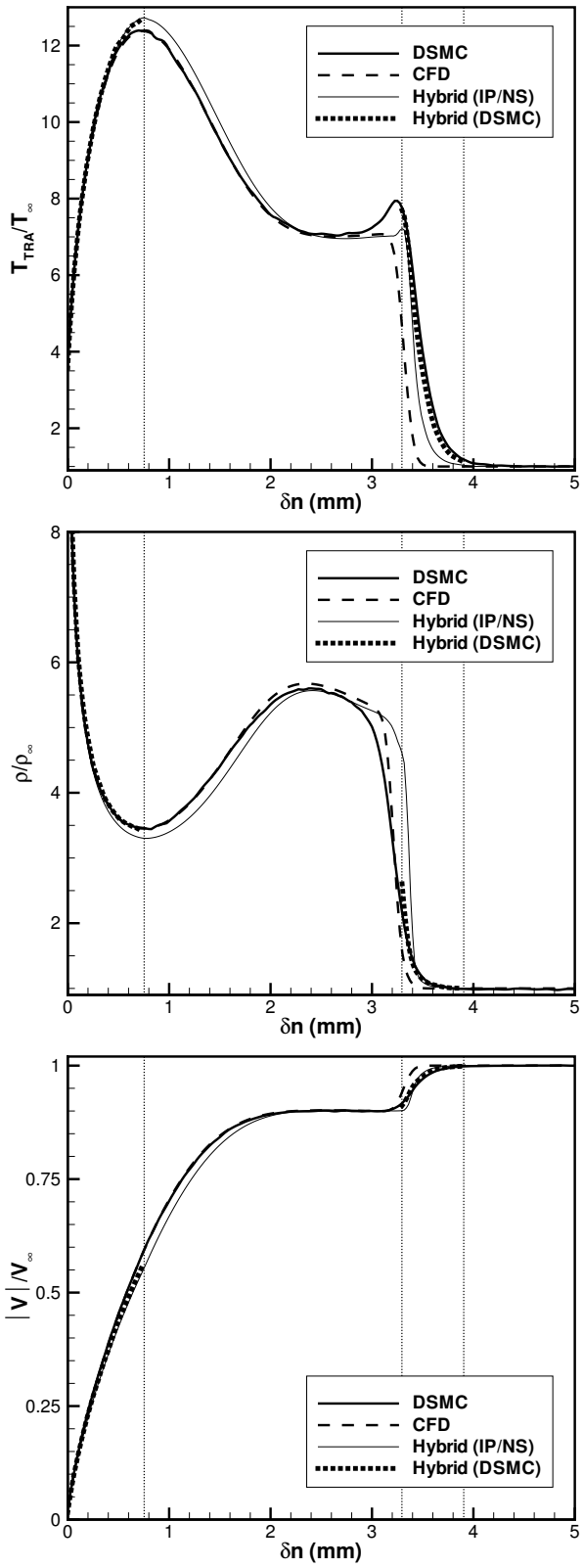

Figure 6.9: Comparisons for profiles along the line normal to the cone at $x = 4$ cm when 10 layers of buffer cells are employed.

6.1.3 Results Obtained With 6 Layers of Buffer Cells and $\mathbf{Kn_{max} = 0.005}$

The other way of increasing the area of the particle domain is by setting a smaller breakdown cut-off value. If the cut-off value is set to 0.005 and 6 layers of buffer cells are employed, the hybrid results are in excellent agreement with the DSMC results. In Figures 6.10 to 6.12, excellent agreement is shown between the hybrid-DSMC and pure DSMC results in both the shock region and the region close to the wall. The price for obtaining the encouraging hybrid results, however, is that about 55.3% (99,505) of the total number of cells are in the particle domain after one million hybrid simulation steps and the simulation takes about 190 hours on the 1-GHz Intel Linux cluster.

The temperature profiles in Figures 6.10 to 6.12 exhibit the poor prediction of the DSMC-IP method in strong nonequilibrium regions. This is another issue that must be improved in the future.

A pure DSMC-IP simulation can be viewed as that obtained with the cut-off value for the breakdown parameter equal to 0 and all cells are in the particle domain. Results similar to the profiles in Figure 6.10 to 6.12 are then expected.

6.1.4 Computational Cost

Details of the computational costs of different numerical methods executed on an Intel Linux cluster with 20 1-GHz processors under various setups are provided in Table 6.1 for comparison. The number of particles includes particles in both the particle and buffer cells. Considering the three hybrid simulations, it is clear that a simulation takes a longer time to run if it has a larger number of particles and more cells with particles.

The per particle cost in the table is defined as the time (in minutes) required on

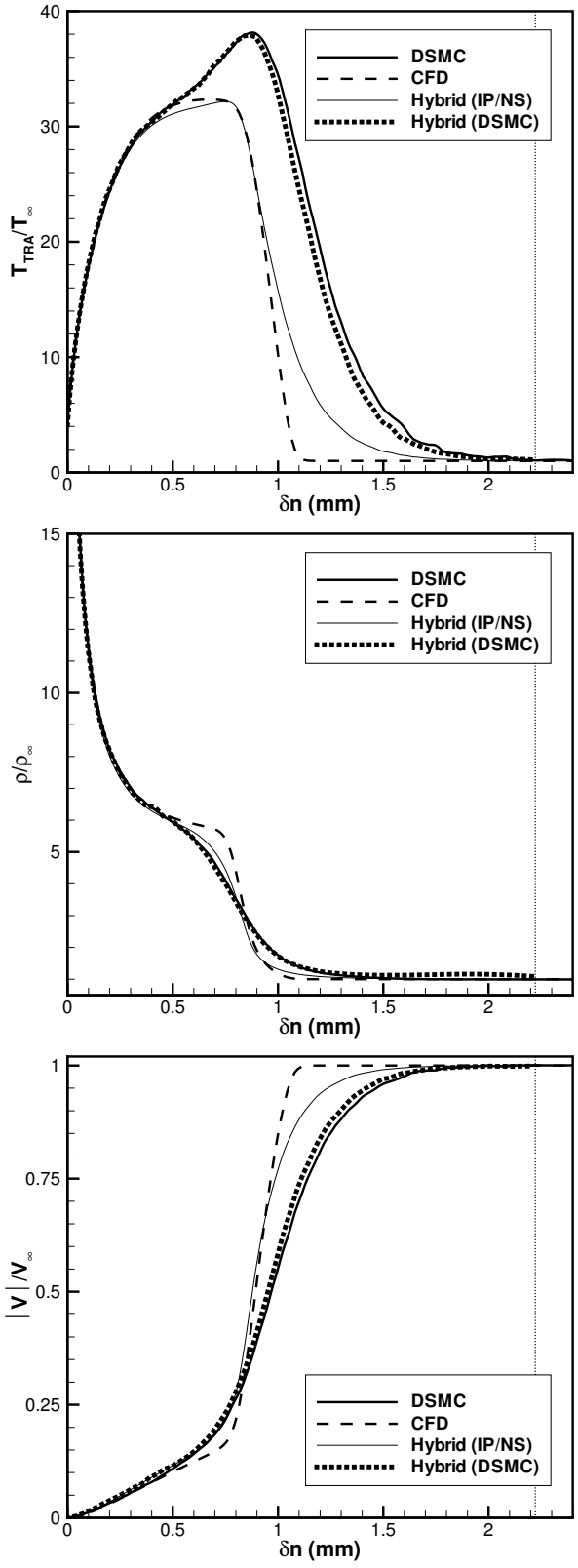

Figure 6.10: Comparisons for profiles along the stagnation line when 6 layers of buffer cells are employed and $\mathrm{Kn}_{\max} = 0.005$.

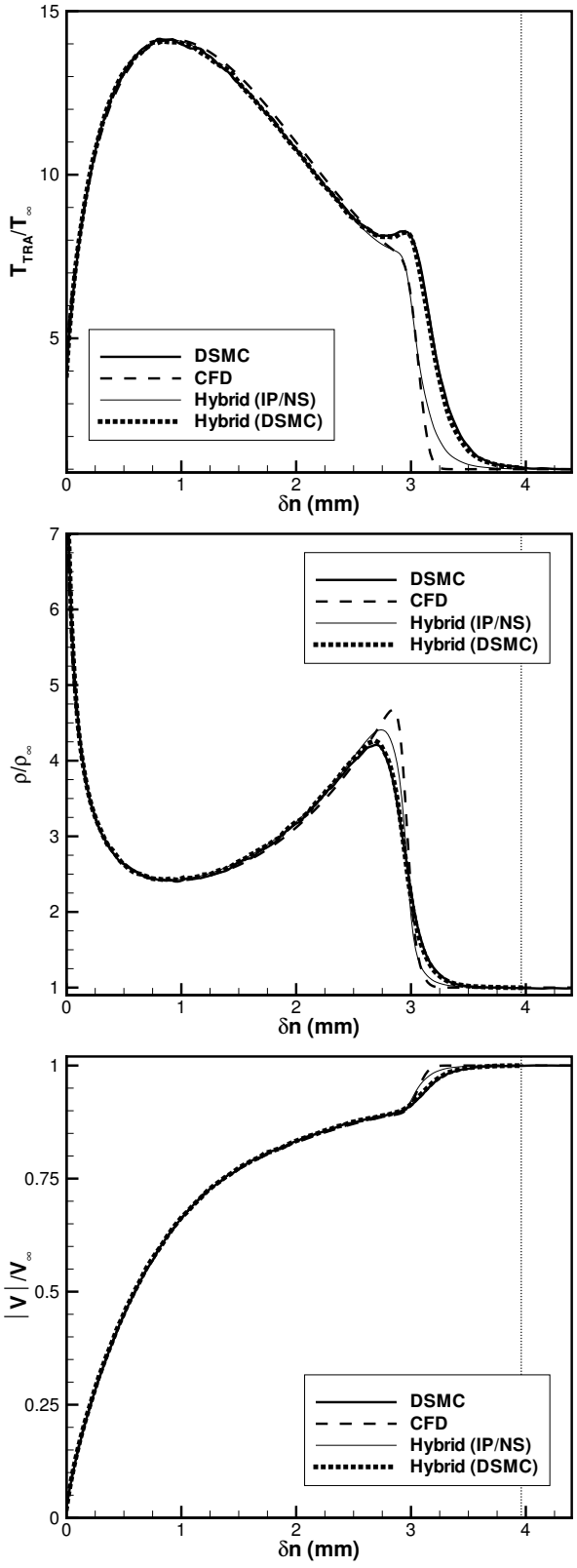

Figure 6.11: Comparisons for profiles along the line normal to the cone at $x = 2$ cm when 6 layers of buffer cells are employed and $\mathrm{Kn}_{\max} = 0.005$.

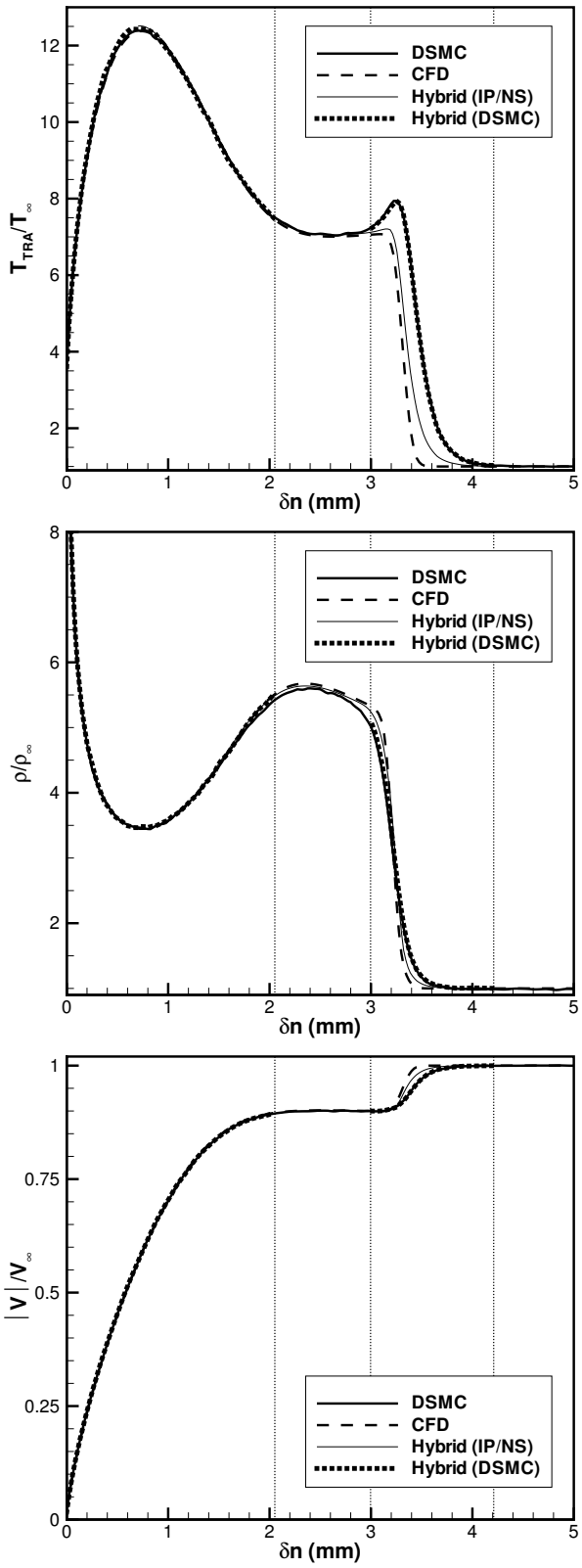

Figure 6.12: Comparisons for profiles along the line normal to the cone at $x = 4$ cm when 6 layers of buffer cells are employed and $\mathrm{Kn}_{\max} = 0.005$.

	CFD	Pure DSMC	Hybrid (6 Buffers)	Hybrid (10 Buffers)	Hybrid (6 Buffers & Kn=0.005)	Pure DSMC-IP
Number of Continuum Cells	180000	-	119949	122792	80495	-
Number of Particle Cells	-	180000	60051	57208	99505	180000
Number of Buffer Cells	-	0	12624	18696	7931	0
Percentage of Particle & Buffer Cells (%)	-	100	40.4	42.2	59.7	100
Particles (million)	-	5.9	3.9	4.0	5.6	9.1
Steps (thousand)	20	200	1000	1000	1000	1000
Time (hour)	0.75	32	130	152	190	260
Per Particle Cost (min/Ks/Mp)	-	1.63	2.00	2.28	2.04	1.71
Per Cell Cost (sec/Ks/Kc)	0.75	3.20	2.60	3.04	3.80	5.20

Table 6.1: Computational costs on an Intel Linux cluster with 20 1-GHz processors of different numerical methods under various setups for a Mach 12.6 nitrogen flow over a 25° blunted cone tip.

the specific Linux cluster for every thousand steps (Ks) and every million simulated particles (Mp). It is very disappointing to find out that the hybrid approach is at least about 23% slower than the pure DSMC method to advance a certain number of steps if the numbers of particles employed in the two methods are identical. The per particle cost of the hybrid approach is even worse than the pure DSMC-IP method by at least 17%.

The per cell cost in Table 6.1 is defined as the time (in seconds) required on the Linux cluster for every thousand steps (Ks) and every thousand computational cells (Kc). From the point of the per cell cost, the CFD method is not overwhelmingly superior over the DSMC method as the latter is slower than the former by no more than a factor of about 4.3.

The per cell cost of the three hybrid simulations increases as the number of simulated particles or the percentage of the particle and buffer cells is increased. Compared to the per cell cost of the pure DSMC simulation, two of the hybrid simulations with $\mathrm{Kn}_{\max}$ equal to 0.03 have lower cost while the third one has a 19% higher cost.

It is easy to make a connection between the per cell cost of the hybrid simulations and Figure 5.2. For instance, the percentage of the particle and buffer cells is about 40% for the hybrid simulation with 6 layers of buffer cells and $\mathrm{Kn}_{\max}$ equal to 0.03 and the time usages by the DSMC and IP methods are 48% and 25% from Figure 5.2 for the case of 50 particles per cell. The time consumed by the particle methods for every thousand steps and every thousand cells is about 1.9 seconds ($2.6 \times 0.48 + 2.6 \times 0.25$). Similarly, the percentage of the particle and buffer cells is about 60% for the hybrid simulation with 6 layers of buffer cells and $\mathrm{Kn}_{\max}$ equal to 0.005 and the time usages by the DSMC and IP methods for 50 particles per cell are 51% and 28%. The time

spent by the particle methods for every thousand steps and every thousand cells is about 3.0 seconds ($3.8 \times 0.51 + 3.8 \times 0.28$). The ratio of the time required by the particle methods in the two cases is $3.0/1.9 = 1.58$, which is very close to the ratio of the number of particles $5.6/3.9 = 1.44$.

The pure DSMC and DSMC-IP simulations have very close per particle costs but quite different per cell costs. This is because there are about 30 particles per cell in the pure DSMC simulation whereas there are about 50 particles per cell in the pure DSMC-IP simulation. If the average number of particles per cell in the pure DSMC-IP simulation is reduced to 30, the per cell cost of the simulation will be very close to 3.2.

It is not clear whether the current hybrid approach is more numerically efficient or less than the DSMC method because the information indicated by the particle and cell costs is mixed. Although the hybrid approach has a higher per particle cost in the blunted cone flow, it should not be concluded that the hybrid approach will also have a higher per particle cost in other flows. The example in the next section will show the exact opposite trend. A possible explanation for the higher per particle cost of the hybrid approach in this particular case is due to a higher cost of interprocessor communication overhead. This issue is related to both the programming algorithm for the interprocessor communication and the hardware architecture of the parallel machine performing the hybrid simulations and is beyond the scope of the present research.

6.2 Hollow Cylinder/Flare

The hybrid simulation for the hollow cylinder/flare is started by obtaining a steady state CFD solution. The CFD solution [62] is obtained on a structured grid

consisting of 2048 cells along the surface and 512 cells normal to the surface. The steady state CFD solution is then mapped onto the 1000 by 200 structured grid shown in Figure 3.14 by interpolation for initializing the hybrid simulation. In each hybrid simulation considered below, the size of the particle domain is updated every 100,000 time steps.

6.2.1 Results Obtained With 6 Layers of Buffer Cells

In the first hybrid calculation for the hollow cylinder/flare, 6 layers of buffer cells are employed and the time step is 2.5×10^{-10} sec. A total number of 5 million steps is computed after the domain is initialized with the CFD solution and the last 60,000 steps are sampled once for every three steps. At the beginning of the hybrid simulation, about 37.9% (75,854) of the total number of cells are in the particle domain and at the end of the simulation, about 38.2% (76,496) are in the particle domain. Although the number of the particle cells does not change too much, the area that they occupy does alter significantly.

The transition of the particle domain from the beginning to the end of the hybrid simulation is shown as the gray regions in Figure 6.13. A large portion of the particle domain is above the cylinder, where low density is encountered. The other portion of the particle domain is primarily along the oblique shock wave from the leading edge, the detached bow shock, and the flare body surface. Notice that there is a large continuum domain near the conjunction of the cylinder and flare as the hybrid simulation is started and it gradually vanishes after about 3.1 millon time steps.

At the beginning of the hybrid simulation, there is a very narrow particle region coming out from the main body of the particle domain and merging into the oblique shock region. The narrow particle region is caused by a strong density gradient in the

CFD solution (shown below). The narrow particle region moves in the downstream direction with time and eventually settles down and joins with the oblique and bow shock waves to form a fork point.

The hybrid simulation is performed on an Intel Linux cluster with 40 2.4-GHz processors connected with a high-bandwidth Myrinet network. There are about 80 particles in each particle cell. The run time is about 590 hours – more than 24 days!

Flow Fields

Comparisons of the translational temperature and density contours obtained with pure DSMC and the hybrid method are shown in Figures 6.14. Although it is very encouraging that the two solutions are in fair agreement under such complex circumstance, discrepancies between them can be easily found, especially around the conjunction of the cylinder and flare. Notice that the oblique shock starting from the sharp leading edge of the cylinder reaches the flare at a slightly different location in the two solutions. A thicker detached bow shock is predicted in the hybrid solution. As a result, the flow behind the bow shock is not exactly the same in the two simulations.

Surface Properties

In Figures 6.15(a) and 6.15(b), numerical results are compared with the experimental data from Holden [50] for pressure and heat transfer coefficients along the body surface. The hybrid-DSMC and hybrid-IP results are almost identical along the surface. Generally speaking, the hybrid results are in good agreement with DSMC and experimental results from the leading edge up until about $x/L = 0.8$. The most interesting point to emphasize is that the size of the separation zone is reduced from the initial size predicted by CFD to about the size measured in the experiment. This

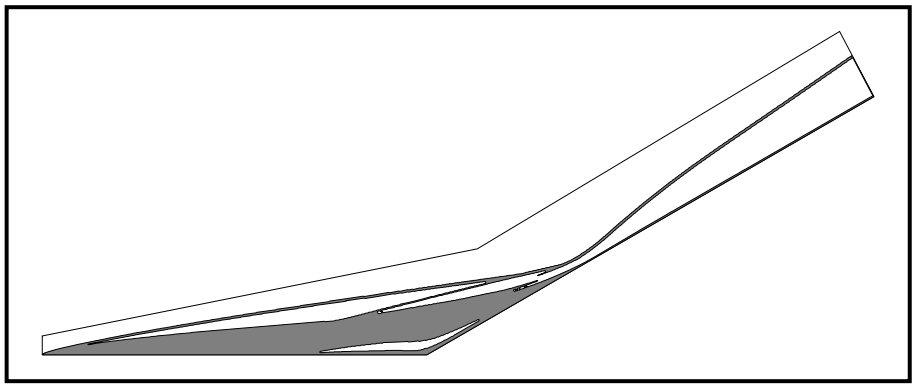

(a) Beginning of the hybrid simulation.

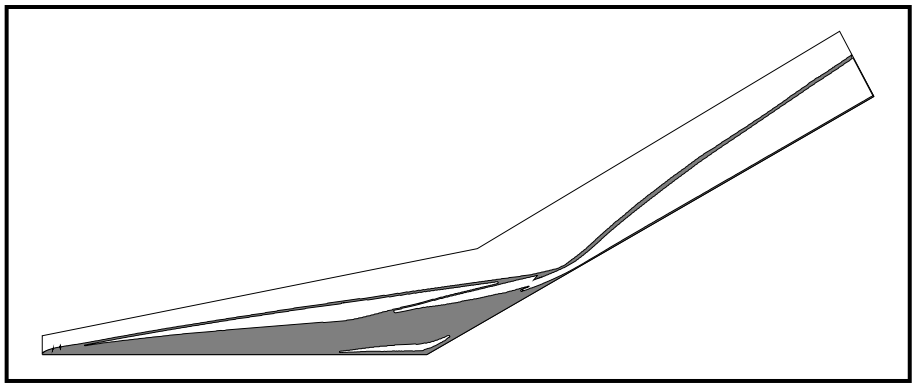

(b) 500,000 steps after the hybrid simulation.

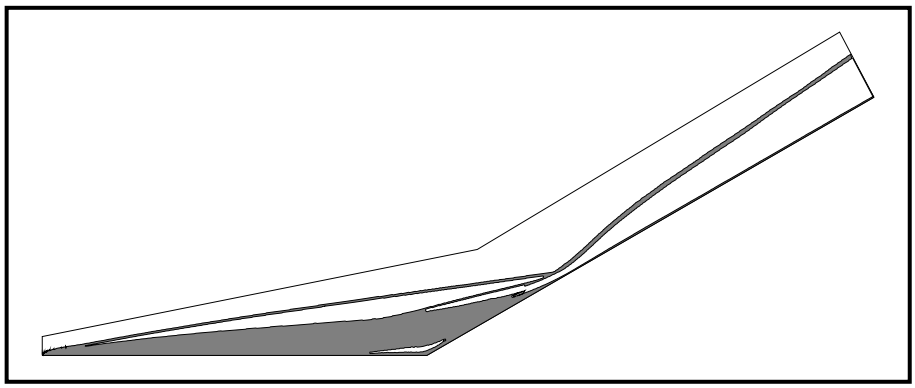

(c) 1 million steps after the hybrid simulation.

Figure 6.13: Particle domain in the hybrid simulation for the flow over a hollow cylinder/flare. (continued)

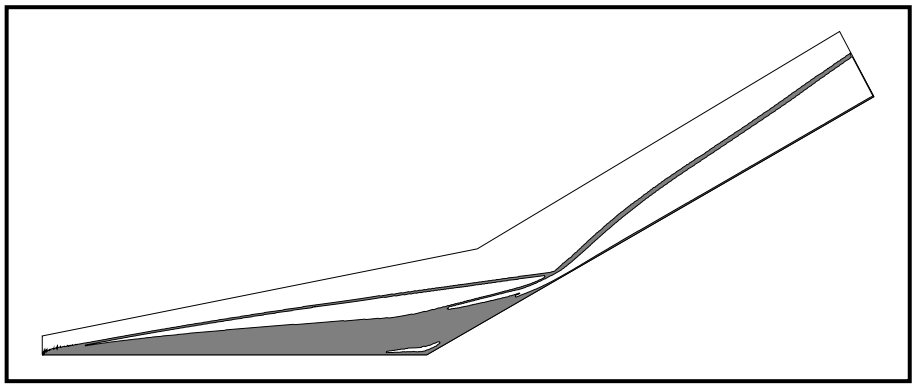

(d) 1.5 million steps after the hybrid simulation.

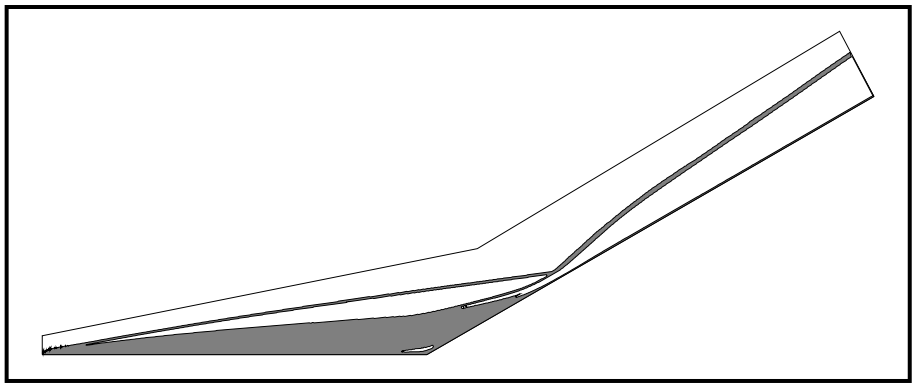

(e) 2.0 million steps after the hybrid simulation.

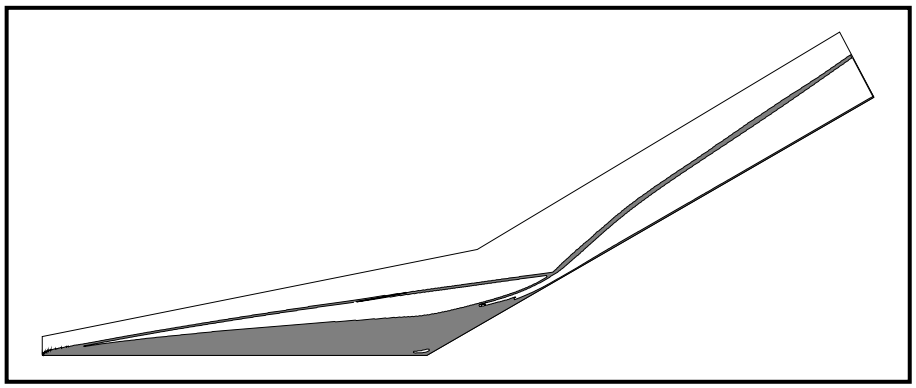

(f) 2.5 million steps after the hybrid simulation.

Figure 6.13: Particle domain in the hybrid simulation for the flow over a hollow cylinder/flare. (continued)

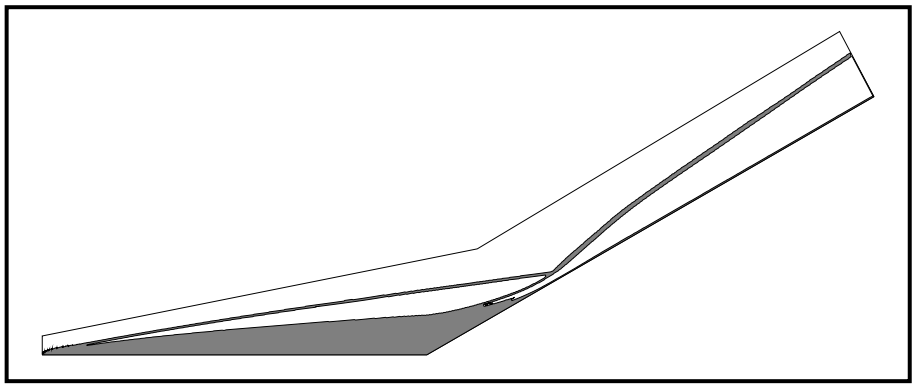

(g) 3.1 million steps after the hybrid simulation.

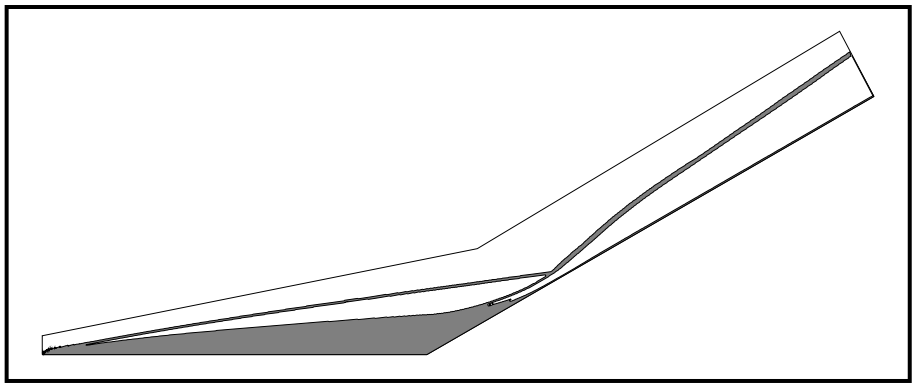

(h) 4.0 million steps after the hybrid simulation.

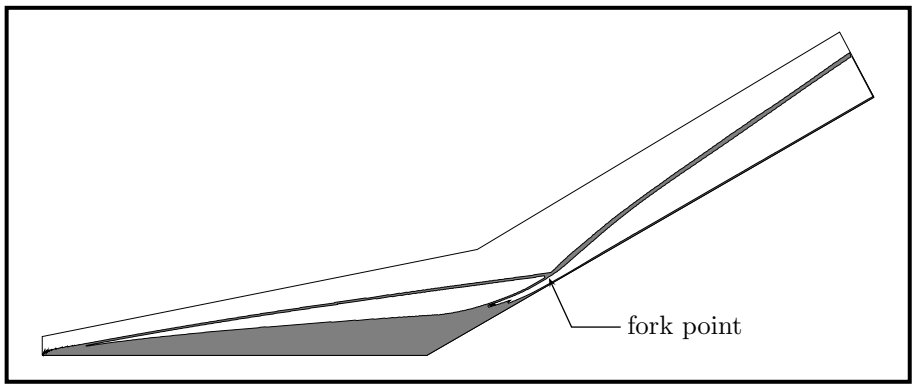

(i) 5.0 million steps after the hybrid simulation.

Figure 6.13: Particle domain in the hybrid simulation for the flow over a hollow cylinder/flare.

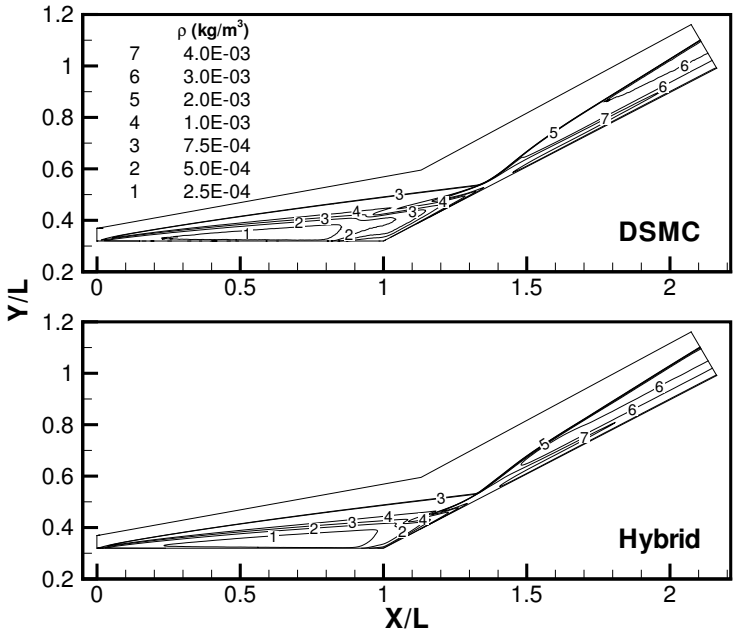

(a) Comparison of mass density.

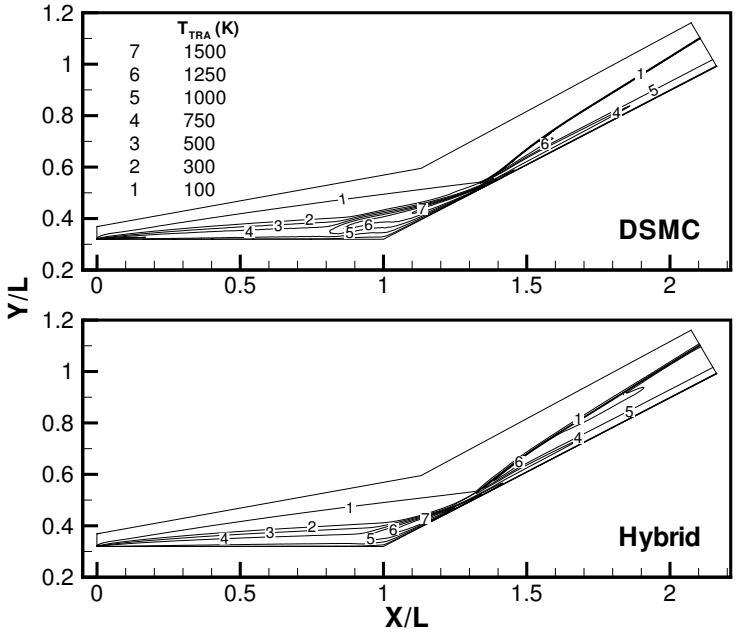

(b) Comparison of translational temperature.

Figure 6.14: Comparison for mass density and translational temperature of DSMC simulation and hybrid simulation with 6 layers of buffer cells for the flow over a hollow cylinder/flare.

indicates that the hybrid approach is successful at a certain level.

As pointed out previously, the oblique shock strikes the flare at a different location in the hybrid solution, resulting in a different location for the peaks of the surface pressure and heat transfer coefficients. The heat transfer rate behind the peak is over-predicted by the hybrid approach while DSMC and CFD both provide good agreement with the measured data.

Skin friction coefficients calculated with the different numerical methods are compared in Figure 6.16. It is evident that the sizes of the separation zone predicted by them differ to a large extent.

Detailed Comparisons

Detailed comparisons of the pure DSMC, CFD, and hybrid solutions are first made along the line normal to the cylinder surface at $x/L = 0.01$, as displayed in Figure 6.17. The comparisons all show that the hybrid-DSMC results are in outstanding agreement with the pure DSMC results. Notice that DSMC predicts a temperature ratio T/T_∞ equal to about 12 at the wall while the wall boundary condition and freestream temperatures give a ratio of 3.11, indicating a large temperature jump at the wall and very strong translational nonequilibrium near the leading edge. Neither the slip model nor the DSMC-IP method makes a correct prediction of the slip temperature at the wall. Substantial discrepancies between the DSMC/hybrid-DSMC and CFD/hybrid-IP temperatures are a result of the nonequilibrium. On the other hand, the DSMC-IP scheme predicts an accurate velocity jump at the wall.

Next, the flow field around the middle of the cylinder is studied. In Figure 6.18, profiles are shown of comparisons for the flow properties along the line normal to the cylinder body at $x/L = 0.5$. At this station, the whole computational domain is

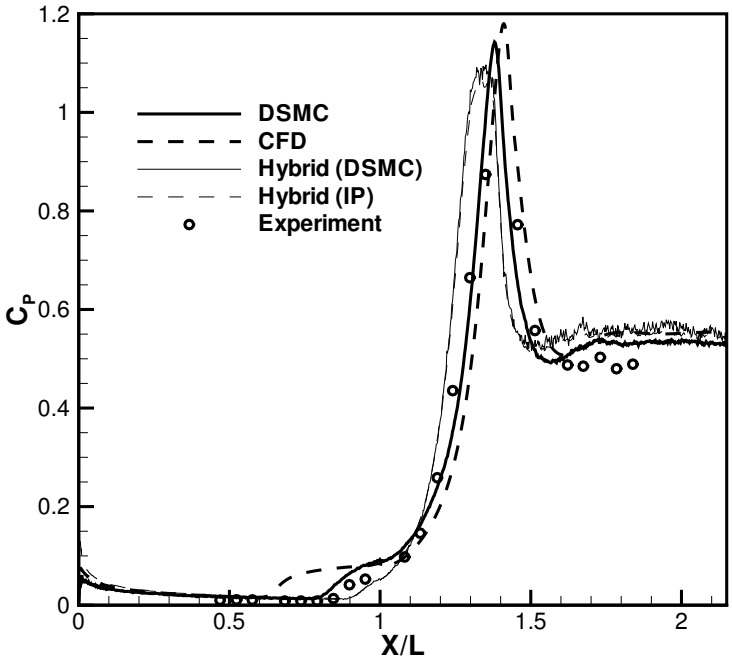

(a) Comparison of surface pressure.

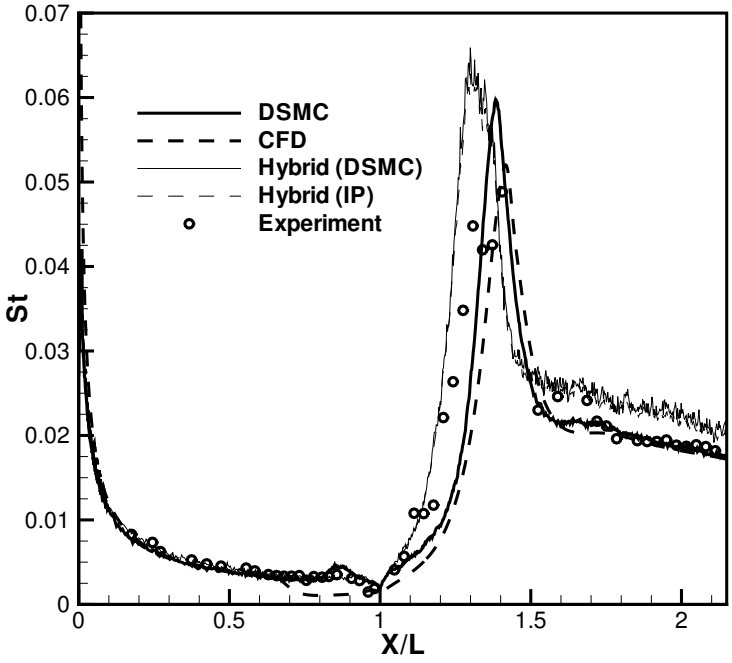

(b) Comparison of surface heat transfer rate.

Figure 6.15: Comparison of surface properties with different numerical methods and experimental data for the flow over a hollow cylinder/flare.

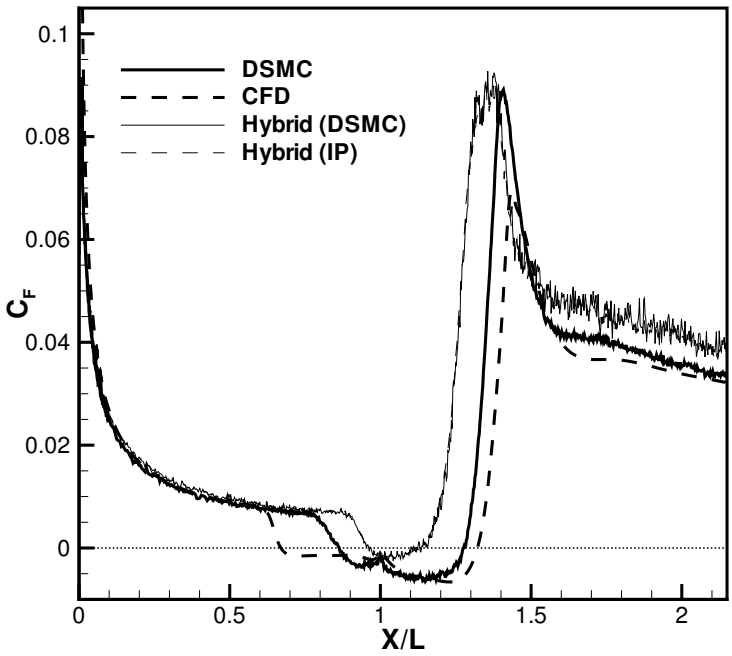

Figure 6.16: Comparison of skin friction coefficients with different numerical methods for the flow over a hollow cylinder/flare.

divided into four sub-domains along the δn direction and hybrid-DSMC information is absent in the continuum domains. In the particle domain next to the body, the hybrid-DSMC results again are predicted excellently by the hybrid approach. The density profiles indicate that the density is as low as 30-40% of the freestream density at about $\delta n = 2$ mm. This can also be observed in Figure 6.14(a).

In the shock region, the hybrid-DSMC and hybrid-IP results are shown to move from the initial CFD conditions towards the DSMC solutions. This suggests that 6 layers of buffer cells are sufficient to handle such an oblique shock very well.

Because the nonequilibrium effect becomes relatively weak at this station, the hybrid-IP and DSMC results are very close in most of the region. The slip velocity and temperature predicted by the CFD slip models are accurate, based on comparisons to the DSMC velocity and temperature.

Further downstream at the conjunction of the cylinder and flare ($x/L = 1$),

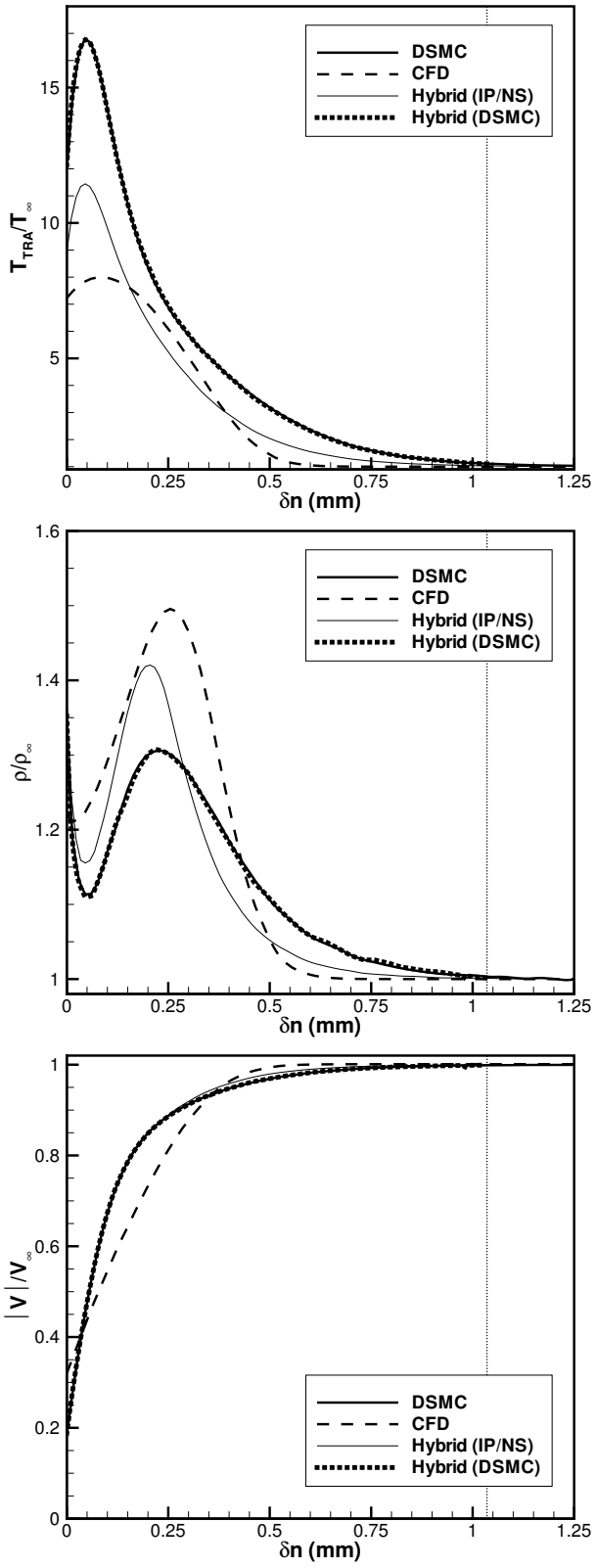

Figure 6.17: Comparisons for profiles along the line normal to the cylinder at $x/L = 0.01$ when 6 layers of buffer cells are employed.

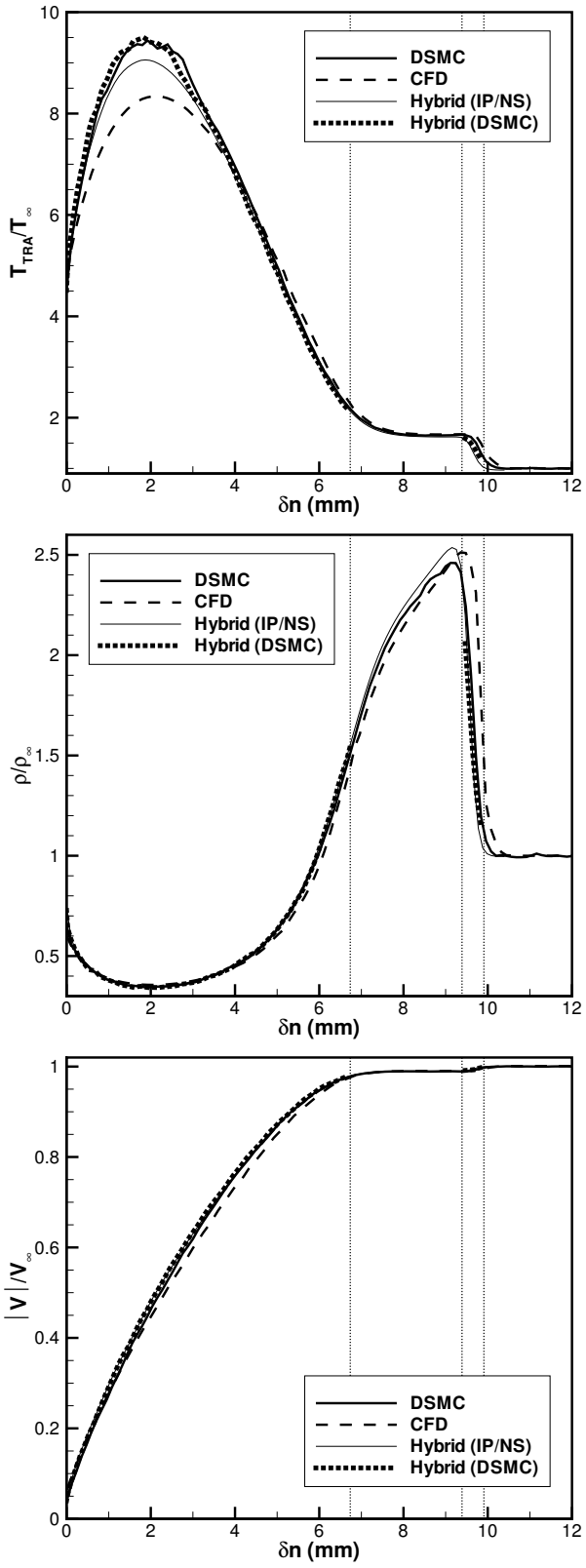

Figure 6.18: Comparisons for profiles along the line normal to the cylinder at $x/L = 0.5$ when 6 layers of buffer cells are employed.

profiles along a vertical line are plotted in Figure 6.19 for comparison. The hybrid approach does not work so well at this station. Velocity profiles show that the sizes of the separation zone calculated by the various numerical methods are different. Notice the strong density gradient in the CFD solution in the continuum domain from $\delta n = 10.4$ to 16.9 mm. This strong density gradient results in the narrow particle domain at the beginning of the hybrid simulation in Figure 6.13(a). Ideally, this narrow particle domain should move to about $\delta n = 11$ mm as indicated in the DSMC density profile, but it vanishes in the hybrid simulation because of a locally flat NS density.

The ratio of the wall temperature predicted with the hybrid approach is very close to 3.11 and there is no slip velocity observed. These two aspects combined imply that the translational nonequilibrium effect has become very weak at this station. The densities on the wall predicted with the hybrid approach are much lower than the DSMC result.

The whole computational domain is divided into six regions along the line normal to the flare at $x/L = 1.3$, as displayed in Figure 6.20. It is found in Figure 6.14 that this station is right ahead of the fork point mentioned above. The particle region near the wall is very small and is only about 0.29 mm in width. The small shock region predicted by the hybrid approach is at about from $\delta = 3.9$ to 4.2 mm and the initial CFD shock region is at about from $\delta = 5$ to 6 mm. The DSMC shock is in between the two CFD and hybrid shocks. It is concluded that the hybrid approach does not successfully handle such a flow because it fails to change the shock wave from the position initialied with the CFD solution to the correct position predicted by DSMC.

The third particle region is from $\delta = 1.8$ to 2.1 mm. The hybrid-IP/NS density

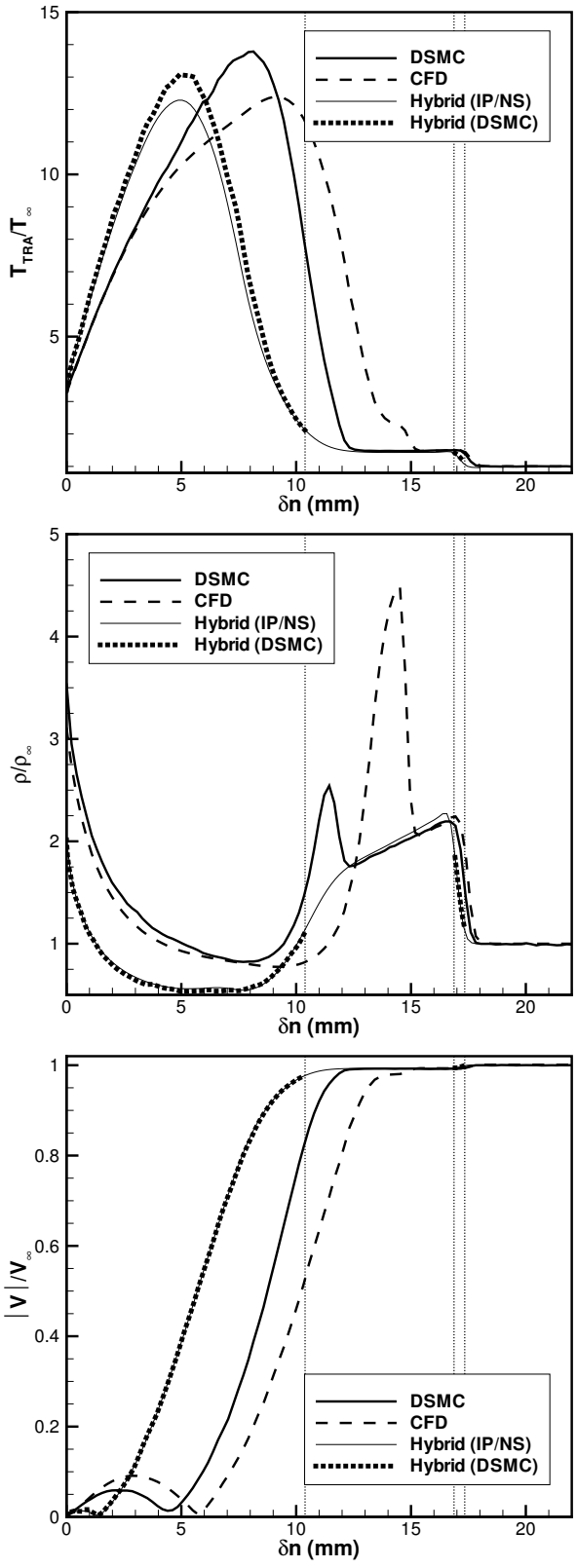

Figure 6.19: Comparisons for profiles along the line normal to the cylinder at $x/L = 1$ when 6 layers of buffer cells are employed.

profile at $\delta = 1.8$ mm indicates a wrong domain interface placing as the gradient is large but the Knudsen number evaluated in terms of density is lower than the breakdown cut-off value.

When a line normal to the flare is considered behind the fork point at $x/L = 1.6$, the whole computational domain is again divided into four regions. The flow property profiles from various numerical methods are plotted in Figure 6.21 for comparison. It is worth pointing out that the hybrid results are in good agreement with the DSMC results in the very narrow particle region near the wall.

The shock position in the hybrid simulation moves from the initial CFD shock position, beyond the DSMC shock position, and further toward the freestream direction. This suggests that the shock angles calculated with the three numerical methods are not the same as each other. It is difficult at this point for the current hybrid approach to work under such a circumstance.

Inappropriate placing of the domain interface is again detected at the interface of $\delta = 7.3$ mm where temperature, density, and velocity gradients are all significant. At this interface, discrepancies between the hybrid-DSMC and hybrid-IP/NS information are found due to the absence of the buffer cell information, as explained in Section 5.5.

6.2.2 Results Obtained With 10 Layers of Buffer Cells

To investigate the influence of the number of layers of buffer cells on the hybrid simulation, 10 layers of buffer cells are employed in the hybrid simulation. Since the computation is expected to be more expensive than the one with 6 layers of buffer cells, the new hybrid simulation is not initialized with the steady state CFD solution. Instead, the new simulation is started with the results after 4.5 million steps in the

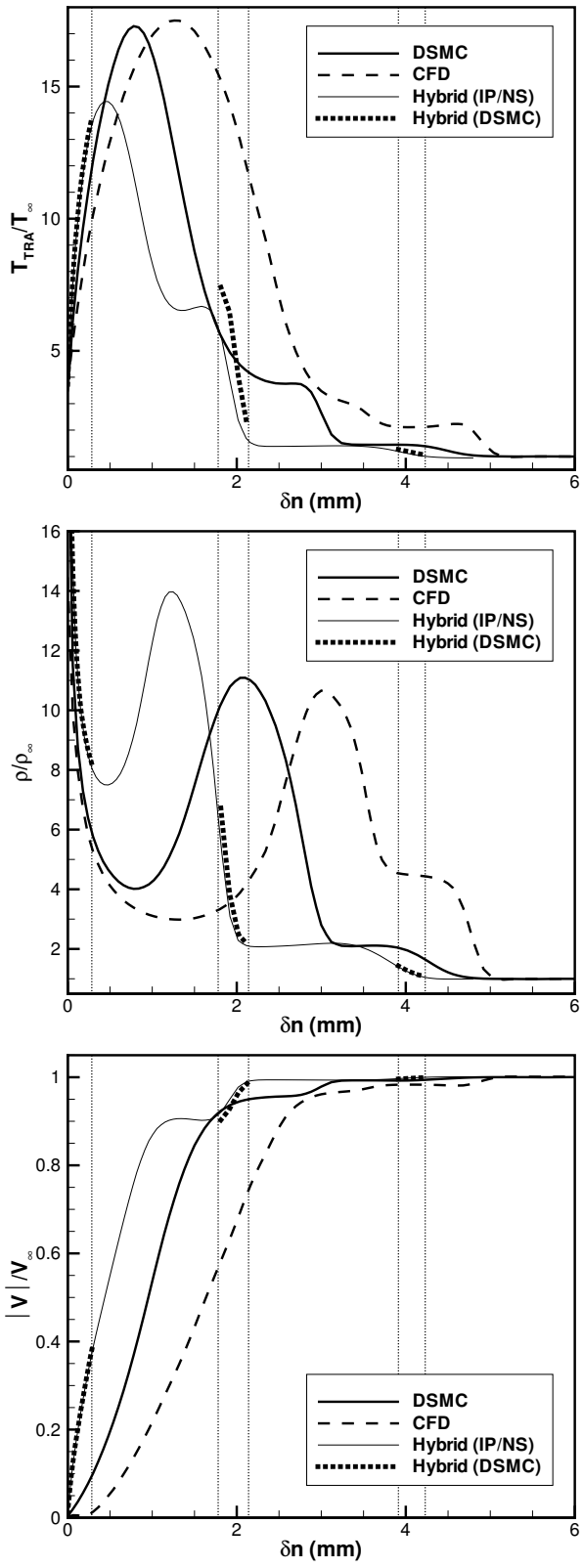

Figure 6.20: Comparisons for profiles along the line normal to the flare at $x/L = 1.3$ when 6 layers of buffer cells are employed.

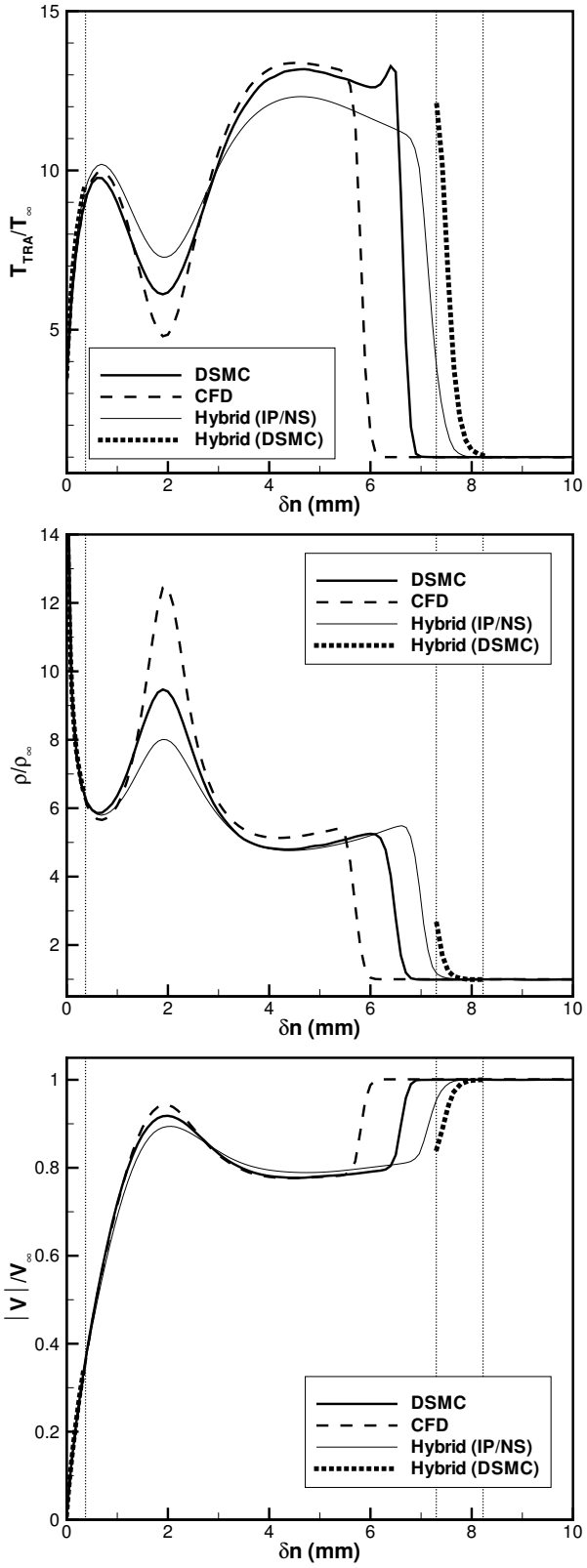

Figure 6.21: Comparisons for profiles along the line normal to the flare at $x/L = 1.6$ when 6 layers of buffer cells are employed.

last section and carried out for another 500,000 steps. The total number of time steps, therefore, is 5 million that is the same as in the last section.

The flow property profiles extracted from various lines normal to the body are displayed in Figures 6.22 to 6.26. In general, good agreement between the hybrid-DSMC and pure DSMC results can be found at $x/L = 0.01$ and 0.5 in both boundary and shock regions and poor agreement at $x/L = 1$ and 1.3. In Figure 6.26, the new results at $x/L = 1.6$ exhibit the same characteristics as in Figure 6.21: the hybrid and pure DSMC results in the narrow particle region near the wall are in good agreement, the hybrid shock is the one furthest away from the body, and the hybrid solution in the shock region does not agree with the pure DSMC solution to a large extent.

6.2.3 Discussion

There are several possible reasons to cause the poor prediction at $x/L = 1, 1.3$ and 1.6. Perhaps The size of the particle domains is too small. The number of layers of the buffer cells may be too small. The time step employed in the hybrid simulations may be too large. The collision models in the DSMC-IP technique may be inadequate. Rotational nonequilibrium is not taken into account in the hybrid approach.

Among the listed reasons, the factor of time step can be ruled out because the time steps in the hybrid simulations are an order of magnitude smaller than in the pure DSMC simulation. Another factor that can be eliminated is the ignored rotational nonequilibrium in the present hybrid approach. An observation of the temperature profiles in Figures 6.17 to 6.21 or in Figures 6.22 to 6.26 shows that the highest temperature ratio T/T_∞ is about 17 at $x/L = 0.01$ and 1.3. This temperature ratio

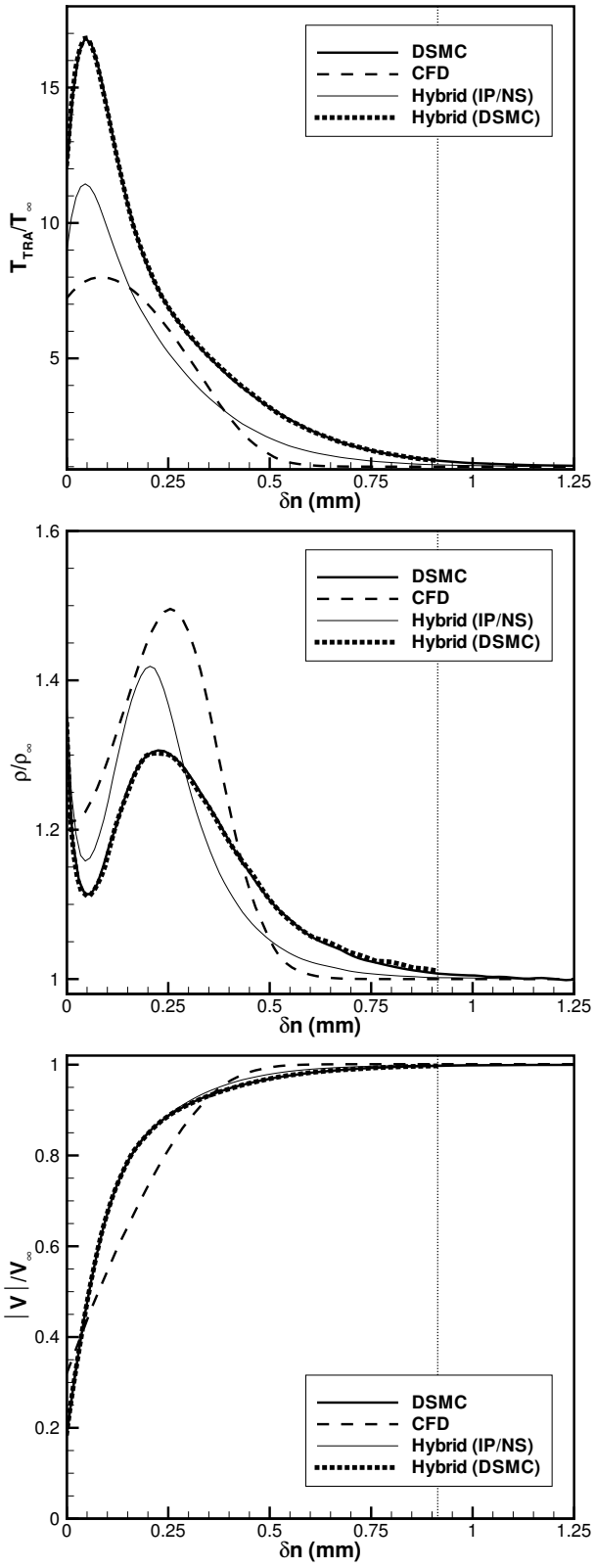

Figure 6.22: Comparisons for profiles along the line normal to the cylinder at $x/L = 0.01$ when 10 layers of buffer cells are employed.

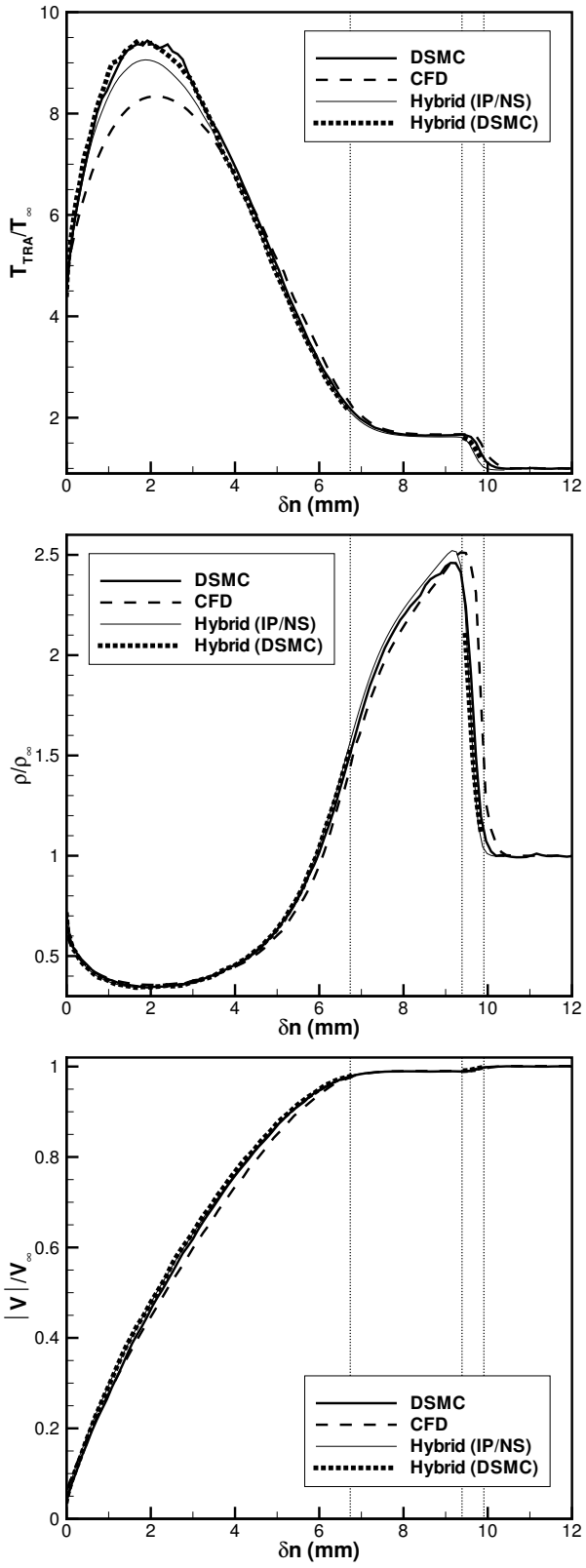

Figure 6.23: Comparisons for profiles along the line normal to the cylinder at $x/L = 0.5$ when 10 layers of buffer cells are employed.

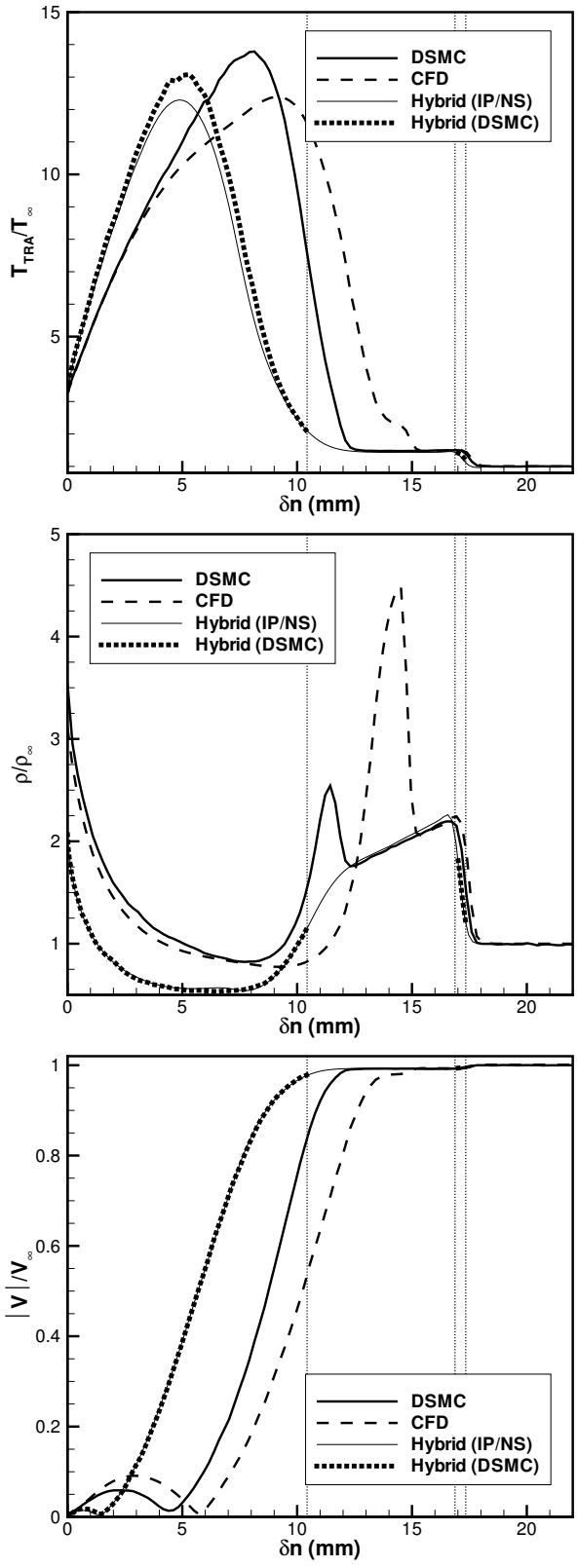

Figure 6.24: Comparisons for profiles along the line normal to the cylinder at $x/L = 1$ when 10 layers of buffer cells are employed.

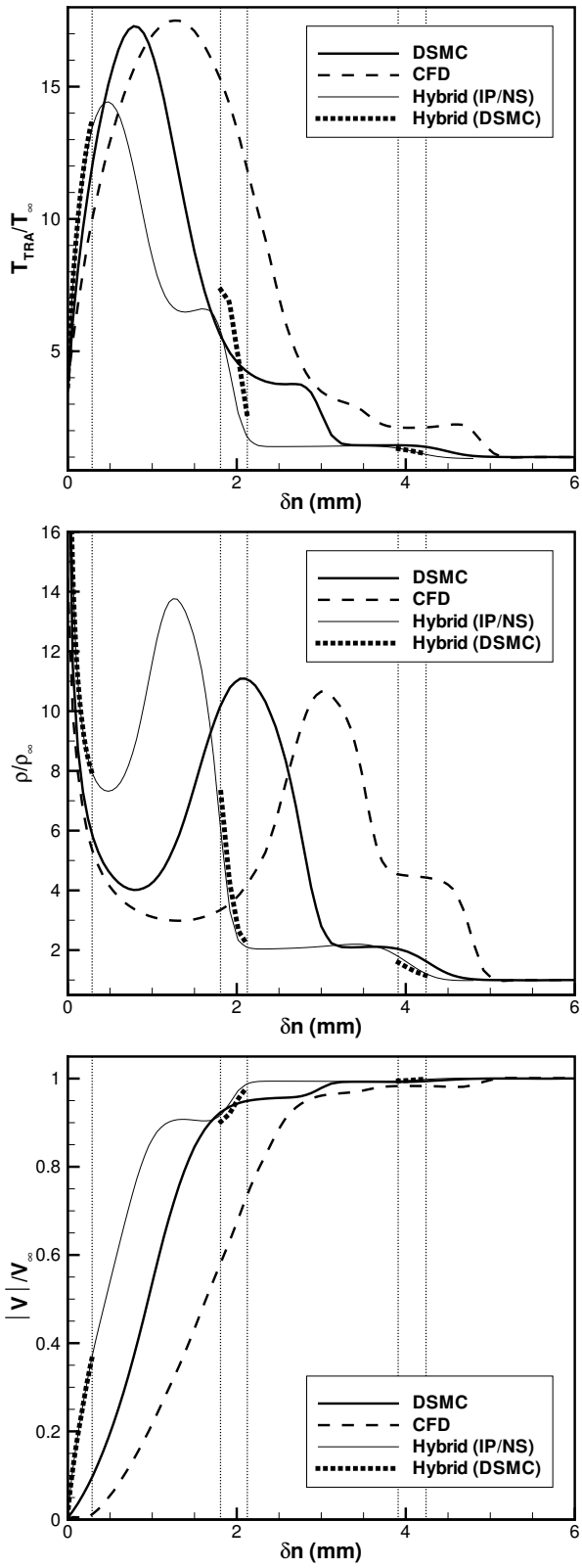

Figure 6.25: Comparisons for profiles along the line normal to the flare at $x/L = 1.3$ when 10 layers of buffer cells are employed.

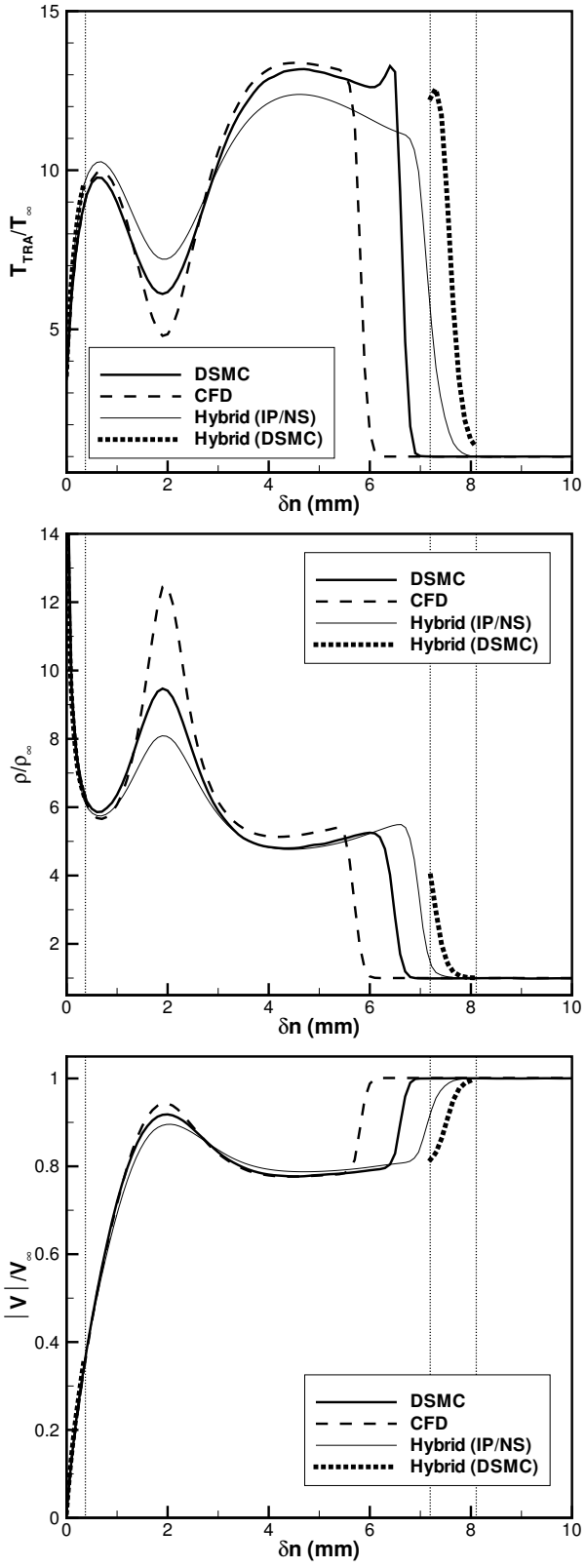

Figure 6.26: Comparisons for profiles along the line normal to the flare at $x/L = 1.6$ when 10 layers of buffer cells are employed.

corresponds to a temperature at about 1,624 K. At this temperature, the collision frequency involving the exchange of both translational and rotational energies is insignificant and the two energy modes are nearly equilibrium. In addition, it is evident that the hybrid-DSMC temperature is well predicted at $x/L = 0.01$.

The numerical experiments performed by Sun and Boyd [78] for verifying the IP technique and determining the C_μ and C_κ values in the collision models involved very simple flows, such as Couette flows, thermal Couette flows, Rayleigh flows, and NACA0012 airfoil flows. Most of these flows share one common feature: the main stream flows in a single direction. It is unclear whether the IP technique and collision models are adequate for the present flows with large areas of circulation, such as the separation zone at the conjunction of the cylinder and flare. A lid-driven cavity flow could be a good test in the future.

The poor prediction in the shock regions at $x/L = 1.3$ and 1.6 is very probably the result of the inappropriate domain interface location determined with the continuum breakdown parameter $\mathrm{Kn}_{\max}$. As pointed out previously, the breakdown parameter in the shock regions tends to place the continuum/particle domain interface at the location with large flow gradients, leading to a much smaller particle domain. A particle domain that is too small makes the hybrid approach work poorly, especially when the initial shock angle predicted by CFD is so different from the final shock angle predicted by DSMC.

In the hollow cylinder/flare flow, the results obtained with 6 layers of buffer cells differ only slightly from the results obtained with 10 layers of buffer cells. If the size of the particle domain is increased by decreasing the continuum breakdown cut-off value, for instance, 6 or 10 layers of the buffer cells are not expected to have a great influence on the physical accuracy. However, this requires more studies to be

confirmed.

6.2.4 Computational Cost

In Table 6.2, the computational costs of various numerical methods on an Intel Linux cluster with 40 2.4-GHz processors under different setups are listed. The number of particles is the summation of the numbers of particles in all particle and buffer cells. The time taken by the hybrid simulation with 10 layers of buffer cells is estimated by multiplying by 10 the time actually consumed for the last 500,000 time steps. Since neither of the hybrid simulations can be considered satisfactory in terms of accuracy and they spend at least twice the computational time of the pure DSMC simulation, the present hybrid approach is not regarded as successful for the specific flow over a hollow cylinder/flare.

The per particle and cell costs in the table have the same definition as in Table 6.1 in the last example. Unlike the last example, the current hybrid approach on the particular Linux cluster is at least 57% faster than the DSMC method in terms of the per particle cost. However, it is also inappropriate to conclude that the hybrid approach always has a lower per particle cost than the DSMC method because it is difficult to compare the interprocessor communication overhead between these two methods.

It is evident that the CFD method is overwhelmingly superior than the DSMC method in terms of the per cell cost. This is primarily because there is a significant number of particles in the DSMC simulation and the busy communication between the processors slows down the numerical performance. This is in part because the CFD solution [62] is obtained with an implicit scheme that is faster than the one employed in the blunted cone flow. However, based on the comparisons of the surface

	CFD	Pure DSMC	Hybrid (6 Buffers)	Hybrid (10 Buffers)
Number of Continuum Cells	200000	-	123504	122921
Number of Particle Cells	-	200000	76496	77079
Number of Buffer Cells	-	0	16121	26149
Percentage of Particle & Buffer Cells (%)	-	100	47.8	51.6
Particles (million)	-	27.0	8.0	9.0
Steps (thousand)	38	300	5000	5000
Time (hour)	8*	280	590	630†
Per Particle Cost (min/Ks/Mp)	-	2.07	0.89	0.84
Per Cell Cost (sec/Ks/Kc)	0.72	16.8	2.12	2.27

*On a 2048 by 512 grid.

†Estimation.

Table 6.2: Computational costs on an Intel cluster with 40 2.4-GHz processors of different numerical methods and under various setups for a Mach 12.4 nitrogen flow over a hollow cylinder/flare.

flow properties from the CFD solution with the experimental data, it is clear that the accuracy of the solution has been sacrificed.

The per cell costs of the hybrid simulations look much better than that of the pure DSMC simulation. The primary reason is again due to the significant amount of simulated particles in the pure DSMC simulation.

CHAPTER VII

Summary and Conclusions

7.1 Summary

The main objective for developing a hybrid particle-continuum method is to create a faster and more accurate approach than other conventional means. A hybrid method for computing hypersonic, nonequilibrium flows in 2D/axisymmetric configurations has been described in the thesis. In the particle domain, the DSMC-IP technique was employed while in the continuum domain, a finite volume, second-order accurate, Steger-Warming flux vector splitting NS solver was utilized.

In this thesis, continuum breakdown in a flow is defined as when the continuum solution differs from the particle solution by at least 5%. Numerical investigations showed that a Knudsen-number-like parameter, $\mathrm{Kn}_{\mathrm{max}}$, can best predict the continuum breakdown in the flows of interest.

Buffer and reservoir cells were introduced in the continuum domain and work as an extension of the particle domain. At the end of the particle movement phase, particles in either particle or buffer cells are retained. All simulated particles in the reservoir cells are first deleted for each time step and re-generated based on the local cell values. The microscopic velocities for the newly generated particles are initialized to the Chapman-Enskog distribution using an acceptance-rejection scheme.

The macroscopic DSMC-IP information in particle cells was updated for each time step. Given the fact that the DSMC-IP information has much smaller statistical scatter, the particle cells adjacent to the domain interface were regarded as the ghost cells and the DSMC-IP information in them were used to evaluate the continuum fluxes. Therefore, coupling these two domains becomes straightforward. Information exchange on the domain interface was continuously carried out for each time step.

Numerical experiments of hypersonic flows over a blunted cone and a hollow cylinder/flare were conducted, with the use of the continuum-breakdown criterion $\mathrm{Kn}_{\max} = 0.03$ or 0.005 and 6 or 10 layers of buffer cells. The hybrid method was first initialized with a steady state CFD solution and then marched forward. The interface between the particle and continuum domains was updated periodically.

The flow surface properties, the pressure and heat transfer coefficients, along the body walls of the hybrid results were compared with other numerical results and experimental data. The flow field properties, including temperature, density, and velocity, along several lines normal to the bodies were extracted and detailed comparisons were made with the corresponding DSMC and CFD solutions.

7.2 Conclusions

For the blunted cone case, the hybrid approach is capable of simulating the flow quite well. When 10 layers of buffer cells and the breakdown criterion $\mathrm{Kn}_{\max} = 0.03$ were employed, or 6 layers of buffer cells and the breakdown criterion $\mathrm{Kn}_{\max} = 0.005$ were employed, the hybrid results were remarkably accurate, in comparison with the DSMC results. Since the latter hybrid setup required more time on computation, it is concluded that 10 layers of buffer cells and the breakdown criterion $\mathrm{Kn}_{\max} = 0.03$ is the best hybrid simulation setup for this specific flow.

For the hollow cylinder/flare case, the conclusions are mixed. On the positive side, the size of the separation zone in the hybrid simulation was reduced from that predicted by CFD to approximately that measured in the experiment. The flow field simulated by the hybrid method is accurate from the leading edge up to at least the middle of the cylinder, regardless of whether 6 or 10 layers of buffer cells were employed. On the negative side, the flow field simulated by the hybrid method does not agree with the DSMC results in most regions further downstream from the middle of the cylinder, even when 10 layers of buffer cells were employed. A possible reason for the disagreement is due to the poor prediction by the DSMC-IP method near the shock region, with the result that everything from there on is affected. The other reason is probably attributed to inappropriate domain interface location determined with the continuum breakdown parameter $\mathrm{Kn}_{\max}$.

The disappointing performance of the hybrid method in strong shock regions is primarily caused by the equilibrium assumption in the DSMC-IP technique to estimate the extra translational energy carried by a simulated particle moving from one cell to the other. The new energy flux model developed in Section 2.5 can relax this assumption and should be integrated with the hybrid method in the future. In addition, a new breakdown parameter is proposed in the next section.

The numerical efficiency of the current hybrid method is a serious concern. In the blunted cone case, the hybrid simulation under the best setup took more than four times longer than the pure DSMC simulation. In the hollow cylinder/flare case, the hybrid simulations took at least 24 days on a Linux cluster with 40 2.4-GHz processors. The main reason for the poor numerical performance is that the time step required in a typical hybrid simulation is always smaller than in the standard DSMC simulation, sometimes an order of magnitude smaller. For instance, the time steps

employed in the pure DSMC and hybrid simulations for the hollow cylinder/flare were 3 nsec and 0.25 nsec, respectively. This is in part because the CFD scheme is explicit in the hybrid approach. This is also in part because the time step required in a DSMC-IP simulation is smaller than in the pure DSMC simulation. For instance, the time steps employed in the pure DSMC and pure DSMC-IP simulations for the blunted cone tip were 2 nsec and 0.5 nsec, respectively. Additionally, the DSMC-IP method uses more memory than in the standard DSMC method. It is therefore concluded that the numerical efficiency of the hybrid method is far from satisfactory.

Overall, the hybrid approach described in this thesis is the only truely hybrid DSMC-CFD approach to date. It is robust, multi-dimensional, strongly coupled, parallelized, and able to simulate strongly nonequilibrium, hypersonic compressed flows. The main weakness of the hybrid approach is its poor numerical performance.

7.3 Future Work

The current DSMC/CFD hybrid approach can be considered as a solid platform for future development. Several aspects for short term and long term development are described as follows. Many of these ideas should be first performed for one-dimensional flows, for instance 1-D shock problems, and then implemented in the fully 2-D/axisymmetric version.

7.3.1 Distribution of Newly Generated Particles

The current hybrid approach uniformly and randomly places the newly generated particles in the reservoir cells. In the future, the particles should be placed along the density gradient direction to account for the non-uniformity of the particle distribution.

7.3.2 Continuum Breakdown

Due to the poor prediction in a shock wave region by the DSMC-IP method, consideration should be given to determining the domain interface based on the DSMC information instead of the DSMC-IP information. This may be a good idea because the DSMC information contains the detailed nonequilibrium information. From the point of view of a general rule for determining the domain interface, however, there are at least four reasons against this idea. (1) The DSMC information is not continuous at the domain interface. Evaluation of the continuum breakdown parameter at such locations becomes very unclear. (2) There is no DSMC information outside the particle domain. Therefore, evaluation of the continuum breakdown parameter is confined within the particle domain only. (3) A smooth DSMC solution is very difficult to obtain in low speed flow regions. A small perturbation in a certain flow property in a solution always leads to a locally significant gradient for that property and in turn increases the difficulty of determining the location of the domain interface. (4) In general, because it always takes many more sampling steps to obtain a smooth DSMC solution, the overall numerical efficiency of the hybrid approach will become poorer and poorer if such a rule is implemented.

As a result, it is necessary to depend on the NS-IP information for determining the location of the domain interface. Numerical experiments exhibit a fundamental flaw of the use of the local Knudsen number as the continuum breakdown parameter in certain large gradient regions. A simple solution to this problem is the introduction of a reference Knudsen number

$$\mathrm{Kn}_{\mathrm{ref}} = \frac{\lambda}{Q_{\mathrm{ref}}} \left| \nabla Q \right| .$$

The reference value is a constant and can be taken from the freestream conditions,

for instance. In this way, regions with larger gradients always have higher Knudsen numbers. It is required to re-evaluate the cut-off value before this parameter can be actually employed.

7.3.3 Boundary Conditions for the New Energy Flux Model

Probably the easiest boundary conditions for the new energy flux model are the slip boundary conditions in Equations (2.17) and (2.18). When a simulated particle strikes a diffuse wall, its IP velocity and temperature are updated to the local slip velocity and temperature. Because this is a continuum model being applied in a particle method, its feasibility is unknown.

A more complex idea is inspired by the fact that the velocity distribution of a gas molecule reflected from a diffuse wall is the standard Maxwellian in the directions tangential to the wall and is a biased Maxwellian in the direction normal to the wall. Using Equations (2.23) and (2.24), the velocity distribution of a reflected IP particle is biased and can be written as

$$f(c_n, c_t)\, dc_n dc_t = \frac{1}{\sqrt{2\pi RT_w}\, RT_w} c_n \exp\left(-\frac{c_n^2 + c_t^2}{2RT_w}\right) dc_n dc_t,$$

where c_n is the velocity component normal to the wall and c_t is the velocity component tangential to the wall. Therefore, there are biased Maxwellian particles in the IP method in addition to the standard Maxwellian particles. The drawback of this idea is that the flux evaluation in Equation (2.41) becomes more complex, especially when the cell interface is not parallel with the wall.

7.3.4 A General Collision Model

The C_μ and C_κ values in Table 2.2 are assumed in a phenomenological collision model and are determined from numerical experiments based on the current DSMC-IP method. Any changes to the DSMC-IP method will have effects on the C_μ and

C_κ values and a new set of values must be re-evaluated by performing numerical experiments. It is, therefore, worth simulating the collisions in the DSMC-IP method by a better model that has less dependence on numerical experiments.

Since the DSMC and DSMC-IP methods decouple the particle movements and collisions in each time step, the Boltzmann equation can be split into two parts which, respectively, represent the convection and collision phenomena in a flow

$$\frac{\partial}{\partial t}F + \mathbf{c}\cdot\nabla F = 0, \tag{7.1a}$$

$$\frac{\partial}{\partial t}F = \frac{\delta}{\delta t}F. \tag{7.1b}$$

Equation (7.1b) can be approximated by the BGK model [12]. Assuming that an IP particle j is characterized by the Maxwellian distribution $\mathcal{M}_j$ at time t and in a cell that has the local equilibrium distribution $\mathcal{M}_c$, the evolution of the IP particle in the cell due to collisions is

$$\frac{\partial}{\partial t}F_j = \frac{\mathcal{M}_c - F_j}{\tau}, \tag{7.2}$$

where τ is the local relaxation time and can be evaluated with $\tau = \mu/p$. The exact solution to Equation (7.2) over a small period of time Δt is

$$\begin{aligned} F_j(t+\Delta t) &= \mathcal{M}_c + (\mathcal{M}_j(t) - \mathcal{M}_c)e^{-\Delta t/\tau} \\ &= \mathcal{M}_j(t)e^{-\Delta t/\tau} + \left(1 - e^{-\Delta t/\tau}\right)\mathcal{M}_c. \end{aligned} \tag{7.3}$$

It is easy to show that the distribution F_j remains unchanged as $\Delta t \to 0$ or evolves to $\mathcal{M}_c$ as $\Delta t \to \infty$. If the distribution of the IP particle after Δt is further approximated to be Maxwellian, its velocity and temperature can be analytically determined by

$$\boldsymbol{\xi}_j(t+\Delta t) = \frac{1}{\rho}\int_{\mathbb{R}^3} m\mathbf{c}F_j(t+\Delta t)\,d\mathbf{c}, \tag{7.4}$$

$$T_j(t+\Delta t) = \frac{1}{3\rho R}\int_{\mathbb{R}^3} mc'^2F_j(t+\Delta t)\,d\mathbf{c}. \tag{7.5}$$

7.3.5 Numerical Efficiency Improvement

As mentioned above, the current hybrid approach requires a smaller time step than the standard DSMC method because of the explicit CFD scheme and the DSMC-IP technique. To improve the numerical efficiency of the hybrid approach, a faster CFD method, such as an implicit scheme, can be incorporated. It is unclear at this point how exactly to increase the time step allowed in the DSMC-IP technique. One direction is to modify the DSMC-IP technique with the new energy flux model in Section 2.5 and the new boundary conditions in Section 7.3.3.

7.3.6 Physical Models

The level of physical modeling implemented so far in the hybrid code is only capable of simulating a simple, perfect gas. As the purpose of developing a hybrid code is specifically intended for hypersonic flow with local regions of nonequilibrium, the level of physical modeling needs to be raised to include the ability to simulate thermal nonequilibrium of rotational and vibrational molecular modes, as well as finite-rate, nonequilibrium chemistry. In addition, the future hybrid approach must be capable of simulating flows with multi-species. For DSMC and CFD, methods for modeling the thermochemical nonequilibrium and gas mixtures are available, but for the DSMC-IP method, schemes for modeling these same processes are yet to be developed.

APPENDICES

APPENDIX A

Shock Structures by the DSMC-IP with the New Energy Flux Model

A.1 Shocks in Argon

Unless otherwise specified, the computational domain spans about 40 upstream mean free paths and is evenly divided between the upstream and downstream regions with the initial discontinuity at the origin. Although this is a 1-D problem, a 2-D grid with 400 uniform cells in the flow direction and 5 cells in the transverse direction is employed. The results shown below are from the middle 400 cells. The number of particles per cell in the upstream is about 30 on average. The reference time-step is 10 nsec in all cases.

In Figure A.1, results from the present IP method for a weak Mach 1.55 shock are compared with the old IP method [78] and with DSMC. It is clear that the present IP method is better than the old one. Although the profiles of the present IP method and DSMC in the figure are in good agreement in the rear portion of the shock, the present method still fails to predict the onset of temperature increase at the upstream edge of the shock. Detailed inspection reveals that the density profile calculated with the current IP method is slightly thinner.

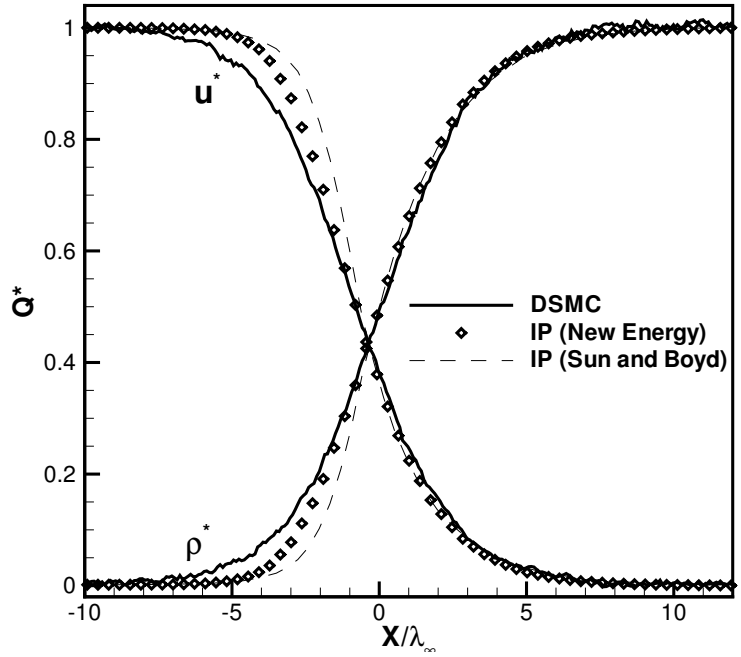

(a) Comparison of density and velocity.

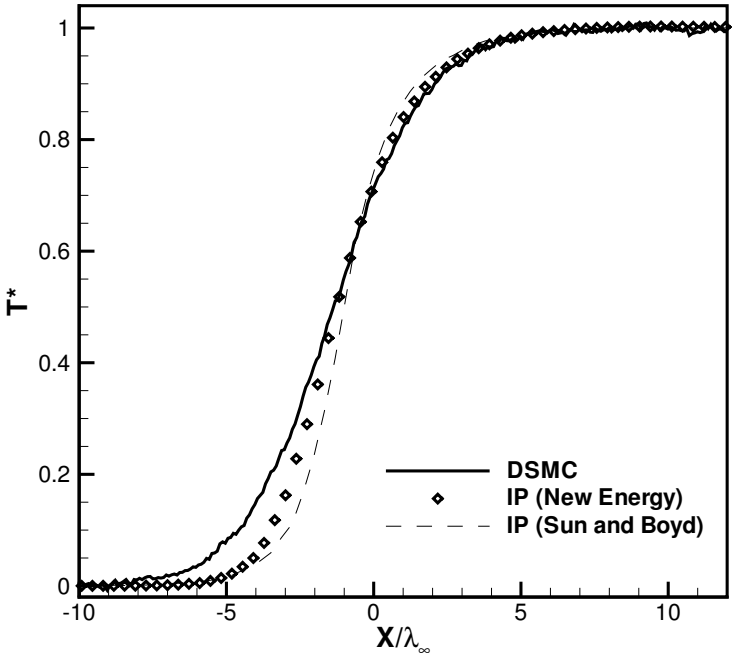

(b) Comparison of translational temperature.

Figure A.1: Comparison of non-dimensional flow properties for a Mach 1.55 shock in argon.

Figure A.2 shows the results when the Mach number is increased to 4. The density profile predicted with the present IP method is in excellent agreement with the DSMC results. The discrepancies in the temperature and velocity at the shock front still persist but they are not any worse than in the last example at lower Mach number. On the other hand, the old IP method results are very poor.

Under hypersonic upstream conditions, it is very difficult for the old IP method to generate reasonable results at Mach numbers higher than 5. On the other hand, the IP method with the new energy flux model works very well even if Mach number is increased to 8. Comparisons for non-dimensional density, velocity, and temperature are displayed in Figure A.3. The density profile predicted with the IP method and the new energy flux model is again in excellent agreement with the DSMC results although the IP method predicts a slightly thicker shock.

The size of the downstream computational region at Mach 8 and higher is increased to about 60 upstream mean free paths. Numerical experiments demonstrated mismatched downstream boundary conditions if the size of the downstream region is too small.

The reciprocal shock thickness (a measure of the maximum density gradient) is shown in Figure A.4 as a function of Mach number. The experimental data are from Alsmeyer [5] and Navier-Stokes data from Boyd [21]. The most striking conclusion that can be made is that the current IP method predicts shock density profiles much closer to the experimental and DSMC results for all Mach numbers than the old IP method. When the Mach number is very high, the shock thickness calculated with the IP method is slightly thicker than the measured data. The overall accuracy of the new IP method is much better than the CFD method, except at very low Mach numbers. Notice that the old IP method stops at Mach 5 because reasonable results

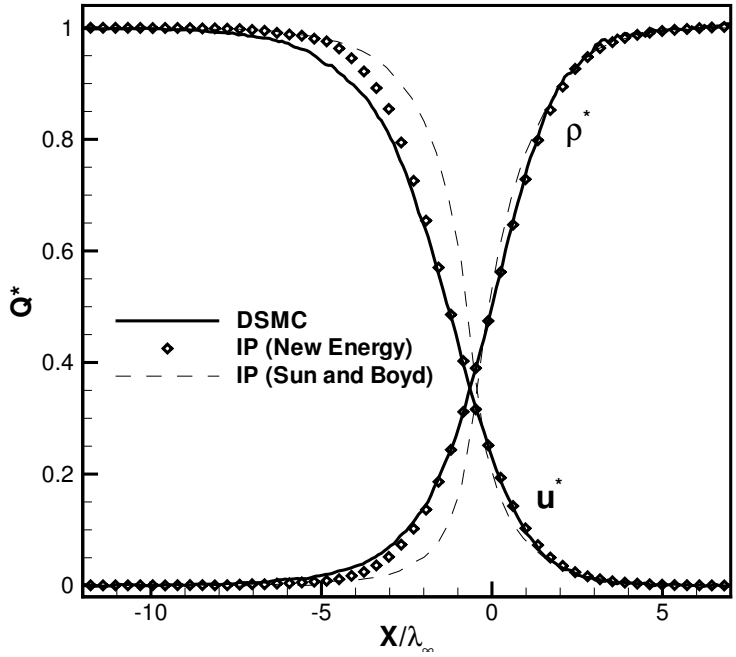

(a) Comparison of density and velocity.

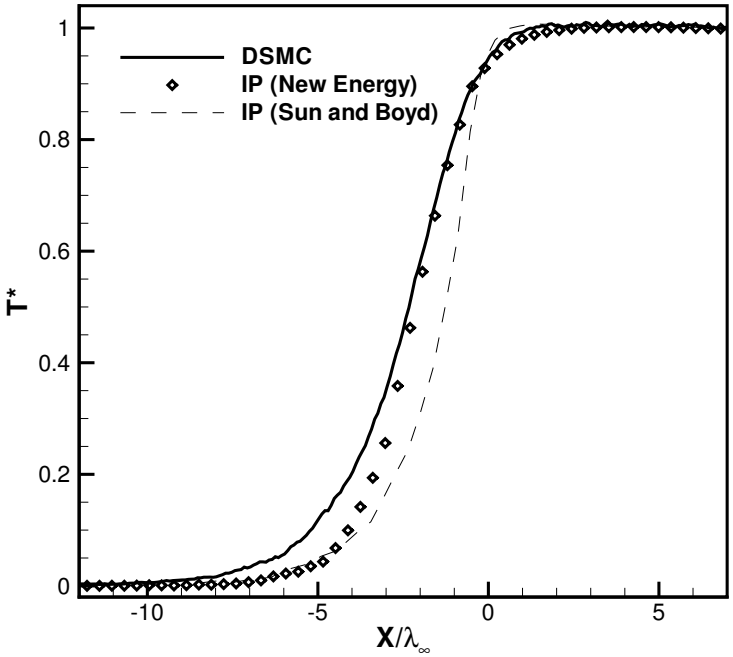

(b) Comparison of translational temperature.

Figure A.2: Comparison of non-dimensional flow properties for a Mach 4 shock in argon.

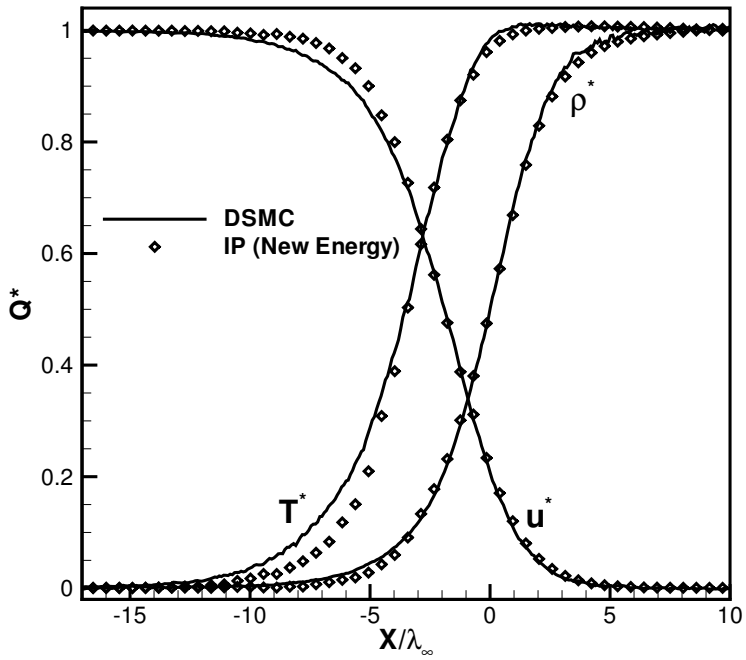

Figure A.3: Comparisons of non-dimensional flow properties for a Mach 8 shock in argon.

are difficult to obtain for higher Mach numbers.

A.2 Shocks in Nitrogen

When nitrogen gas is considered, the number of internal degrees of freedom ζ is 2 due to rotation. The upstream conditions of a Mach 5 flow are $u_1 = 1248.6$ m/s, $T_1 = 300$ K and $\rho_1 = 7.483 \times 10^{-5}$ kg/m^3. The downstream temperature is $T_2 = 1740$ K. The computational domain spans about 50 upstream mean free paths, otherwise it is the same as in the previous examples. A similar 2-D grid is again employed. The number of particles per cell in the upstream is also about 30. The reference time-step is 20 nsec.

The results from the new IP method are in very good agreement with the DSMC results in terms of density and velocity, as shown in Figure A.5(a). The reciprocal shock thickness predicted by DSMC and the new IP method is 0.345 and 0.330,

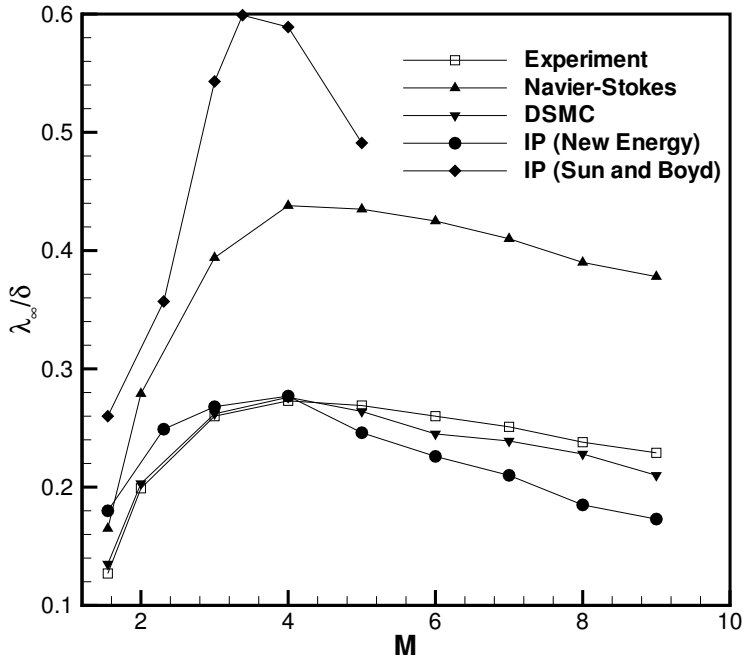

Figure A.4: Comparisons for reciprocal shock thickness for shock waves in argon.

respectively, compared with the measured data of about 0.35 from Alsmeyer [5].

An overall kinetic temperature $T_{\rm ov}$ may be introduced for a nonequilibrium gas as the weighted average of the translational and internal temperatures [16]

$$T_{\rm ov} = (3T_{\rm tra} + \zeta T_{\rm int})/(3 + \zeta).$$

Strong nonequilibrium effects can easily be observed from the significant differences between the DSMC translational and rotational temperatures in Figure A.5(b).

Because the principle of equipartition of energy is applied in the current IP method, meaning that the translational and internal temperatures must be equal, there is no way at this point for the IP method to predict this kind of nonequilibrium. Unlike the argon gas examples, the onset of temperature at the upstream edge of the Mach 5 nitrogen shock is well captured by the IP method. The resulting IP temperature profile also shows a 0.8% overshoot near the center of the shock. Higher Mach numbers are not considered because the downstream temperature will increase

substantially. At Mach 6, for instance, the downstream temperature increases to about 2,400 K, and it is difficult to judge at such high temperature the accuracy of the new IP method due to the nonequilibrium effects. In the future development of the IP method, rotational and vibrational relaxation will be taken into account.

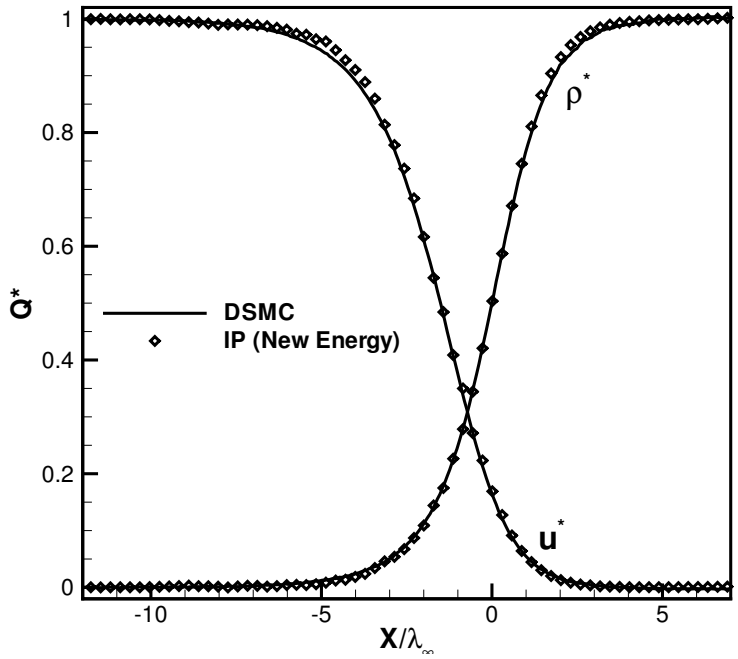

(a) Comparison of density and velocity.

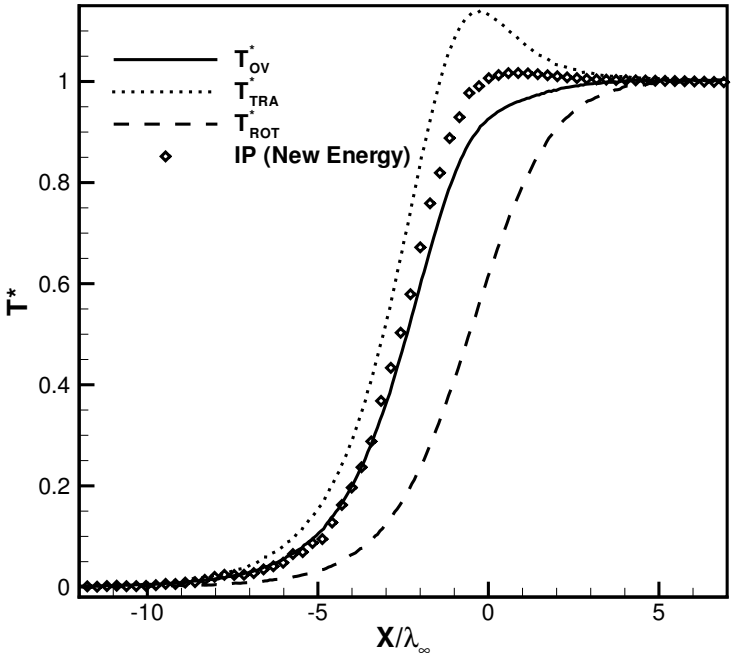

(b) Comparison of temperatures.

Figure A.5: Comparison of non-dimensional flow properties for a Mach 5 shock in nitrogen.

APPENDIX B

Similarity of the Knudsen Numbers Based on Density and Temperature

By taking the ratio of the two Knudsen numbers

$$\frac{\mathrm{Kn}_D}{\mathrm{Kn}_T} = \frac{T}{\rho}\left|\frac{\nabla\rho}{\nabla T}\right|$$

and recognizing in the boundary layer that the derivative in the normal direction n is much larger in magnitude than in the tangential direction, the ratio can be approximated as

$$\frac{\mathrm{Kn}_D}{\mathrm{Kn}_T} \approx \frac{T}{\rho}\left|\frac{\partial\rho/\partial n}{\partial T/\partial n}\right|.$$

Furthermore, since pressure p, which is proportional to ρT, in the boundary layer is approximately invariant along the normal direction n, we have $\rho\frac{\partial T}{\partial n} + T\frac{\partial \rho}{\partial n} = 0$. Accordingly, the ratio of the two Knudsen numbers becomes

$$\frac{\mathrm{Kn}_D}{\mathrm{Kn}_T} \approx 1$$

at a small distance from the wall. The same proof applies to P.

BIBLIOGRAPHY

BIBLIOGRAPHY

[1] O. Aktas and N. R. Aluru. A Combined Continuum/DSMC Technique for Multiscale Analysis of Microfluidic Filters. *Journal of Computational Physics*, 178(2):342–372, 2002.

[2] B. J. Alder and T. E. Wainwright. Studies in Molecular Dynamics. *Journal of Chemical Physics*, 27:1208–1209, 1957.

[3] B. J. Alder and T. E. Wainwright. Studies in Molecular Dynamics. I. General Method. *Journal of Chemical Physics*, 31:459–466, 1959.

[4] M. P. Allen and D. J. Tildesley. *Computer Simulation of Liquids*. Oxford University Press, New York, 1987.

[5] H. Alsmeyer. Density Profiles in Argon and Nitrogen Shock Waves Measured by the Absorption of an Electron Beam. *Journal of Fluid Mechanics*, 74(3):497–513, 1976.

[6] D. A. Anderson, J. C. Tannehill, and R. H. Pletcher. *Computational Fluid Mechanics and Heat Transfer*. Hemisphere Publishing, Washington, 1984.

[7] J. D. Anderson. *Hypersonic and High Temperature Gas Dynamics*. McGraw-Hill, New York, 1989.

[8] D. Baganoff and J. D. McDonald. A Collision-Selection Rule for a Particle Simulation Method Suited to Vector Computers. *Physics of Fluids*, 2(7):1248–1259, July 1990.

[9] R. Balakrishnan and R. K. Agarwal. Numerical Simulation of Bhatnagar-Gross-Krook–Burnett Equations for Hypersonic Flows. *Journal of Thermophysics and Heat Transfer*, 11(3):391–399, 1997.

[10] R. Balakrishnan, R. K. Agarwal, and K.-Y. Yun. Higher-Order Distribution Functions, BGK-Burnett Equations and Boltzmann's H-Theorem. AIAA Paper 1997–2551, June 1997.

[11] J. J. Bertin. *Hypersonic Aerothermodynamics*. American Institute of Aeronautics and Astronautics, Washington DC, 1994.

[12] P. L. Bhatnagar, E. P. Gross, and M. Krook. A Model for Collision Processes in Gases. I. Small Amplitude Processes in Charged and Neutral One-Component Systems. *Physical Review*, 94(3):511–525, 1954.

[13] G. A. Bird. Breakdown of Translational and Rotational Equilibrium in Gaseous Expansions. *AIAA Journal*, 8:1998–2003, 1970.

[14] G. A. Bird. Direct Simulation and the Boltzmann Equation. *Physics of Fluids*, 13(11):2676–2681, Nov. 1970.

[15] G. A. Bird. Monte-Carlo Simulation in an Engineering Context. In S. S. Fisher, editor, *Proceedings of the 12th International Symposium on Rarefied Gas Dynamics, Charlottesville, Virginia*, pages 239–255, 1981.

[16] G. A. Bird. *Molecular Gas Dynamics and the Direct Simulation of Gas Flows*. Oxford University Press, New York, 1994.

[17] C. Borgnakke and P. S. Larsen. Statistical Collision Model for Monte Carlo Simulation of Polyatomic Gas Mixture. *Journal of Computational Physics*, 18:405–420, 1975.

[18] J.-F. Bourgat, P. L. Tallec, and M. D. Tidriri. Coupling Boltzmann and Navier-Stokes Equations by Friction. *Journal of Computational Physics*, 127(2):227–245, 1996.

[19] I. D. Boyd. Analysis of Rotational Nonequilibrium in Standing Shock Waves of Nitrogen. *AIAA Journal*, 28(11):1997–1999, Nov. 1990.

[20] I. D. Boyd. Rotational-Translational Energy Transfer in Rarefied Nonequilibrium Flows. *Physics of Fluids A*, 2(3):447–452, Mar. 1990.

[21] I. D. Boyd. Predicting Breakdown of the Continuum Equations Under Rarefied Flow Conditions. In A. D. Ketsdever and E. P. Muntz, editors, *Proceedings of the 23th International Symposium on Rarefied Gas Dynamics, Wistler, Canada*, pages 899–906, 2003.

[22] I. D. Boyd, G. Chen, and G. V. Candler. Predicting Failure of the Continuum Fluid Equations in Transitional Hypersonic Flows. *Physics of Fluids*, 7(1):210–219, Jan. 1995.

[23] I. D. Boyd and W.-L. Wang. Monte Carlo Computations of Hypersonic Interacting Flows. AIAA Paper 2001–1029, Jan. 2001.

[24] C. Cai, I. D. Boyd, J. Fan, and G. V. Candler. Direct Simulation Methods for Low-Speed Microchannel Flows. *Journal of Thermophysics and Heat Transfer*, 14(3):368–378, 2000.

[25] G. V. Candler, I. Nompelis, and M.-C. Druguet. Navier-Stokes Predictions of Hypersonic Double-Cone and Cylinder-Flare Flow Field. AIAA Paper 2001–1024, Jan. 2001.

[26] G. V. Candler, I. Nompelis, M.-C. Druguet, M. S. Holden, T. P. Wadhams, I. D. Boyd, and W.-L. Wang. CFD Validation for Hypersonic Flight: Hypersonic Double-Cone Flow Simulations. AIAA Paper 2002–0581, Jan. 2002.

[27] C. Cercignani. *Rarefied Gas Dynamics: From Basic Concepts to Actual Calculations*. Cambridge University Press, Cambridge, 2000.

[28] S. Y. Chou and D. Baganoff. Kinetic Flux-Vector Splitting for the Navier-Stokes Equations. *Journal of Computational Physics*, 130(2):217–230, 1997.

[29] K. A. Comeaux, D. R. Chapman, and R. W. MacCormack. An Analysis of the Burnett Equations Based on the Second Law of Thermodynamics. AIAA Paper 1995–0415, Jan. 1995.

[30] S. Dietrich and I. D. Boyd. Scalar and Parallel Optimized Implementation of the Direct Simulation Monte Carlo Method. *Journal of Computational Physics*, 126:328–342, 1996.

[31] C. R. Duttweiler. *Development and Parallelization of a Hybrid Particle/Continuum Method for Simulating Rarefied Flow*. PhD thesis, Department of Aeronautics and Astronautics, Stanford University, 1998.

[32] J. Fan, I. D. Boyd, C.-P. Cai, K. Hennighausen, and G. V. Candler. Computation of Rarefied Gas Flows Around a NACA 0012 Airfoil. *AIAA Journal*, 39:618–625, 2001.

[33] J. Fan and C. Shen. Statistical Simulation of Low-Speed Unidirectional Flow in Transition Regime. In e. a. R. Brum, editor, *Proceedings of the 21th International Symposium on Rarefied Gas Dynamics, Marseille, France*, pages 245–252, 1998.

[34] A. L. Garcia. *Numerical Methods for Physics*. Prentice-Hall, Englewood Cliffs, New Jersey, 1994.

[35] A. L. Garcia and B. J. Alder. Generation of the Chapman-Enskog Distribution. *Journal of Computational Physics*, 140(1):66–70, 1998.

[36] A. L. Garcia, J. B. Bell, W. Y. Crutchfield, and B. J. Alder. Adaptive Mesh and Algorithm Refinement Using Direct Simulation Monte Carlo. *Journal of Computational Physics*, 154(1):134–155, 1999.

[37] J. D. George and I. D. Boyd. Simulation of Nozzle Plume Flows Using a Combined CFD-DSMC Approach. AIAA Paper 1999–3454, June 1999.

[38] P. A. Gnoffo. CFD Validation Studies for Hypersonic Flow Prediction. AIAA Paper 2001–1025, Jan. 2001.

[39] T. Gökçen and R. W. MacCormack. Nonequilibrium Effects for Hypersonic Transitional Flows Using Continuum Approach. AIAA Paper 1989–0461, Jan. 1989.

[40] T. I. Gombosi. *Gaskinetic Theory*. Cambridge University Press, New York, 1994.

[41] N. G. Hadjiconstantinou. Hybrid Atomistic-Continuum Formulations and the Moving Contact-Line Problem. *Journal of Computational Physics*, 154(2):245–265, 1999.

[42] J. K. Harvey. A Review of a Validation Exercise on the Use of the DSMC Method to Compute Viscous/Inviscid Interactions in Hypersonic Flow. AIAA Paper 2003–3643, June 2003.

[43] J. K. Harvey, M. S. Holden, and T. P. Wadhams. Code Validation Study of Laminar Shock/Boundary Layer and Shock/Shock Interactions in Hypersonic Flow. Part B: Comparison with Navier-Stokes and DSMC Solutions. AIAA Paper 2001–1031, Jan. 2001.

[44] D. B. Hash and H. A. Hassan. Assessment of Schemes for Coupling Monte Carlo and Navier-Stokes Solution Methods. *Journal of Thermophysics and Heat Transfer*, 10(2):242–249, 1996.

[45] D. B. Hash and H. A. Hassan. An Decoupled DSMC/Navier-Stokes Analysis of a Transitional Flow Experiment. AIAA Paper 1996–0353, Jan. 1996.

[46] D. B. Hash and H. A. Hassan. Two-Dimensional Coupling Issues of Hybrid DSMC/Navier-Stokes Solvers. AIAA Paper 1997–2507, June 1997.

[47] C. Hirsch. *Numerical Computation of Internal and External Flows, Volume 1: Fundamentals of Numerical Discretization*. John Wiley & Sons, New York, 1989.

[48] C. Hirsch. *Numerical Computation of Internal and External Flows, Volume 2: Computational Methods for Inviscid and Viscous Flows*. John Wiley & Sons, New York, 1990.

[49] M. S. Holden. Experimental Database from CUBRC Studies in Hypersonic Laminar and Turbulent Interacting Flows including Flowfield Chemistry. RTO Code Validation of DSMC and Navier-Stokes Code Validation Studies CUBRC Report, June 2000.

[50] M. S. Holden. Measurement in Regions of Laminar Shock Wave/Boundary Layer Interaction in Hypersonic Flow - Code Validation. CUBRC Report in CD-ROW, May 2003.

[51] M. S. Holden and T. P. Wadhams. Code Validation Study of Laminar Shock/Boundary Layer and Shock/Shock Interactions in Hypersonic Flow. Part A: Experimental Measurements. AIAA Paper 2001–1031, Jan. 2001.

[52] C. R. Kaplan and E. S. Oran. Nonlinear Filtering for Low-Velocity Gaseous Microflows. *AIAA Journal*, 40:82–90, 2002.

[53] H. Kato and J. C. Tannehill. Computation of Hypersonic Laminar Separated Flows using an Iterated PNS Algorithm. AIAA Paper 2001–1028, Jan. 2001.

[54] K. Koura and H. Matsumoto. Variable Soft Sphere Molecular Model for Air Species. *Physics of Fluids A*, 4(5):1083–1085, May 1992.

[55] J. A. Lordi and R. E. Mates. Rotational Relaxation in Nonpolar Diatomic Gases. *Physics of Fluids*, 13:291–308, 1970.

[56] T. Lou. *Basis for a Hybrid Scheme Combining Kinetic Flux-Vector Splitting for the Navier-Stokes Equations With a Particle Method*. PhD thesis, Department of Aeronautics and Astronautics, Stanford University, 1996.

[57] R. W. MacCormack and G. V. Candler. The Solution of the Navier-Stokes Equations Using Gauss-Seidel Line Relaxation. *Computers and Fluids*, 17(1):135–150, 1989.

[58] J. G. Méolans. Thermal Slip Boundary Conditions in Vibrational Nonequilibrium Flows. *Mechanics Research Communications*, 30:629–637, 2003.

[59] C. H. Michaelis. *Development of A Continuum/Rarefied Hybrid Scheme for Flows with Thermal and Chemical Non-equilibrium*. PhD thesis, Department of Aeronautics and Astronautics, Stanford University, 2001.

[60] J. N. Moss. DSMC Computations for Regions of Shock/Shock and Shock/Boundary Layer Interaction. AIAA Paper 2001–1027, Jan. 2001.

[61] I. Nompelis. private communication, Aug. 2001.

[62] I. Nompelis. private communication, Aug. 2003.

[63] C. K. Oh and E. S. Oran. A New Hybrid Algorithm: Navier-Stokes as a DSMC Filter. AIAA Paper 1998–0849, Jan. 1998.

[64] T. Ohwada. Structure of Normal Shock Waves: Direct Numerical Analysis of the Boltzmann Equation for Hard-Sphere Molecules. *Physics of Fluids A*, 5(1):217–234, Jan. 1993.

[65] T. Ohwada. Heat Flow and Temperature and Density Distributions in a Rarefied Gas Between Parallel Plates with Different Temperature. Finite-Difference Analysis of the Nonlinear Boltzmann Equation for Hard-Sphere Molecules. *Physics of Fluids*, 8(8):2153–2160, Aug. 1996.

[66] J. G. Parker. Rotational and Vibrational Relaxation in Diatomic Gases. *Physics of Fluids*, 2:449–462, 1959.

[67] D. I. Pullin. Direct Simulation Methods for Compressible Inviscid Idal-Gas Flow. *Journal of Computational Physics*, 34:231–244, 1980.

[68] A. Rahman. Correlations in the Motion of Atoms in Liquid Argon. *Physical Review A*, 136:405–411, 1964.

[69] D. J. Rasky, H. K. Tran, and D. B. Leiser. Thermal Protection Systems. *Launchspace*, 3:49–54, 1998.

[70] R. Rovedo, D. B. Goldstein, and P. L. Varghese. Hybrid Euler/Particle Approach for Continuum/Rarefied Flows. *Journal of Spacecraft and Rockets*, 35(3):258–265, 1998.

[71] R. Rovedo, D. B. Goldstein, and P. L. Varghese. Hybrid Euler/Direct Simulation Monte Carlo Calculation of Unsteady Slit Flow. *Journal of Spacecraft and Rockets*, 37(6):753–760, 2000.

[72] C. J. Roy, T. J. Bartel, M. A. Gallis, and J. L. Payne. DSMC and Navier-Stokes Predictions for Hypersonic Laminar Interacting Flows. AIAA Paper 2001–1030, Jan. 2001.

[73] C. J. Roy, M. A. Gallis, T. J. Bartel, and J. L. Payne. Navier-Stokes and DSMC Simulations for Hypersonic Laminar Shock-Shock Interaction Flows. AIAA Paper 2002–0737, Jan. 2002.

[74] S. A. Schaaf and P. L. Chambre. *Flow of Rarefied Gases*. Princeton University Press, Princeton, NJ, 1966.

[75] C. Shen, J. Z. Jiang, and J. Fan. Information Preservation Method For The Case of Temperature Variation. In T. J. Bartel and M. A. Gallis, editors, *Proceedings of the 22nd International Symposium on Rarefied Gas Dynamics, Sydney, Australia*, volume 585, pages 185–192, 2001.

[76] Y. Sone, T. Ohwada, and K. Aoki. Temperature Jump and Knudsen Layer in a Rarefied Gas over a Plate Wall: Numerical Analysis of the Linearized Boltzmann Equation for Hard-Sphere Molecules. *Physics of Fluids A*, 1(2):363–370, Feb. 1989.

[77] Q. Sun. *Information Preservation Methods for Modeling Micro-Scale Gas Flows*. PhD thesis, Department of Aerospace Engineering, University of Michigan, 2003.

[78] Q. Sun and I. D. Boyd. A Direct Simulation Method for Subsonic, Micro-Scale Gas Flows. *Journal of Computational Physics*, 179(2):400–425, 2002.

[79] Q. Sun, I. D. Boyd, and G. V. Candler. Numerical Simulation of Gas Flow Over Micro-Scale Airfoils. *Journal of Thermophysics and Heat Transfer*, 16(2):171–179, 2002.

[80] Q. Sun, I. D. Boyd, and G. V. Candler. A Hybrid Continuum/Particle Approach for Micro-Scale Gas Flows. In A. D. Ketsdever and E. P. Muntz, editors,

Proceedings of the 23th International Symposium on Rarefied Gas Dynamics, Wistler, Canada, pages 752–759, 2003.

[81] P. L. Tallec and F. Mallinger. Coupling Boltzmann and Navier-Stokes Equations by Half Fluxes. *Journal of Computational Physics*, 136(1):51–67, 1997.

[82] P. Vijayakumar, Q. Sun, and I. D. Boyd. Detailed Models of Vibrational-Translational Energy Exchange for the Direct Simulation Monte Carlo Method. *Physics of Fluids*, 11(8):2117–2126, Aug. 1999.

[83] W. G. Vincenti and C. H. Kruger, Jr. *Introduction to Physical Gas Dynamics*. Krieger Publishing, Malabar, Florida, 1986.

[84] D. C. Wadsworth and D. A. Erwin. One-Dimensional Hybrid Continuum/Particle Simulation Approach for Rarefied Hypersonic Flows. AIAA Paper 1990–1690, June 1990.

[85] D. C. Wadsworth and D. A. Erwin. Two-Dimensional Hybrid Continuum/Particle Simulation Approach for Rarefied Hypersonic Flows. AIAA Paper 1992–2975, July 1992.

[86] W.-L. Wang and I. D. Boyd. A New Energy Flux Model in the DSMC-IP Method for Nonequilibrium Flows. AIAA Paper 2003–3774, June 2003.

[87] W.-L. Wang, I. D. Boyd, G. V. Candler, and I. Nompelis. Particle and Continuum Computations of Hypersonic Flow Over Sharp and Blunted Cones. AIAA Paper 2001–2900, June 2001.

[88] W.-L. Wang, Q. Sun, and I. D. Boyd. Assessment of a Hybrid Method for Hypersonic Flows. In A. D. Ketsdever and E. P. Muntz, editors, *Proceedings of the 23th International Symposium on Rarefied Gas Dynamics, Wistler, Canada*, pages 923–930, 2003.

ABSTRACT

A HYBRID PARTICLE/CONTINUUM APPROACH FOR
NONEQUILIBRIUM HYPERSONIC FLOWS

by

Wen-Lan Wang

Chairperson: Professor Iain D. Boyd

A hybrid particle-continuum computational framework is developed and presented for simulating nonequilibrium hypersonic flows, aimed to be more accurate than conventional continuum methods and faster than particle methods. The framework consists of the direct simulation Monte Carlo-Information Preservation (DSMC-IP) method coupled with a Navier-Stokes solver. Since the DSMC-IP method provides the macroscopic information at each time step, determination of the continuum fluxes across the interface between the particle and continuum domains becomes straightforward.

Buffer and reservoir cells are introduced in the continuum domain and work as an extension of the particle domain. At the end of the particle movement phase, particles in either particle or buffer cells are retained. All simulated particles in the reservoir cells are first deleted for each time step and re-generated based on the local

cell values. The microscopic velocities for the newly generated particles are initialized to the Chapman-Enskog distribution using an acceptance-rejection scheme.

Continuum breakdown in a flow is defined as when the continuum solution departs from the particle solution to at least 5%. Numerical investigations show that a Knudsen-number-like parameter can best predict the continuum breakdown in the flows of interest.

Numerical experiments of hypersonic flows over a simple blunted cone and a much more complex hollow cylinder/flare are conducted. The solutions for the two geometries considered from the hybrid framework are compared with experimental data and pure particle solutions. Generally speaking, it is concluded that the hybrid approach works quite well. In the blunted cone flow, numerical accuracy is improved when 10 layers of buffer cells are employed and the continuum breakdown cut-off value is set to be 0.03. In the hollow cylinder/flare hybrid simulation, the size of the separation zone near the conjunction of the cylinder and flare is improved from the initial continuum solution to approximately that in the measured data. Numerical accuracy of the flow field varies with locations. It is also concluded that the numerical efficiency obtained with the hybrid approach is far from satisfactory. Overall, the present framework is the first fully coupled, hybrid continuum-particle method for nonequilibrium hypersonic flows and provides a solid foundation for future development.